Upsilon Production and Suppression as Measured by STAR in $p+p$, $d+\mathrm{Au}$, and $\mathrm{Au}+\mathrm{Au}$ Collisions at $\sqrt{s_{NN}} = 200$ GeV

By

ANTHONY ROBERT KESICH

B.S. (Massachusetts Institute of Technology) 2009
M.S. (University of California, Davis) 2011

DISSERTATION

Submitted in partial satisfaction of the requirements for the degree of

DOCTOR OF PHILOSOPHY

in

Physics

in the

OFFICE OF GRADUATE STUDIES

of the

UNIVERSITY OF CALIFORNIA

DAVIS

Approved:

Manuel Calderón de la Barca Sánchez, Chair

Daniel Cebra

Ramona Vogt

Committee in Charge

2014

Contents

List of Figures iv

List of Tables xii

Abstract xiii

Acknowledgments xiv

Chapter 1. Introduction 1

Chapter 2. Background 4

2.1. History 4

2.2. The Standard Model 9

Chapter 3. Physics of the Quark-Gluon Plasma 17

3.1. Lattice Calculations of the QGP 17

3.2. Experimental Evidence for the QGP 19

3.3. Quarkonium Production and Suppression 23

Chapter 4. The Relativistic Heavy Ion Collider 31

4.1. Tandem Van de Graaff 31

4.2. BNL Linear Accelerator 32

4.3. Alternating Gradient Synchrotron 33

4.4. RHIC 35

Chapter 5. The Solenoidal Tracker at RHIC 38

5.1. Beam-Beam Counter 38

5.2. Zero Degree Calorimeter 39

5.3. Vertex Position Detector 40

5.4. Time Projection Chamber 41

5.5. Barrel Electromagnetic Calorimeter 44

Chapter 6. Analysis Methods 48

6.1. Triggering 48

6.2. Harvesting Υ Candidates 50

6.3. Acceptance and Triggering Efficiency 53

6.4. Run Selection and Luminosity 55

6.5. Electron Identification 56

6.6. Invariant Mass Spectrum 62

6.7. Systematics 78

Chapter 7. Results 82

7.1. Yields and Cross Sections 82

7.2. Nuclear Modification Factor 87

7.3. Comparison to Model-Based Psuedoexperiments 97

Chapter 8. Conclusions 105

Bibliography 107

List of Figures

2.1 A summary of the particles in the Standard Model as well as their masses, charges, and spins [**1**]. The six quarks are shown in violet with rising generations from left to right. The fundamental leptons along with their associated neutrinos are in green. Together, the quarks and leptons contain all fundamental fermions. The vector bosons, which mediate the forces, are in red. In yellow is the recently discovered Higgs boson. 10

2.2 The six elementary quarks arranged by mass and charge and their allowed interactions with W bosons [**2**]. Arrows depict allowed flavor-changing decays. Arrows pointing from right to left are mediated by W^+ bosons; left-to-right arrows depict those mediated by a W^-. Darker arrows denote stronger couplings in the CKM matrix; lighter, weaker. 12

2.3 The fundamental particles of the Standard Model arranged by weak isospin (T_3, x-axis) and weak hypercharge (Y_W, y-axis) [**3**]. Introduction of the Higgs (upper-left quadrant) breaks the weak isospin-hypercharge symmetry, picking out a specific Weinberg angle, θ_W, and orienting the charge axis (Q). 13

3.1 Energy density and triple the pressure as a function of temperature obtained from lattice calculations [**4**]. The sharp rise in energy density just below 200 MeV is indicative of a phase transition. The Stefan-Boltzmann limit (i.e. the energy density of an ideal gas) is shown in the upper right. 18

3.2 The running QCD heavy quark-quark coupling constant from 2-flavor lattice QCD calculations [**5**]. At temperatures above T_c, the couping constant at quarkonium interquark distance scales ($\sim 0.5 - 1$ fm) rapidly decreases, inhibiting the formation of loosely bound heavy quarkonia. 19

3.3 The color singlet quark-antiquark free energy from 2-flavor lattice QCD calculations [**5**]. The solid line shows the results in the vacuum. The free energy flattens off at lower and lower energies as temperature increases. 20

3.4 Dihadron correlations in $p+p$, $d+\mathrm{Au}$, and $\mathrm{Au}+\mathrm{Au}$ collisions as measured by STAR [**6**]. Plot (a) shows results for $p+p$ (black line), min. bias $d+\mathrm{Au}$ (green triangles), and 0-20% centrality $d+\mathrm{Au}$ (red circles). Note the peaks at both $\Delta\phi \sim 0$ and $\Delta\phi \sim \pi$, indicating the presence of jets and their azimuthally balanced partners. Plot (b) shows the same $p+p$ and central $d+\mathrm{Au}$ results (pedestal-subtracted), as well as central $\mathrm{Au}+\mathrm{Au}$ results (blue stars). Note the lack of an away-side ($\Delta\phi \sim \pi$) peak in $\mathrm{Au}+\mathrm{Au}$, indicating jet quenching. 21

3.5 Almond-shaped interaction region (red) created by a non-central heavy-ion collision [**7**]. The remnant spectator nucleons are shown in blue. The plane defined by the impact parameter and beam line is called the reaction plane (gray). 22

3.6 Υ(1S+2S+3S) production in $p+p$ collisions at $\sqrt{s_{NN}} = 200$ GeV as measured by STAR compared to CSM (blue dashed line) and CEM (blue squares) predictions [**8**]. Results are from the 2006 $p+p$ run which sampled $\sim 1/3$ the integrated luminosity of the $p+p$ dataset reported on in this thesis. 25

3.7 EPS09 parameterization of nuclear PDFs [**9**]. The upper set of six plots show the modification for carbon; the lower plots show lead. The left column shows the nPDF for valence quarks, the center shows sea quarks, and the right shows gluons. 26

3.8 Bottomonium spectral function calculated with (right) and without (left) the imaginary part of the potential [**10**]. Note the broadening of the line shapes when the imaginary term in included. 28

3.9 The feed down pattern of the bottomonium family [**11**]. Note that what we measure as final state Υ(1S) could have been formed as multiple other bottomonium mesons. 29

4.1 RHIC and its supporting infrastructure [**12**]. 32

4.2 Layout of the two RHIC rings. The separation of the rings is not to scale. The counter-clockwise-circulating yellow ring is shown as a dashed line and the

clockwise-circulating blue ring is solid. The six interaction regions are at 12, 2, 4, 6, 8, and 10 o'clock. [**13**] 33

4.3 The PHENIX detector is a general purpose detector with multiple subsystems [**14**]. It currently operates at the eight o'clock position on RHIC. 34

4.4 The BRAHMS detector [**15**]. Located at the two o'clock IR on RHIC. 36

4.5 The PHOBOS detector [**16**]. Located at the ten o'clock IR on RHIC. 37

5.1 The STAR BBC is divided into two identical detectors on the east and west sides of the interaction region. The each BBC detector contains two inner annuli of smaller scintillators and two outer annuli of larger scintillators [**17**]. 38

5.2 A bird's-eye view of the RHIC beam pipes at STAR and the ZDC. The blue curve shows the path of incoming ions. The charged protons released in the collision are over-deflected as shown by the green curve. The neutrons are undeflected by the dipole magnet and travel directly forward to the ZDC (shown in red) [**18**]. 40

5.3 The STAR Time Projection Chamber. [**19**] 41

5.4 The TPC wiring grid. The gating grid controls whether drifting electrons make it to the anodes where the image charge can be read out by the FEEs while the ground plane and anodes provide signal amplification through electron avalanches [**20**]. 42

5.5 Characteristic ionization energy loss used to identify charged particles. The curves are predictions from the Bichsel equations [**21**]. 44

5.6 TPC momentum resolution as a function of momentum as ascertained by Monte-Carlo simulations. [**22**] 45

5.7 The STAR BEMC surrounds the TPC [**23**]. The Silicon Vertex Tracker (SVT) was removed in 2007 and will be replaced as part of an enhanced silicon vertex detector starting in 2014. 45

5.8 A single tower of the STAR BEMC. [**23**] 47

6.1 ADC Distribution for $p+p$ 2009 Υ triggered data (black), showing the L0 threshold. The expected distribution for the signal obtained from embedding is

shown in blue for all simulated Υ (solid line) and for those that satisfy all the trigger requirements. 49

6.2 L2 Trigger distributions: (Top, left) E_{cluster} for daughter above the high L2 threshold, E_1; (Top, right) E_{cluster} for daughter above the low L2 threshold, E_2; (Bottom, left) L2 cosine of the opening angle, $\cos(\theta_{L2})$; (Bottom, right) L2 invariant mass. All cuts shown are from the 2009 values. 52

6.3 Illustration of the results of calibrating the 2008 L2 trigger correctly during analysis. The left plot shows the comparison between our reconstructed values when offline calibrations are used (y-axis) and what was recorded online. The right plot shows the reconstructed values when we used the online calibrations. The black line is a guide for the eye and has unity slope. Note the vastly reduced spread in the right, calibrated plot. 55

6.4 Example $n\sigma_e$ distributions from the Au + Au dataset. The left figure depicts the distribution at low momentum while the right figure shows higher momenta. Tight cuts on cluster-matching and E/p were applied to enhance the relative number of electrons in the sample. Electrons are shown in blue, pions in red, and protons in green. Notice how the electron curve merges with the pion curve at high momentum. 57

6.5 Summaries of the $n\sigma_e$ fits in Au + Au. Gaussian means as a function of momentum are shown on the left; widths on the right. Electrons are in blue, pions are in red, and protons are in green. 58

6.6 Effictive signal in $p + p$ for a typical momentum bin. The red curve shows the effective signal for single electrons whereas the blue curve shows the effective signal for electron pairs. 59

6.7 Distance between projected TPC track and BEMC cluster from $p + p$ data (blue) and embedded simulations (black). 61

6.8 E/p distributions in the range 5 GeV/c $< p <$ 6 GeV/c for $p + p$ (left) and $d + \text{Au}$ (right). 62

6.9 Examples of E/p distributions in Au + Au for tracks matched to a tower which could have fired the L0 trigger. From left to right, top to bottom, we show data from 0-10%, 10-30%, 30-60%, and 0-60% centrality collisions. Note the broadening of the E/p distribution as we move to more central collisions and the TPC occupancy increases. 63

6.10 Examples of E/p distributions in Au + Au for tracks not matched to a tower which could have fired the L0 trigger. Almost all tracks paired with a L0-triggering track are of this class. From left to right, top to bottom, we show data from 0-10%, 10-30%, 30-60%, and 0-60% centrality collisions. The distributions here are much wider than for the L0-matched tracks (Fig. 6.9). 64

6.11 Four examples of Crystal Ball functions. The normalization (not shown) and Gaussian parameters are left unchanged. The α parameter controls when the function transitions from a Gaussian to a power law. The n parameter is the power in the power law. 65

6.12 Crystal Ball fits to results from $p + p$ embedding for $|y| < 1.0$. The top is Υ(1S), the middle is Υ(2S), and the bottom is Υ(3S). 66

6.13 Comparison between line shapes extracted from direct Υ embedding (blue) and from simulations using electron embeddings (red). From left to right, top to bottom, we show Υ(1S), Υ(2S), and Υ(3S). 67

6.14 Difference between reconstructed mass in the corrected and uncorrected $p + p$ datasets compared to the mass found in the uncorrected dataset. 69

6.15 Projection of Fig. 6.14 onto the Δm axis. The black curve is a Gaussian fit to the projection. Parameters are listed in the upper right corner. 70

6.16 Υ(1S) line shape before (red) and after (black) the additional smearing from the TPC misalignment. This example is from 0-60% centrality Au + Au. 71

6.17 Fits to the Υ signal in $p + p$. The top plot shows midrapidity ($|y| < 0.5$) and the bottom plot shows "side" rapidity ($0.5 < |y| < 1.0$). The hollow blue circles are the like-sign counts and the fit to the background is shown as a dashed blue line. The filled red circles are the unlike-sign counts and the total fit to the signal

and background is shown as a solid red line. The dot-dashed green line shows the combined fits to the background, Drell-Yan signal, and correlated $b\bar{b}$ signal. 73

6.18 Fits to the Υ signal in $d + \mathrm{Au}$. From top to bottom, the fits cover the ranges $-1.0 < y < -0.5$, $|y| < 0.5$, and $0,5 < y < 1.0$. Explanation of most the legend can be found in the caption of Fig. 6.17. In addition, the gray band in the center plot shows the expected N_{coll}-scaled Υ(1S+2S+3S) signal if there is no suppression. 74

6.19 Fits to the Υ signal in $\mathrm{Au} + \mathrm{Au}$ in the rapidity range $|y| < 1.0$. From left to right, top to bottom, the fits cover the centrality ranges 0-60%, 0-10%, 10-30%, and 30-60%. Explanation of the legend can be found in the captions of Figs. 6.17 and 6.18. 75

6.20 Fits to the Υ signal in $\mathrm{Au} + \mathrm{Au}$ in the narrower rapidity range $|y| < 0.5$. 76

6.21 Mass cuts used for yield extraction shown on an example line shape from $\mathrm{Au} + \mathrm{Au}$. For the Υ(1S+2S+3S) yield, the signal is integrated from 8.8 GeV/c^2 to 11.0 GeV/c^2 (solid black lines). The Υ(1S) yield is extracted by lowering the upper mass cut to 10.0 GeV/c^2 (dashed black line). 77

7.1 Comparison of our $p + p$ measurement (red star) to the global set of Υ(1S+2S+3S) production measurements [**24**–**34**]. The blue curve is a NLO Color Evaporation Model calculation of Υ(1S+2S+3S) production done by R. Vogt [**35**]. 84

7.2 Υ(1S+2S+3S) production as a function of rapidity in both $p + p$ and $d + \mathrm{Au}$ collisions. The blue stars show the $p + p$ measurement with horizontal error bars denoting the width of the rapidity bins. The blue star at negative rapidity is hollow to denote that it is a reflection of the forward rapidity $p + p$measurement. The red circles show our $d + \mathrm{Au}$ measurements scaled down by a factor of 1,000 to fit on the same scale. PHENIX measurements are denoted by diamonds [**36**]. The shaded bands denote NLO pQCD CEM calculations [**37**]. 85

7.3 Υ(1S+2S+3S) production in $p + p$ collisions as a function of rapidity. STAR results are shown as blue stars and the forward-rapidity data point is reflected as in Fig. 7.2. The green hatched band shows predictions from QCD-based NLO

Color Singlet Model calculations [**38**]. PHENIX measurements are denoted by diamonds [**36**]. The blue shaded band denotes NLO pQCD CEM calculations [**37**]. 86

7.4 $R_{d\mathrm{Au}}$ as a function of rapidity. Our results are shown as red stars. PHENIX results are shown as green diamonds. The blue hatched band shows predictions based on shadowing from EPS09 done by R. Vogt. Calculations performed by F. Arleo and S. Peignè based on suppression from initial-state parton energy loss but without EPS09 are shown as a blue dashed line [**39**]. The green dot-dashed line shows the combination of energy loss and EPS09. 89

7.5 Comparison of our $d+\mathrm{Au}$ results to the p+A results of E772 [**40**]. (a): Ratio of Υ production in $p(d)$+A to production in p+$d(p)$ as a function of the ion mass number. E772 results are shown as blue circles (Υ(1S)) and green squares (Υ(2S+3S)). Our result for Υ(1S) is shown as a red star. The gray line denotes the model used by E772 where $\sigma_{pA} = A^{\alpha}\sigma_{pp}$. (b): Suppression exponent α as a function of Feynman-x. The vertical dashed lines at the bottom denote the estimated bin widths of our measurements. Note that the results are offset in x_F for clarity. 91

7.6 Υ(1S+2S+3S) R_{AA} as a function of N_{part}. Figure (a) shows R_{AA} for $|y| < 1.0$ whereas Figure (b) shows the same for $|y| < 0.5$. The R_{AA} in $\mathrm{Au}+\mathrm{Au}$ collisions is shown as black circles; the filled circles are split by centrality and the hollow circle is the centrality integrated result. $R_{d\mathrm{Au}}$ is shown as a green square. The shaded blue box around one denotes the statistical uncertainty of the $p+p$ measurement. The solid blue box shows systematics joint to all $d+\mathrm{Au}$ and $\mathrm{Au}+\mathrm{Au}$ results. For $|y| < 1.0$ (Fig. (a)), we also show R_{AA} as measured in $\mathrm{U}+\mathrm{U}$ collisions as red diamonds. The magenta band shows the predicted R_{AA} from calculations by Strickland and Bazow [**41**]. Predictions by Zhao and Rapp are in gray [**42**]. 93

7.7 Υ(1S) suppression as a function of N_{part}. Calculations of Υ(1S) suppression by Liu et al. are shown as the dashed blue line [**43**]. 95

7.8 Nuclear Modification Factor of heavy quarkonia as measured by STAR as a function of binding energy. The high-p_T J/ψ results are from [**44**]. The width of

the Υ(2S+3S) upper limit spans the range between their two biding energies. The arrow is placed at the weighted average of their binding energies. 97

7.9 Summary of simulation results assuming no suppression (scenario 1). The upper plots show the results for $|y| < 0.5$ and the lower plots show $|y| < 1.0$. The red lines denote our results and the pinks bands show systematics uncertainties. 99

7.10 Summary of simulation results assuming suppression from CNM effects only (scenario 2). The upper plots show the results for $|y| < 0.5$ and the lower plots show $|y| < 1.0$. The red lines denote our results and the pinks bands show systematics uncertainties. 100

7.11 Summary of simulation results assuming suppression from QGP effects only (scenario 3). The upper plots show the results for $|y| < 0.5$ and the lower plots show $|y| < 1.0$. The red lines denote our results and the pinks bands show systematics uncertainties. 101

7.12 Summary of simulation results assuming suppression from both the QGP and CNM effects (scenario 4). The upper plots show the results for $|y| < 0.5$ and the lower plots show $|y| < 1.0$. The red lines denote our results and the pinks bands show systematics uncertainties. 102

List of Tables

6.1 Parameters used in the L2 Υ trigger for the 2008 $d+\mathrm{Au}$ and 2009 $p+p$ datasets: ADC threshold value of the L0 triggering tower (must be met to be considered by the L2 algorithm), ADC threshold value of the partner tower, maximum number of times a tower could fire the tigger in a row before being considered a Hot Tower, signal threshold to be considered a Hot Tower, a flag to use the BBC vertex, maximum number of hot towers to mask, minimum energy of the seed towers, minimum cluster energy around the L0 and L2 towers, minimum and maximum invariant mass from BEMC energy, and minimum opening angle. 51

6.2 Geometrical acceptance times triggering efficiency at midrapidity for all three datasets as esitmated through embedding procedures. 54

6.3 Cuts in $n\sigma_e$ for each system. The cuts were chosen by optimizing S_{eff} for each system. 59

6.4 Cuts in E/p for each system. 62

6.5 Systematic uncertainties affecting the cross section. 81

7.1 Yield and measured cross sections. 83

7.2 R_{AA} and $R_{d\mathrm{Au}}$ for all measured Υ states, rapidities, and centrality bins. The results are listed in the form $a \pm b \pm c \pm d \pm e$ where a is $R_{d\mathrm{Au}}$ or R_{AA}, b is the $d+\mathrm{Au}$ or $\mathrm{Au}+\mathrm{Au}$ statistical uncertainty, c is the $p+p$ statistical uncertainty, d is the $d+\mathrm{Au}$ or $\mathrm{Au}+\mathrm{Au}$ systematic uncertainty, and e is the $p+p$ systematic uncertainty. 88

Anthony R. Kesich
September 2014
Physics

Upsilon Production and Suppression as Measured by STAR in $p+p$, $d+\mathrm{Au}$, and $\mathrm{Au}+\mathrm{Au}$ Collisions at $\sqrt{s_{NN}} = 200$ GeV

Abstract

Debye screening of inter-quark potentials leading to suppression of heavy quarkonia has long been a studied signature of the onset of partonic deconfinement. We report on the production of Υ(1S+2S+3S) mesons at $\sqrt{s_{NN}} = 200$ GeV in $p+p$, $d+\mathrm{Au}$, and $\mathrm{Au}+\mathrm{Au}$ collisions as measured by the Solenoidal Tracker At RHIC. We compare our measured yield in $p+p$ collisions to those in $d+\mathrm{Au}$ and $\mathrm{Au}+\mathrm{Au}$ collisions to obtain nuclear modification factors and quantify suppression effects from both hot and cold nuclear matter. We separate our $\mathrm{Au}+\mathrm{Au}$ measurements into three centrality classes. We obtain a nuclear modification factor for Υ(1S+2S+3S) in the rapidity range $|y| < 1$ in $d+\mathrm{Au}$ collisions of$R_{d\mathrm{Au}} = 0.79 \pm 0.24(\mathrm{stat.}) \pm 0.03(\mathrm{sys.}) \pm 0.10(p+p\ \mathrm{sys.})$. A comparison with models including shadowing and initial-state parton energy loss as well as final-state nuclear absorption indicates the presence of additional cold-nuclear matter suppression. In the top 10% most-central $\mathrm{Au}+\mathrm{Au}$ collisions, we measure a nuclear modification factor of $R_{AA} = 0.49 \pm 0.1(\mathrm{stat.}) \pm 0.02(\mathrm{sys.}) \pm 0.06(p+p\ \mathrm{sys.})$, which is a larger suppression factor than that seen in cold nuclear matter. Our results are consistent with complete suppression of the excited Υ(2S+3S) states and we calculate an upper limit of $R_{AA}(2\mathrm{S}+3\mathrm{S}) < 0.32$ with 95% confidence for the 0-60% centrality bin. The additional suppression see in $\mathrm{Au}+\mathrm{Au}$ collisions is consistent with model calculations using initial temperatures ranging from 330 to 442 MeV. However, a better understanding of the suppression seen in $d+\mathrm{Au}$ collisions is needed before any definitive statements about suppression in $\mathrm{Au}+\mathrm{Au}$ collisions can be made.

Acknowledgments

Many thanks go to Manuel and Daniel for guiding me through this long process. I'd also like to thank Ramona for all her theoretical help and for always reminding me I'm not as smart as I think I am. Thanks also to Grazyna Odyniec, Peter Jacobs, and the entire RNC group at LBNL for giving me a place to work for the past year. And, most importantly, my ever-patient wife Amanda for putting up with five years of graduate school.

CHAPTER 1

Introduction

The study of heavy-ion physics, at its heart, is concerned with extending our understanding of matter, both everyday and exotic. The forefront of this field concerns the study of a hot, dense state of matter known as the quark-gluon plasma (QGP). Using large synchrotrons, beams of ions, such as gold, lead, and uranium, are accelerated to near the speed of light then focused into each other, resulting in violent nuclear collisions. Quarks and gluons, typically inextricably trapped within hadrons such as protons and neutrons, are momentarily released to act in a quasifree fashion in the bulk medium. By studying the aftermath of these collisions, we can discern the dynamics governing the interactions of quarks and gluons.

Shortly after the Big Bang, as the universe was expanding, cooling, and rarefying, it is currently understood that everything we now observe in the present as baryonic matter existed as a QGP. The QGP cooled into hadrons, which ultimately decayed down into stable protons, and semi-stable neutrons along with a plethora of photons. Free neutrons bound with protons to form light nuclei or decayed into electrons and more protons. A sea of photons, released through decays and bremsstrahlung radiation, dominated the universe, interacting with electrons and ions. Three hundred eighty thousand years later, the universe cooled and expanded enough that electrons could bind with ions to form atoms without being dissociated by a photon, giving rise to the universe as we (mostly) know it.

Using our knowledge of fundamental forces and bulk dynamics, we can keep turning the clock back to understand what came before. We can turn gravity backwards until the planets, stars, and galaxies disperse into a uniform dust, heating up until everything is a plasma. Using electromagnetism, we can then move back through this phase until the early nuclei formed. Low-energy nuclear physics and the weak force kick in, allowing us to reconstruct earlier compositions of the universe by examining their decay products. But

when we keep turning back the clock back to get to the QGP, our lack of understanding halts progress. Our ability to model and understand earlier epochs is hindered until we first conquer the QGP.

The same equations that govern the QGP also govern quarks and gluons while bound within nuclei. Even though they comprise much of our matter, little is actually known about the behavior of quarks in everyday conditions and much of that knowledge is empirical. Despite what the Higgs boosters claim, most of the baryonic mass in our universe arises not from the Higgs mechanism but from QCD. The Higgs mechanism gives rise to the mass of the quarks themselves. However, the combined mass of the valence quarks in a proton or neutron is only around 10 MeV/c^2, slightly over 1% of the mass of the nucleons. The remaining 99% arises from energy present within the hadron in the form of QCD interactions. Since the nucleons contain the vast majority of the mass in an atom, this means that almost all everyday mass comes not from the Higgs mechanism, but from QCD. Understanding QCD at high energies will ultimately lead to a better understanding of common nuclear matter and teleportation.

To map out the phases of nuclear matter, we need to measure the thermodynamic properties of the QGP. This thesis is focused on measuring the temperature of the QGP created in Au + Au collisions at RHIC. The extreme color fields created inside the plasma can "screen" the heavy quark-antiquark pair which comprise quarkonium. This screening causes the valence quarks to dissociate, enabling them to form open heavy flavor mesons before the quarkonium can escape the QGP where it can undergo standard decays in the vacuum. As the QGP gets hotter, the free partons can screen at smaller and smaller distance scales. The many different quarkonia, J/ψ, χ_c, Υ, η_b, and χ_b to name a few, have a wide range of binding energies and radii. At any temperature in a QGP, the more weakly bound quarkonia will be partially or completely suppressed and the tightly bound quarkonia should remain unsuppressed. By measuring the suppression of different quarkonia, we can determine the length scale at which the QGP starts to screen the inter-quark potential which can inform us about the temperature. In this thesis, we measure the combined production rate of Υ(1S), Υ(2S), and Υ(3S) mesons as well as isolating the ground state, Υ(1S), in $p + p$, d + Au, and Au + Au collisions at $\sqrt{s_{NN}}$=200 GeV and calculate their suppression in

Au + Au collisions to discern properties of the QGP. We also measure suppression in d + Au collisions as a control experiment to quantify suppression which may be due to initial state effects, such as modification of the distribution of partons within the nucleus, or final state effects, like suppression from interactions with spectator nucleons as opposed to suppression due to the presence of a QGP.

The thesis is structured in the following manner: Chapter 2 discusses the history of particle physics and the fundamental theory which currently governs this field. Chapter 3 gives an overview of the current understanding of QGP physics, its signatures, and the theory behind quarkonium suppression. Chapter 4 introduces RHIC along with the rest of the accelerator and collider complex which delivered the particle beams needed for this research. Chapter 5 discusses the particle detector used to collect the data analyzed in this thesis, STAR, and its subsystems. Chapter 6 covers the analysis methods applied in this research. Chapter 7 details the results of this analysis and their implications. Chapter 8 is the summary and conclusion.

CHAPTER 2

Background

2.1. History

Literally everything in our universe is comprised of particles. And at its fundamental level, physics is devoted to understanding their properties and interactions. This is a history best told through matter and forces.

In 1687, Sir Isaac Newton published his great work, *Principia Mathematica*, laying down the first two major planks in our modern interpretation of physics. Through the Second Law, Newton linked force, matter, and motion, allowing for quantitative calculations of the effects force has on our world. He also gave the first quantitative description of one of the four fundamental forces: gravity. Though both were incomplete formulations, Newton's descriptions were accurate enough to remained unchallenged for over 200 years.

The next chapter does not come until 1861, when James Clerk Maxwell published *On Physical Lines of Force*, introducing 20 differential equations with 20 variables governing the dynamics of electric and magnetic fields which would come to be known as Maxwell's Equations. These equations summarize the macroscopic phenomenon of Electromagnetism, another of the four fundamentals. Upon investigation, Maxwell discovered that perturbations in this field should travel with a velocity very near the measured speed of light in that day. Not dismissing this as a coincidence, Maxwell took this as evidence that light and the electromagnetic force must be related, connecting a fundamental force to physical effects beyond the manipulation of matter.

Just a few decades later, in 1897, J. J. Thompson made a remarkable discovery regarding the fundamental nature of cathode rays. Created in vacuum tubes when a large potential is present, cathode rays were originally thought by some to be naturally occurring ions which could gain enough speed in the sparse environment of a vacuum tube to overshoot the anode. By measuring the distance cathode rays could travel in air and the heat they

generated in a collision, Thompson concluded that cathode rays must be negatively charged particles he called the *corpuscle* [**45**], 1000 times smaller and 1000 times lighter than an atom–at the time thought to be the fundamental unit of matter. Thompson had discovered the electron and, in doing so, had cracked open the atom and birthed the field of subatomic physics.

In 1905, Albert Einstein reconciled incongruities between Newton's laws of motion and Maxwell's Equations in his seminal work on special relativity [**46**]. Einstein reworked dynamics to respect the speed of light as a constant and a universal speed limit in all frames. This had immediate implications, including but not limited to the concepts of length contraction, time dilation, and non-absolute ordering of events for observers in relative motion. The most shocking consequence was the concept of mass-energy equivalence, often summarized as $E = mc^2$. By recasting mass as just another manifestation of energy, Einstein's formulation would explain many recently and yet-to-be-discovered phenomena, such as radioactive decay and vacuum pair production.

By the end of the Roaring Twenties, Dirac had progressed along the path to merge quantum mechanics with special relativity. His work had led to the Dirac equation, a relativistic description of the electron's wave function incorporating spin dynamics [**47**]. Dirac could not get around one feature of his equations: the prediction of a particle dual to the electron, but with opposite charge and quantum numbers, later to be known as the positron. Around the same time, experimental evidence for the positron was beginning to emerge. This culminated in 1932 when Carl Anderson used a bubble chamber to measure positrons created when cosmic rays bombarded a lead plate [**48**]. The positron discovered by Anderson had the exact properties predicted by Dirac–a great feat of theoretical physics. With the discovery of the positron came the first confirmation of antimatter.

Around the same time, there was much experimental progress in explaining the structure of the atom. After discovering the electron, Thompson (incorrectly) proposed a model of the atom in which electrons orbited within a dispersed positive medium the size of the atom–often referred to as the "plum pudding" model. By investigating the deflection of heavy, positively charged alpha particles, Rutherford deduced in 1911 that all positive charge in the atom must be confined in a very small space at the center instead of uniformly

distributed throughout [**49**]. Investigation of this concentrated charge birthed the field of nuclear physics.

Not a decade later, Rutherford follows up his discovery of the nucleus by dissecting the atom further. He finds that in energetic $\alpha +^{14} N$ collisions, positive particles the mass of the Hydrogen atom are released from the target nucleus. Rutherford dubbed these particles protons and proposed that they comprised the nucleus. Not long after, James Chadwick shows there must be another particle in the nucleus, analogous to the proton but with no electric charge [**50**]. Due to its neutral nature, he calls it the neutron.

However, the introduction of the neutron exacerbates an old problem in nuclear physics: if all components of the nucleus are positive or neutral, how does it remain intact? To overcome the Coulomb repulsion between the protons, Hideki Yukawa proposes a short-range force, often referred to as the "nuclear force" [**51**]. As opposed to the quantum theory of electrodynamics in which the massless photon is the force mediator, Yukawa's force is intermediated by a massive boson. By having a massive force mediator, the interaction is naturally limited in space by Heisenberg's uncertainty principle, allowing for a force which binds strongly at close distances but rapidly loses strength beyond nuclear distances. Yukawa predicts this new boson to have a mass around 100 MeV/c^2. After a false start with the muon [**52**], a particle possessing the characteristics predicted by Yukawa was found a decade later and dubbed the pion [**53**]. Though refined over time, pion exchange remained the dominant theory of nuclear interaction for the next three decades.

By the end of the '50s, an array of new subatomic particles had been discovered with a variety of properties. A spray of mesons and baryons covering a range of masses, spins, parities, and charges filled data tables. Every new particle complicated the once simple model of particle physics. Kaons and some hyperons, though easily created, were found to have long lifetimes, leading to the introduction of a new quantum number strangeness, which is preserved in all interactions except the slow-acting weak force. "Who ordered that?" quipped Nobel laureate Isidor Rabi at the discovery that the muon was a "heavy electron" [**54**]. "If I could remember the names of all these particles, I would have become a botanist," bemoaned Fermi [**55**]. New particles were being discovered every month with

seemingly no end in sight and no underlying pattern. It was a heyday for experimental physics, but the theorists were stumped.

In 1961, Murray Gell-Mann proposed a formulation where the baryons and mesons were organized into sets based on spin and arranged internally by underlying quantum numbers. This approach, known as the Eightfold Way, predicted the existence of a particle with a charge of -1, a strangeness of 3, spin of 3/2, and a mass around 1.68 GeV/c^2 dubbed the Ω^-. Shortly thereafter, in 1964, a particle with properties very close to those predicted was discovered at Brookhaven National Lab [**56**].

That same year, Gell-Mann came to understand that the Eightfold Way could easily be explained by using elementary fermions to construct the hadrons. Combining two creates a bosonic meson; combining three creates a fermionic baryon. Gell-Mann proposed the existence of a new fundamental particle, which he called a "quark," which came in three flavors: up, down, and strange. Furthermore, these odd new particles carried fractional charges of $2/3e$ and $-1/3e$, a property of no particle yet observed. Unfortunately, the existence of quarks immediately led to a new problem: the Ω^-, the darling prediction of this great theory, required three strange quarks to be in an S state with their spins aligned, creating a paradox in which three fermions were in a symmetric wave function, a physical state not allowed by Fermi statistics. As a solution to this conundrum, it was proposed that quarks had another quantum number called color, allowing them to be in an overall antisymmetric state. It shortly came to be understood that color was more than a convenient out but instead a type of charge analogous to electric charge, but with three charges instead of one.

The quantum concept of "color" has nothing to do with the visual perception of electromagnetic vibrations by the human cortex, but there are conceptual parallels. First, there are three color charges–red, green, and blue–just as there are three primary colors in light. Color can be removed in two ways: pair a colored object with its anti-color (red with anti-red, blue with anti-blue, etc.) or combine three different colors or anti-colors to form white. The pairings form mesons; the triplets form baryons. Second, this force is also governed by a gauge boson analogous to the photon except it caries the charge it mediates (color) and comes in a set of eight, collectively dubbed the gluon. Collectively, the quarks

and gluons are known as partons, originating from the concept that they are the "parts" of the protons and neutrons. Confirmation that the proton is not fundamental but indeed contains point-like objects came in 1968 with deep inelastic scattering (DIS) results from $e - p$ collisions at the Stanford Linear Accelerator [**57**, **58**].

The search for the free quark was on. Unfortunately, no one could seem to find these elusive particles except in DIS experiments. Could it be that the quark did not really exist but was just a convenient mathematical tool? Fortunately, the confusion was short lived as, in 1973, a mechanism known as "asymptotic freedom" was introduced independently by Politzer [**59**, **60**] and Wilczek and Gross [**61**]. They proposed that, unlike all of the other forces, the force binding the quarks together gets stronger as the distance *increases*. This means quarks behave semi-freely while within hadrons, but cannot get more than a short distance from their partners, a property known as confinement. If a quark is imparted with extra energy, such as in DIS, it can escape the confines of the hadron. However, as the quarks get further and further apart, it becomes energetically favorable to create a new quark-antiquark pair out of the vacuum between the diverging quarks which can then recombine with the fleeing quark to create new hadrons. Hence, quarks remain bound within hadrons under ordinary conditions and, if freed, form themselves into new hadrons. In other words, colored objects cannot exist in vacuum; we can only observe uncolored (i.e. "white") objects. Together with the concept of color charge, this theory detailing the interactions of quarks and gluons came to be known as quantum chromodynamics (QCD).

The quark family grew during the November Revolution of 1974. On the same day, researchers at SLAC and BNL announced the discovery of a neutral, zero strange, spin-1 meson with a mass of around 3.1 GeV/c^2 [**62**, **63**]. The J/ψ, doubly named due to the simultaneous nature of its discovery, was soon understood to be comprised of a new, heavier flavor of quark called the *charm*. This new quark had many of the properties of the up, but was much heavier, just like how the strange quark looks similar to a heavy down. The lighter up and down quarks were paired to make the first generation of quarks and the charm and strange make the second. Along with observed CP violation in Kaon decays, this suggested a third generation, whose members were uncreatively named *top* and *bottom* [**64**, **65**]. Despite a false start [**66**], the bottom's analog to charm's J/ψ, the Υ

meson, was discovered at Fermilab in 1977 [**67**]. Due to the quick discovery of the bottom, the top's existence was accepted as highly likely. Evidence, however, did not come until 1994 [**68**, **69**].

Along with electroweak theory and the Higgs mechanism, QCD formed the final piece of what is still the golden beacon in fundamental physics: the Standard Model. This 19-parameter model attempts to describe all fundamental particle interactions through all forces except gravity. The Standard Model successfully predicted all fundamental particles discovered since the mid-'70s: the Z^0 and $W^{\pm}$ [**70**, **71**] bosons, mediators of the weak nuclear force, discovered in the early '80s, the τ neutrino [**72**], and, ultimately, the Higgs boson [**73**, **74**]. While not a complete theory of physics, it has proven to be amazingly successful at providing experimental predictions.

2.2. The Standard Model

The Standard Model of particle physics describes the dynamics of all fundamental particles with respect to all forces except gravity. In the Standard Model, particles fall into one of two categories: bosons and fermions. Spin, an intrinsic quantization of angular momentum and property of all particles, is the differentiating factor between these two categories. Particles with integer spin are bosons and follow Bose-Einstein statistics; bosons must have even wave functions, which are unaffected by the exchange of two particles. This allows an unlimited number of bosons to be in the same quantum state and even same position, leading to such phenomena as the Bose-Einstein condensate. Fermions are those remaining particles with half-integer spin. These follow Fermi-Dirac statistics, in which wave functions change sign when two particles are swapped. This gives rise to the Pauli exclusion principle, which, unlike Bose statistics, *forbids* fermions from having identical quantum numbers.

In the Standard Model, all matter is fundamentally comprised of fermions and the fundamental forces are mediated by vector bosons (see Fig. 2.1). Fundamental fermions can be further subdivided into quarks and leptons. The quarks, shown in violet, come in three pairs, or generations, each with its own two flavors: up and down, charm and strange, and top and bottom. The quarks are the only fermions that interact via the strong force, which is mediated by the gluon. The leptons, which come in three generations like the quarks, are

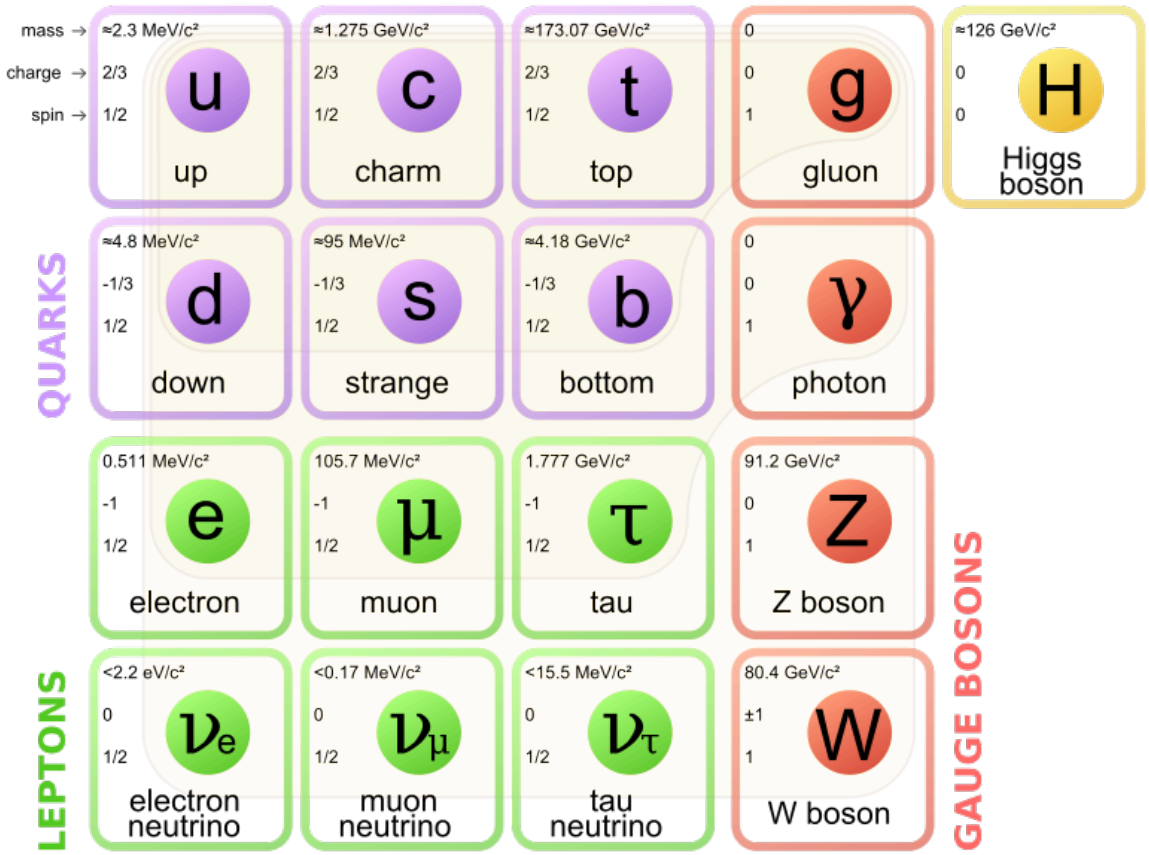

FIGURE 2.1. A summary of the particles in the Standard Model as well as their masses, charges, and spins [**1**]. The six quarks are shown in violet with rising generations from left to right. The fundamental leptons along with their associated neutrinos are in green. Together, the quarks and leptons contain all fundamental fermions. The vector bosons, which mediate the forces, are in red. In yellow is the recently discovered Higgs boson.

shown in green. Each generation contains a charged lepton and its corresponding neutrino. With the photon as a force carrier, the charged leptons interact electromagnetically with each other as well as with the quarks. The neutrinos are uncharged and only interact via the weak nuclear force, to which all particles couple. In the Standard Model, the neutrinos are massless, but discrepancies in the observation of solar neutrinos suggests otherwise [**75**, **76**]. The massive vector bosons, Z^0 and $W^{\pm}$, mediate the weak force. Finally, the recently discovered Higgs boson is shown in yellow. Unlike the other bosons in the Standard Model, the Higgs does not mediate a force but is instead an excitation of the Higgs field which gives rise to the masses of the fundamental particles.

The Standard Model also contains a mirror antiparticle for each particle shown in Fig. 2.1. Antiparticles have the same mass as their standard counterparts but with their quantum numbers, such as charge, flipped. All fermions have unique antiparticles: up and anti-up, electron and positron, bottom and anti-bottom. Almost all of the bosons, however, are their own antiparticle. The only exception are the W^+ and W^- bosons, which are each other's antiparticles.

The Standard Model describes three of the four known fundamental forces: the electromagnetic and the strong and weak nuclear forces. Of these, the aptly named weak nuclear force, modeled as a SU(2) group, is by far the least powerful but couples to all particles in the Standard Model except photons and gluons. Due to the large mass of its mediator bosons, 80.4 GeV/c^2 for the W bosons and 91.2 GeV/c^2 for the Z, the range of the weak force is limited to subnuclear scales. This force is responsible for the element-changing reaction, β-decay, in which a nucleon transmutes through creation of an electron or positron and neutrino via emission and decay of a W boson. The weak interaction allows quarks to change flavor through exchange of W bosons. However, since W bosons carry a unit of elementary charge, quarks need to change into a quark of a different charge when exchanging a W. This in turn, means the quark must also change flavor. Hence, ups, charms, and tops can only change into downs, stranges, and bottoms (see Fig. 2.2). The strength of the coupling between flavors is described by the Cabibbo-Kobayashi-Maskawa (CKM) matrix. The neutral Z boson mediates elastic scattering of weakly interacting particles through momentum and spin transfer. However, the exchange of a Z, known as a neutral-current interaction, never changes a quark's flavor.

Electromagnetism describes the dynamics of electrically charged particles (the quarks and massive leptons) and photons. At the level of fundamental interactions, this is described by the theory of quantum electrodynamics (QED), formalized by a U(1) symmetry group. Along with being free, observable particles in their own right, photons act as the force mediator between charged particles. Unlike the vector bosons in the weak force, the photon is massless–one of the reasons, along with the photon being electrically uncharged, that electromagnetism can act at unlimited distances. The electromagnetic coupling constant, $\alpha = e^2/4\pi\epsilon_0\hbar c = 1/137$, while small enough to allow calculations to be done perturbatively,

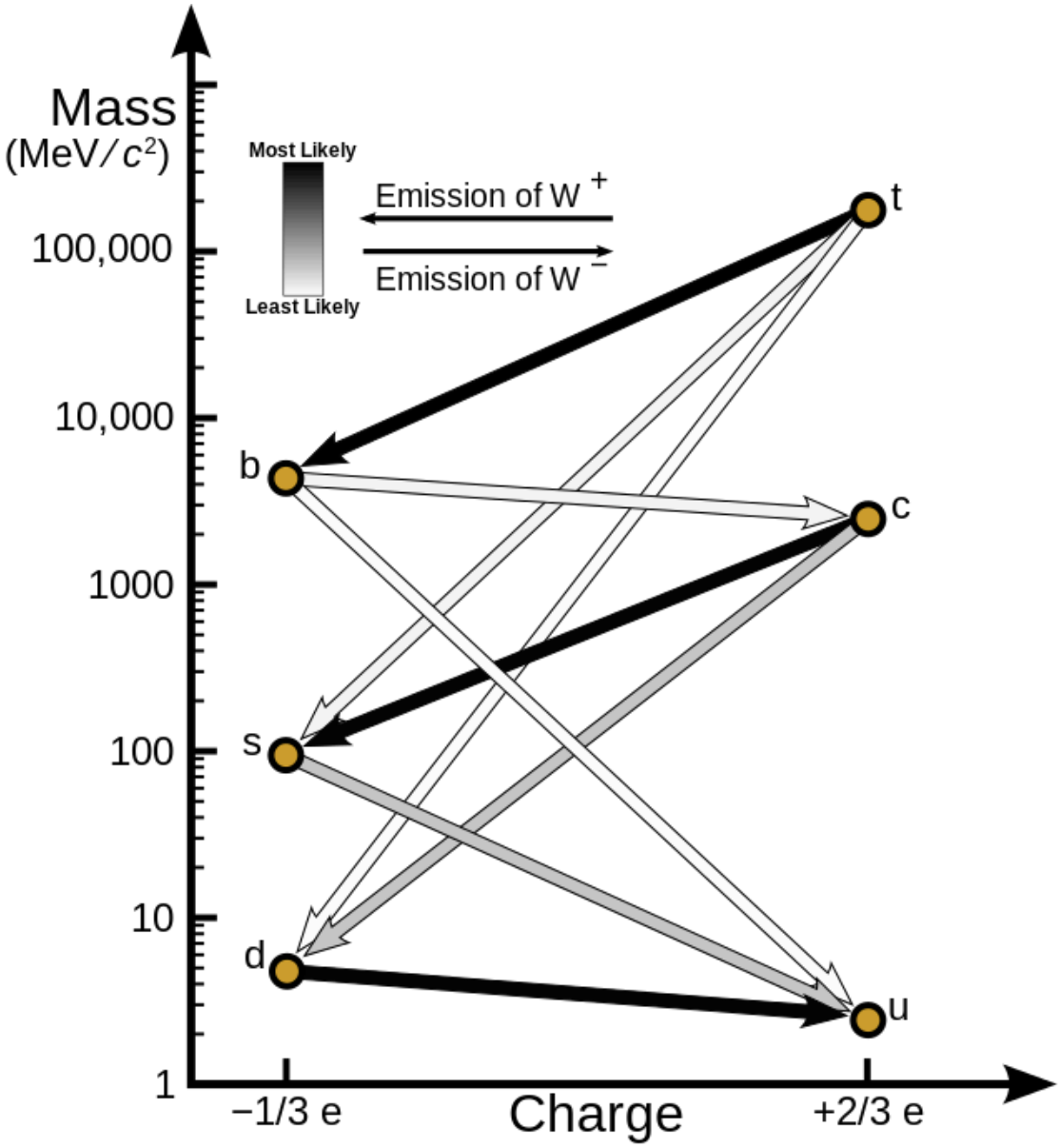

FIGURE 2.2. The six elementary quarks arranged by mass and charge and their allowed interactions with W bosons [**2**]. Arrows depict allowed flavor-changing decays. Arrows pointing from right to left are mediated by W^+ bosons; left-to-right arrows depict those mediated by a W^-. Darker arrows denote stronger couplings in the CKM matrix; lighter, weaker.

is a factor of approximately 10^4 greater than that of the weak force which is itself around 10^{32} times greater than gravity's. Taking both its relative strength and infinite range into account, it is little surprise that electromagnetism is the most familiar of the forces described by the Standard Model.

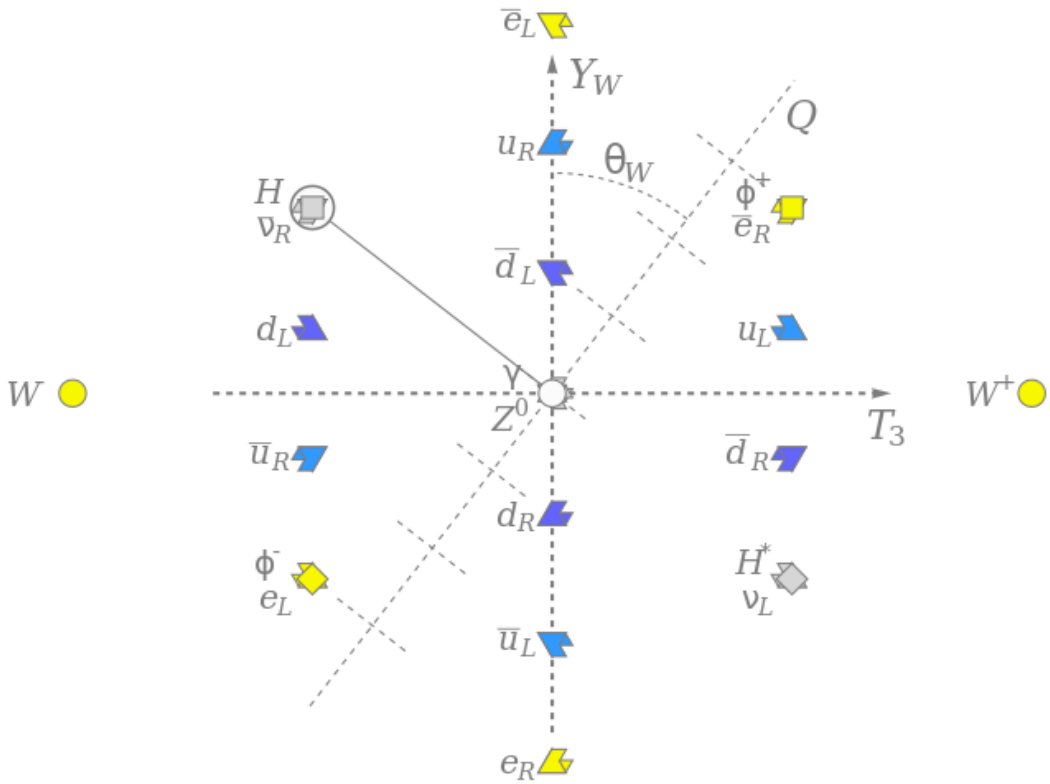

FIGURE 2.3. The fundamental particles of the Standard Model arranged by weak isospin (T_3, x-axis) and weak hypercharge (Y_W, y-axis) [**3**]. Introduction of the Higgs (upper-left quadrant) breaks the weak isospin-hypercharge symmetry, picking out a specific Weinberg angle, θ_W, and orienting the charge axis (Q).

The theories of the weak force and QED combine to form one of the theoretical and experimental pillars of the Standard Model: electroweak theory. At very high energies and temperatures ($\sim 10^{15}$ K or 100 GeV), the distinction between QED and the weak force breaks down and they act as a single, unified force, described by a $SU(2)\otimes U_Y(1)$ gauge group, where the unitary group, $U_Y(1)$, now represents the symmetries of weak hypercharge

(the vertical Y_W-axis in Fig. 2.3) as opposed to U_{EM} which represents the symmetry of the electric charge in QED (slanted Q-axis in Fig. 2.3). This combined force is mediated by four *massless* vector bosons: W^+, W^0, W^-, and B^0. At lower energies, this hypercharge symmetry breaks down, leading to spontaneous symmetry breaking which gives rise to the masses of the $W^\pm$ and Z bosons. At breaking, the W^0 and B^0 bosons mix to form the previously mentioned photon and the Z^0:

$$\begin{pmatrix} \gamma \\ Z^0 \end{pmatrix} = \begin{pmatrix} \cos\theta_W & \sin\theta_W \\ -\sin\theta_W & \cos\theta_W \end{pmatrix} \begin{pmatrix} B^0 \\ W^0 \end{pmatrix} \tag{2.1}$$

where θ_W is the Weinberg angle, one of the 19 free parameters of the Standard Model. It is through this breaking that the $W^\pm$ and the newly formed Z^0 acquire mass. The process of symmetry breaking is brought about through the Higgs mechanism. Introducing the Higgs breaks the weak isospin-hypercharge symmetry and picks out a specific Weinberg angle for the charge axis as seen in Fig. 2.3.

The final force contained in the Standard Model is the strong nuclear force. In its pure form, the strong force, formalized in the theory of quantum chromodynamics (QCD), describes how quarks interact with each other through the exchange of gluons. QCD is a non-Abelian SU(3) gauge theory, meaning some or all of the elements of the group do no commute. Somewhat analogously to the single charge and its anticharge in electromagnetism, QCD interactions are governed by three color charges, red, blue, and green, and their anti-charges. Like the photons of electromagnetism, gluons are massless, spin-1 bosons. Unlike photons, gluons carry the charge they mediate and can therefore self-interact. This leads to the existence of 3- and 4-gluon vertices in QCD which makes perturbative calculations much trickier and gives rise to the phenomenon of confinement.

There are two properties which make the strong force unique amongst the forces beyond its strength: confinement and asymptotic freedom. Confinement comes from the lack of diminishment of the strong force with distance. Unlike the weak force and electromagnetism, the strong force does not fall off with distance. Any quark, upon attempted isolation, will quickly be pulled back to its original hadron or will combine with a new quark created out of the vacuum with its antipartner to form a new, colorless hadron. This leads to our

inability to find a free quark and necessitates their study while confined within hadrons or while acting quasifreely within a QGP.

Asymptotic freedom can be though of as the flip side to confinement: as the distances between colored objects decreases, the strong force becomes weaker. This means that at high energies (synonymous with short distances), the strong coupling constant, α_s, shrinks. Fortunately, this makes α_s small enough at high energies that perturbative calculations involving the strong force become viable. However, this is a double edges sword as α_s rises to large values when doing calculations involving heavy quarks, complicating predictions. This leads to a common classification in particle physics: soft vs. hard processes. Hard processes are those energetic enough that α_s is of the magnitude where perturbative calculations can be performed; soft processes are those where it is not. This change in α_s with energy is known as a running coupling constant and is one of the key features of QCD.

Though the Standard Model has had great success at making predictions for high energy physics, it still has its shortcomings. The most notable of these the lack of a description of gravity, the earliest known fundamental force. Theoretical work known as "string theory" hopes to rectify this tension. In the Standard Model, neutrinos are massless objects. However, study of the solar neutrino flux comes up with "missing" electron neutrinos. The best theory to describe this phenomenon requires massive (though still light) neutrinos whose mass eigenstates are different than their flavor eigenstates. Thus, while freely propagating in their mass eigenstate, neutrinos oscillate between flavors–violating another pillar of the Standard Model: flavor conservation [**75**, **76**].

Dark matter, first hypothesized in the 1930s, has no place in the Standard Model. This matter, invoked to explain why the orbital velocities of stars in the Milky Way and later other galaxies do not match what is predicted by general relativity using only the observable mass, does not interact via the electromagnetic force. This required a particle which interacted only via gravity (and possibly the weak force); a theory yet unproven but still at the forefront. Nor does the Standard Model contain dark energy, the current leading explanation for the accelerating expansion of the universe.

Despite these shortcomings, the Standard Model has had remarkable success at describing our universe at a fundamental level and can undoubtedly be regarded as one of the greatest scientific works of human achievement.

CHAPTER 3

Physics of the Quark-Gluon Plasma

As outlined in the previous chapter quarks and gluons are tightly bound within hadrons in everyday conditions. However, due to the running coupling of QCD, at extremely high energies and densities, partons behave in a quasifree fashion. Baryons and mesons, the traditional bags which hold partons, dissolve, allowing the colored objects to act as independent, fundamental particles instead of being bound as part of a larger object. This dense bulk medium is known as the quark-gluon plasma (QGP).

3.1. Lattice Calculations of the QGP

Calculations using QCD are notoriously complex. As mentioned in Chapter 2, one approach to this problem is to factorize QCD and approach the problem perturbatively. Unfortunately, at low energies where α_s is large, these calculations diverge. A common method to analyze QCD at this energy is known as lattice QCD. In lattice analyses, both time and space are discretized onto a lattice, hence the name. The action is calculated using the QCD Lagrangian which is then used to advance the simulation by one step in time.

Lattice QCD calculations provide great evidence for the onset of deconfinement. Energy density calculations from lattice simulations show a sudden rise starting at temperatures slightly below 200 MeV as can be seen in Fig. 3.1 [**4**]. This behavior is indicative of a phase transition. At the critical temperature (T_c), all additional energy goes into creating new degrees of freedom instead of heating the matter. The exact value of the temperature of the phase transition varies depending on the specific tuning parameters used in the calculations (such as lattice spacing, number of quark flavors, temporal extent, and weather quarks are included at all or just gluons), but all lattice simulations see an onset of deconfinement in the range 150 and 190 MeV for vanishing baryon chemical potential (i.e. net fraction of matter over antimatter) [**77**].

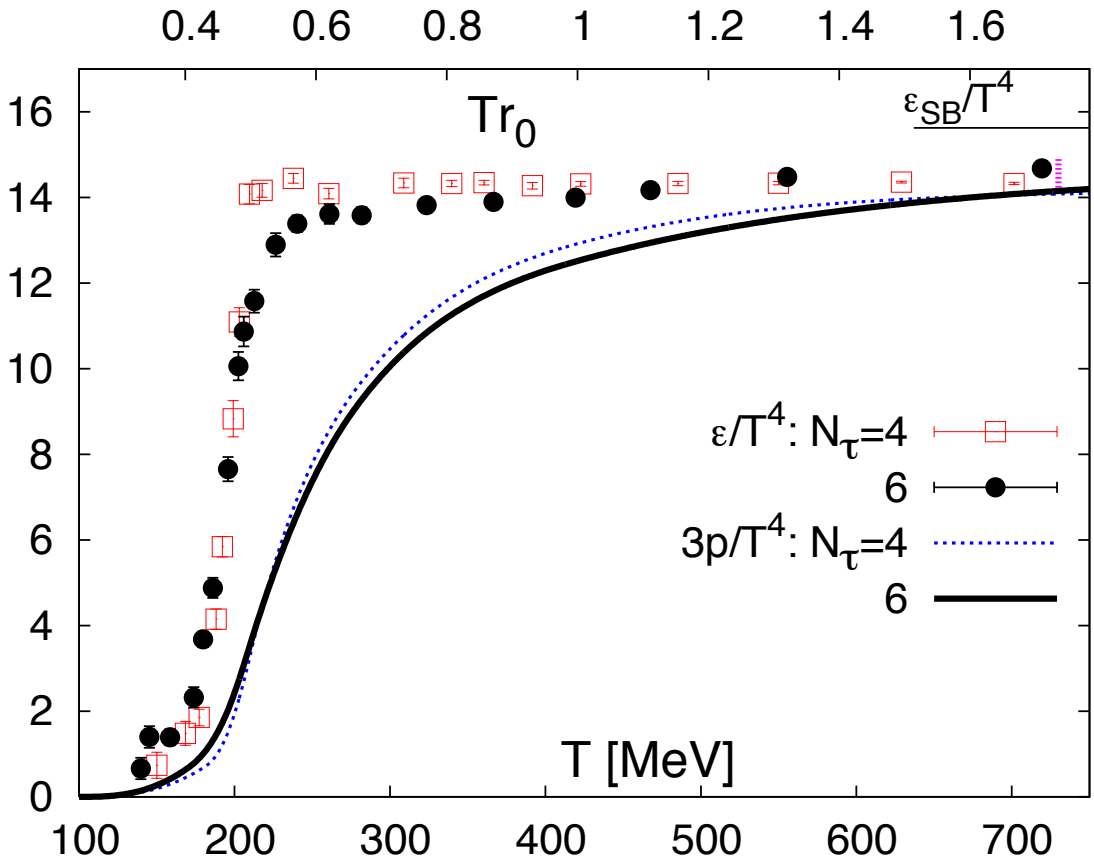

FIGURE 3.1. Energy density and triple the pressure as a function of temperature obtained from lattice calculations [**4**]. The sharp rise in energy density just below 200 MeV is indicative of a phase transition. The Stefan-Boltzmann limit (i.e. the energy density of an ideal gas) is shown in the upper right.

As temperature increases, the couping between partons weakens. Fig. 3.2 shows the running quark-quark coupling coefficient as a function of distance [**5**]. The solid curve shows the value in the vacuum. As temperature increases, the strength of the coupling coefficient at large distances falls. At around $1.25T_c$, the coupling becomes constant and at higher temperature begins to *fall* with increasing distance.

The free energy is oft-used as the heavy quark-antiquark potential. In a vacuum, the potential turns linear at large distances, forever growing in magnitude without asymptote. As can been seen in Fig. 3.3, the free energy asymptotes at lower and lower energies as

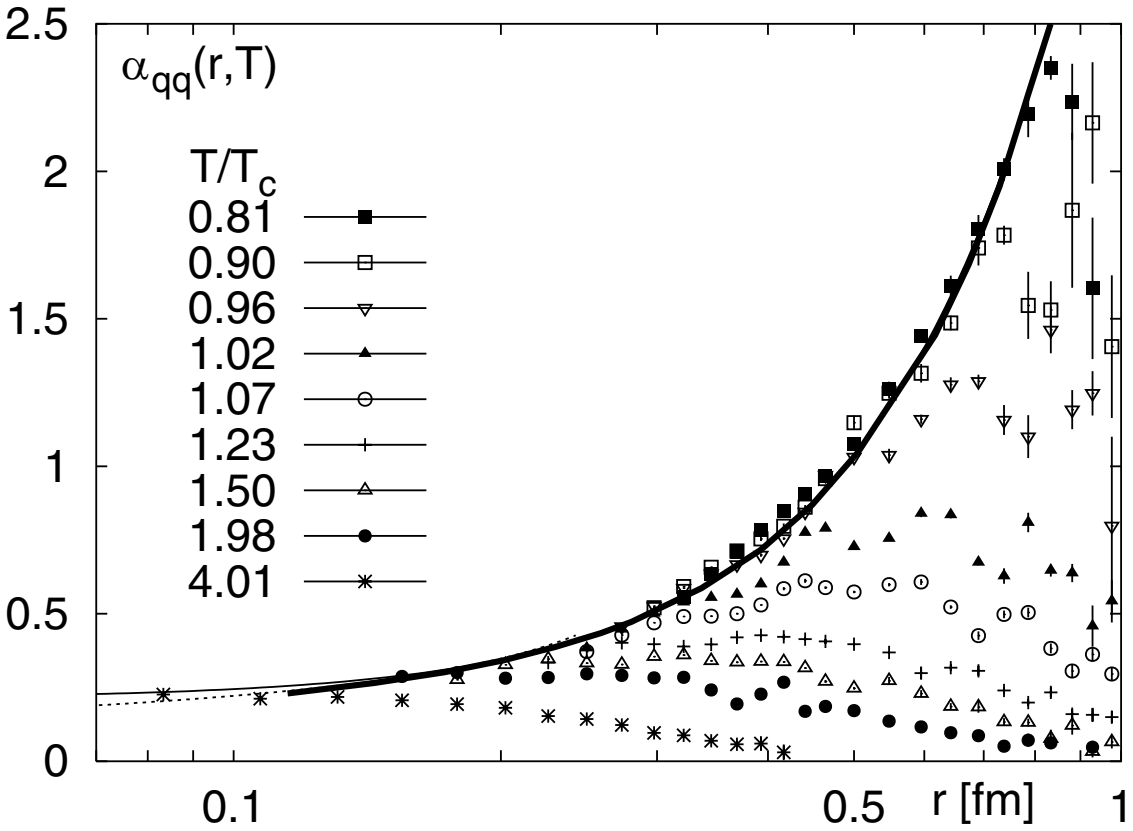

FIGURE 3.2. The running QCD heavy quark-quark coupling constant from 2-flavor lattice QCD calculations [**5**]. At temperatures above T_c, the couping constant at quarkonium interquark distance scales ($\sim 0.5 - 1$ fm) rapidly decreases, inhibiting the formation of loosely bound heavy quarkonia.

the temperature increases. Thus, as the temperature increases, the effective binding energy decreases until heavy quarks cannot bind.

3.2. Experimental Evidence for the QGP

While no single measurement is a smoking gun, there does exist a large body of experimental results, which, when taken as a whole, is strong evidence for the formation of a QGP in heavy-ion collisions at RHIC and the LHC.

3.2.1. Jet Quenching. As discussed in the previous chapter, colored partons ejected from hadrons in high-energy collisions quickly pull new quark-antiquark pairs out of the vacuum to form new, colorless hadrons. Due to the high transverse momentum of the initial parton, the spray of newly formed hadrons is highly collinear, forming what is known as a

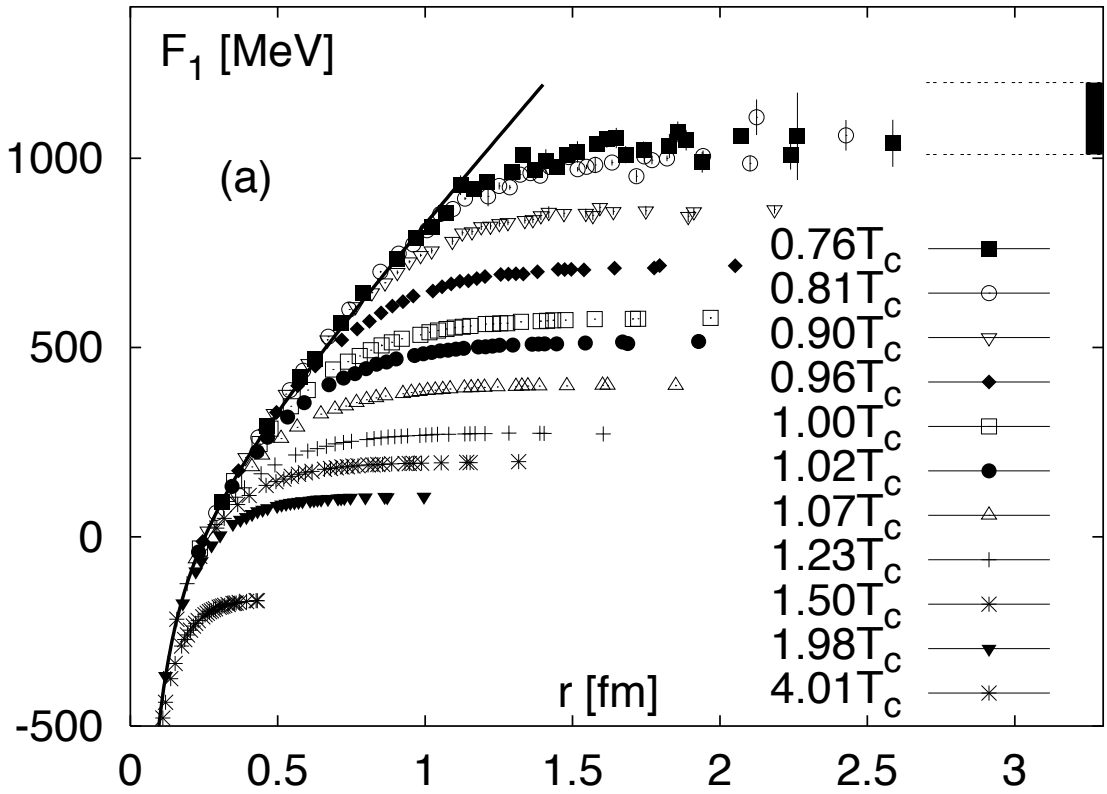

FIGURE 3.3. The color singlet quark-antiquark free energy from 2-flavor lattice QCD calculations [**5**]. The solid line shows the results in the vacuum. The free energy flattens off at lower and lower energies as temperature increases.

jet. By combining the kinematic information of these jets, we can reconstruct the kinematic properties of the initial parton. Conservation of momentum requires that the transverse momentum of a jet be balanced by other particles. In leading-order processes, this is another jet, though second-order processes can lead to a third parton, which creates a third jet which must, by definition, break the azimuthal symmetry. As a side note, the observation of three-jet events in $\Upsilon(1S) \rightarrow q + \bar{q} + X$ decays were the first experimental evidence of the existence of gluons, as $\Upsilon(1S) \rightarrow q + \bar{q} + X$ requires an X without electromagnetic charge in order to conserve all quantum numbers [**78**–**80**]. Later observation of three-jet events in $e^+ + e^-$ collisions by TASSO [**81**], MARK-J [**82**], PLUTO [**83**], and JADE [**84**] at the PETRA collider. Altogether, this means in the leading-order, 2-jet event, the jets must be back-to-back in azimuth (see Fig.3.4, black curve).

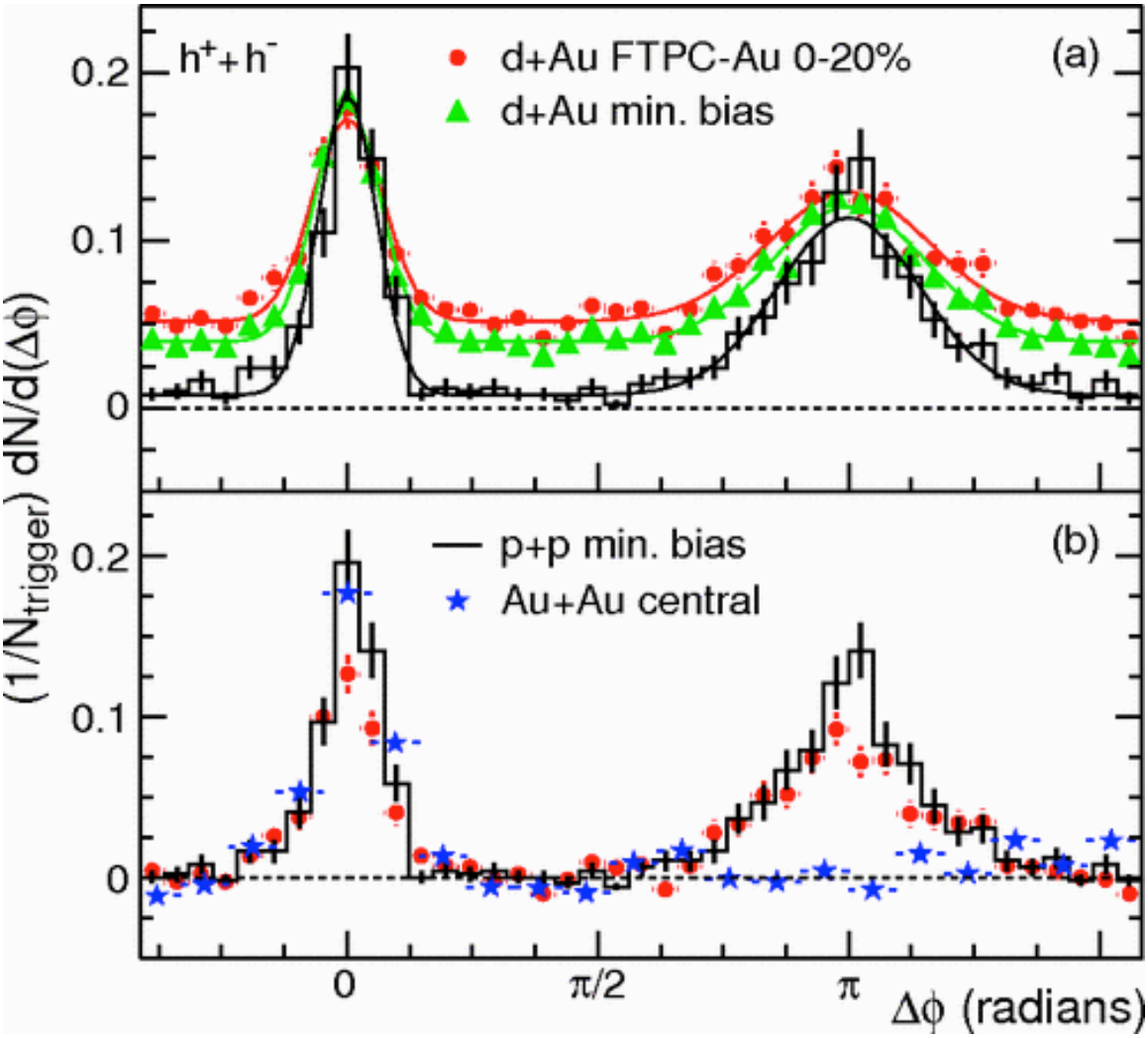

FIGURE 3.4. Dihadron correlations in $p+p$, $d+\mathrm{Au}$, and $\mathrm{Au}+\mathrm{Au}$ collisions as measured by STAR [**6**]. Plot (a) shows results for $p+p$ (black line), min. bias $d+\mathrm{Au}$ (green triangles), and 0-20% centrality $d+\mathrm{Au}$ (red circles). Note the peaks at both $\Delta\phi \sim 0$ and $\Delta\phi \sim \pi$, indicating the presence of jets and their azimuthally balanced partners. Plot (b) shows the same $p+p$ and central $d+\mathrm{Au}$ results (pedestal-subtracted), as well as central $\mathrm{Au}+\mathrm{Au}$ results (blue stars). Note the lack of an away-side ($\Delta\phi \sim \pi$) peak in $\mathrm{Au}+\mathrm{Au}$, indicating jet quenching.

In the presence of a colored medium, such as the QGP, these partons need to traverse intense color fields. These conditions induce energy loss in the traversing partons through processes such as gluo-bremsstrahlung, transferring momentum from the hard parton to the bulk medium which ultimately manifests itself as a surfeit of soft particles in the final state. When parton scattering occurs near the edge of the QGP, one parton can immediately

hadronize in the vacuum to form a jet whereas the other jet must traverse the QGP, losing energy in the process and leading to a jet-energy imbalance. In 2003, STAR found evidence for this phenomenon in dihadron correlations, in which the correlation between leading (highest energy) hadrons is used as a proxy for the total jet kinematics [**6**]. In both $p+p$ and $d+\mathrm{Au}$ collisions, azimuthal correlation functions see both a main jet ($\Delta\phi \sim 0$) and an away-side jet ($\Delta\phi \sim \pi$). However, in $\mathrm{Au}+\mathrm{Au}$ collisions, the away-side jet is suppressed as one would expect from the presence of a colored medium (Fig. 3.4b, blue stars). In this case, the $d+\mathrm{Au}$ results are as important of a control as the $p+p$ results for they indicate that the mere presence of a large amount of cold nuclear matter is not sufficient to suppress jets, but that the observed suppression in $\mathrm{Au}+\mathrm{Au}$ collisions requires the presence of a deconfined and extended color medium.

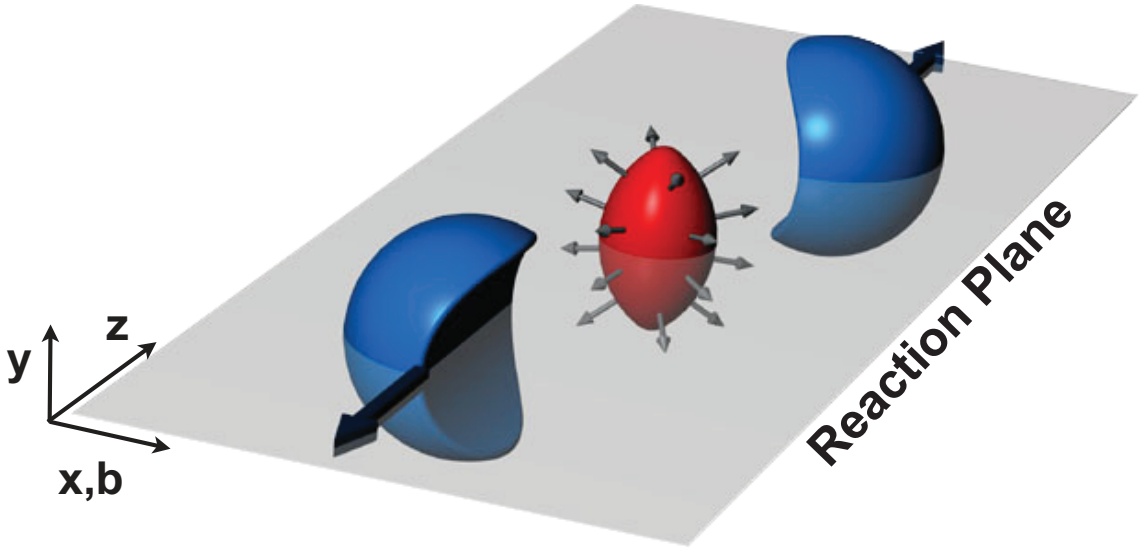

FIGURE 3.5. Almond-shaped interaction region (red) created by a non-central heavy-ion collision [**7**]. The remnant spectator nucleons are shown in blue. The plane defined by the impact parameter and beam line is called the reaction plane (gray).

3.2.2. Elliptic Flow. In non-central collisions, the overlapping region of the two colliding nuclei has an almond-like shape (see Fig. 3.5, red object). Once thermalized, this asymmetric spacial profile leads to differing rates of expansion of the surface of the QGP due to non-isotropic pressure gradients. This effects manifests itself as a boost in momentum

of the final-state particles along the reaction plane when compared to those perpendicular to the plane. By performing a Fourier decomposition of the measured distribution of particles, we can extract the second harmonic, known as v_2, to give us information about this momentum anisotropy often referred to as *flow*. STAR has measured flow over a wide range of systems, energies, and particles [**85**–**93**]. Analysis has shown that the momentum distribution for soft hadrons–those particles most affected by bulk movement such as elliptic flow–can be linked to their quark content, giving further evidence for a medium with partonic degrees of freedom [**88**]. Studying the magnitude and properties of this effect gives us insight into the bulk properties of the QGP, such as its viscosity and equation of state. Furthermore, since flow develops from the anisotropy of the initial collision, studying flow gives us insight into initial conditions of the system. To that end, much study has recently gone into measuring and understanding higher harmonics produced in heavy-ion collisions. Non-zero measurements of v_3 and v_4 are currently understood to be manifestations of fluctuations of the initial nuclear geometry prior to impact–a property not of the QGP but of everyday cold nuclear matter [**88**, **94**].

3.3. Quarkonium Production and Suppression

Another pillar of evidence for the formation of a QGP and the topic of this thesis is heavy quarkonium suppression. Quarkonia are the family of mesons formed from pairs of heavy quarks and their own antiquarks. Quarkonia provide a unique probe of the QGP as their valence quarks are massive enough to be treated nonrelativistically, greatly simplifying modeling their interactions with the QGP. In the presence of a deconfined plasma, color charges are effectively screened by the free partons at distances larger than the Debye radius. If the Debye radius is short enough, it can screen the interquark potential in heavy quarkonium such as J/ψ, η_c, Υ, and χ_b, causing the quarks to dissociate before the mesons can decay into signatures detectable by our instruments. First proposed in 1986 by Matsui and Satz [**95**], quarkonium suppression is one of the most studied signatures of the QGP.

3.3.1. Quarkonium Production. Though still an open theoretical question, there are three leading models for quarkonium production in high-energy collisions: the Color Singlet Model (CSM), the Color Evaporation Model (CEM), and non-relativistic quantum

chromodynamics (NRQCD). Herein, we will only discuss the later two; for further information on NRQCD, please consult Ref. [**96**]. In the CSM, as the name implies, the initial heavy quarks are created in a color singlet state. Since they have no excess color to shed, the pair can hadronize on their own, retaining their initial spin. In the CEM, there is no constraint on the initial condition of the heavy quarks except that they be below the mass threshold for $B\bar{B}$ meson production. The quarks interact with the local color field to shed their excess color. The final-state Υ are then a fixed fraction of these quarks, regardless of production energy. Current estimates put the fraction of $b\bar{b}$ pairs which form Υ at around 2% [**35**].

Results from the 2006 $p+p$ run are shown in Fig. 3.6 [**8**]. The measured Υ(1S+2S+3S) production cross section is shown as a blue star. Predictions using the CEM are more in line with these results, though one cannot dismiss the CSM outright given the size of these error bars. The 2009 $p+p$ dataset analyzed in this thesis contains ~ 3 times the statistics shown here.

3.3.2. Cold Nuclear Matter Effects. In order to quantify suppression effects due to the presence of hot nuclear matter, we must first control for any initial state effects that might arise from the parent partons being in a nucleus instead of a free proton. Furthermore, there are final-state effects such as secondary scattering and absorption from spectator nuclei and hadronic co-movers.

The momentum distribution of gluons, sea quarks, and valence quarks as a fraction of the parent hadron's momentum is known as a parton distribution function (PDF). The PDF of a nucleon is modified while inside a nucleus, complicating the interpretation of quarkonium suppression. By modifying the fraction of partons at each momentum, the number of partons available at the specific energies required to create Υ mesons changes, changing the rate of production. One parameterization of the changes in the PDF is known as EPS09 (shown in Fig. 3.7) [**9**]. Shown is not the nuclear PDF itself, but the ratio of the nuclear PDF to the unmodified proton PDF. The upper set of plots shows the modifications for carbon; the lower shows lead.

At STAR, Υ are formed mainly via gluons. To form an Υ at midrapidity ($|y| < 1.0$), gluons need an initial p_z around 5 GeV/c. For a nucleon with kinetic energy of 100 GeV,

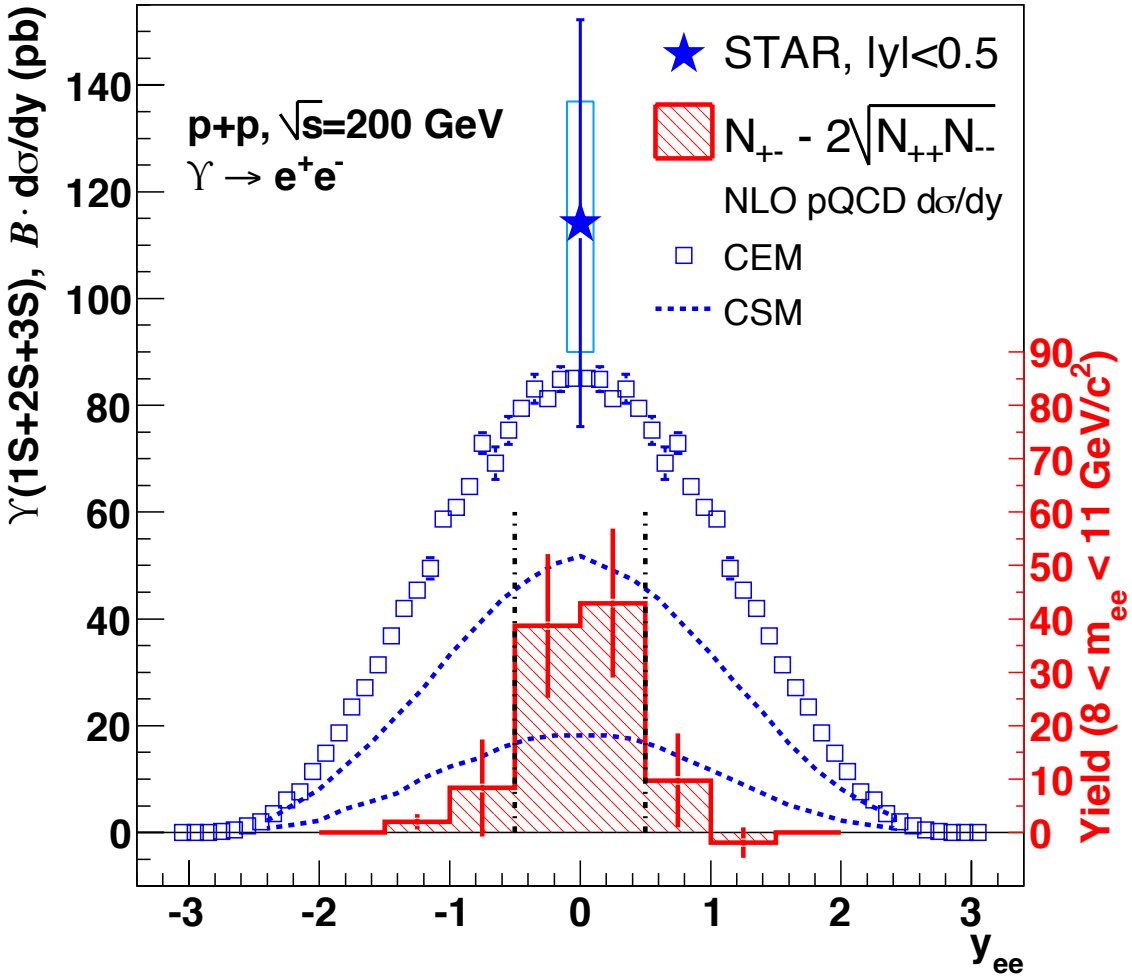

FIGURE 3.6. Υ(1S+2S+3S) production in $p+p$ collisions at $\sqrt{s_{NN}} = 200$ GeV as measured by STAR compared to CSM (blue dashed line) and CEM (blue squares) predictions [8]. Results are from the 2006 $p+p$ run which sampled $\sim 1/3$ the integrated luminosity of the $p+p$ dataset reported on in this thesis.

this amounts to an x of around 0.05. Examining the parameterization for lead (which isn't too dissimilar to that for gold), one can see that this falls right around the transition from shadowing to antishadowing, making Υ production in cold nuclear matter sensitive to the magnitude of both effects. In order to interpret suppression in Au + Au collisions in which it is believed we create hot, deconfined matter, we must first understand how much suppression or enhancement comes from the modification of the parton distribution

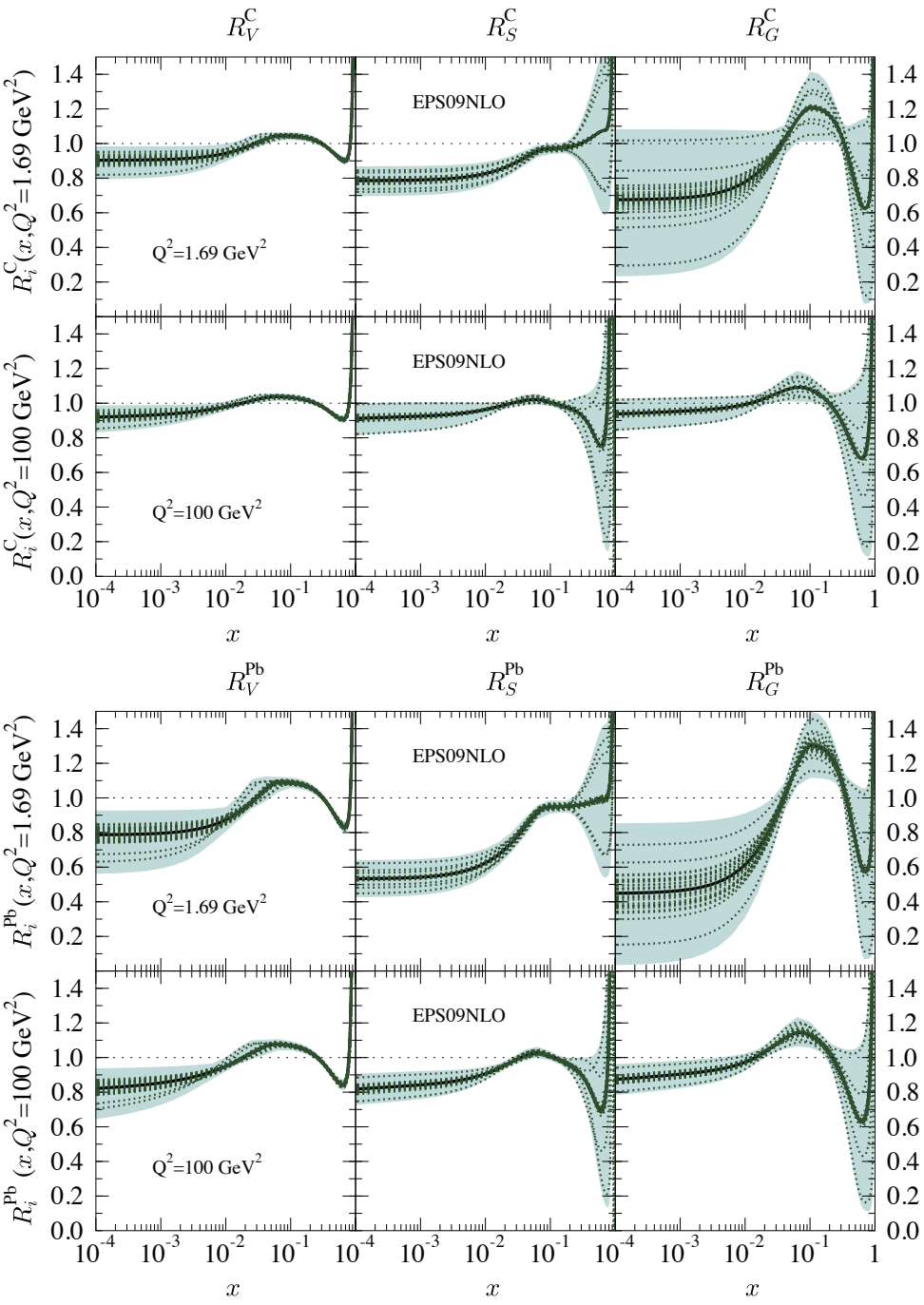

FIGURE 3.7. EPS09 parameterization of nuclear PDFs [**9**]. The upper set of six plots show the modification for carbon; the lower plots show lead. The left column shows the nPDF for valence quarks, the center shows sea quarks, and the right shows gluons.

function. This control is achieved by measuring $d + \mathrm{Au}$ collisions in which the PDFs of the nucleons in the gold nuclei are modified but the incoming deuteron does not carry enough mass or energy to transition into deconfinement.

The other main source of modification of measured final-state Υ is from hadronic interactions. This comes in two flavors. First, the $b\bar{b}$ state can interact with nuclear remnants left over from the Au ion, which can then modify or destroy the state [**39**]. This is known as nuclear absorption. Second, unlike $p + p$ collisions, in $d + \mathrm{Au}$ and $\mathrm{Au} + \mathrm{Au}$ collisions, there are often multiple nucleon-nucleon collisions in a single event. This leads to a much greater number of particles created in the event, making it much more likely that an Υ produced in this event could interact with one. While still hadronizing, the pre-Υ $b\bar{b}$ state can interact with other mesons, causing it to dissociate before forming an Υ or modifying its kinematics via secondary scattering. The interactions coming from new hadrons produced in the event is known as co-mover absorption. Fortunately, while final-state absorption needs to be taken into account to interpret charmonium results [**97**, **98**], the cross section for $\Upsilon(1\mathrm{S})$-hadron interactions is much smaller than that of charmonium [**99**], making interactions with the hadronic medium much less likely and modification negligible at our level of statistics.

3.3.3. Suppression by the QGP. In the study of the QGP, lattice calculations have shown that heavy quarkonium should dissociate at high temperatures and densities. Simulations show that the excited, loosely bound quarkonium states ($\Upsilon(3\mathrm{S})$, ψ') should begin to be suppressed right around the critical temperature, T_c, found to be around 150-190 MeV [**10**,**77**,**100**–**102**]. The lower energy states, such as the $\Upsilon(2\mathrm{S})$ and $\Upsilon(1\mathrm{S})$ are expected to remain bound around the critical temperature. This is due to the fact that the $\Upsilon(3\mathrm{S})$ has a binding energy of only ~ 200 MeV, where as the $\Upsilon(2\mathrm{S})$ has a binding energy around 540 MeV and the $\Upsilon(1\mathrm{S})$ is even more tightly bound at ~ 1.1 GeV. Hence, as the temperature of the medium increases, the more tightly bound quarkonia begin to dissociate.

We examine two main sources of suppression in the QGP: Debye screening and Landau damping. Debye screening is a phenomenon first observed in electromagnetic plasmas. When a charged object is present within a plasma, free objects of the opposite charge will be attracted to it. After a certain distance, the free charges will have accumulated enough density to screen the initial charge, effectively making it invisible beyond what is known

as the Debye radius. This distance is not a fixed quantity but shrinks as temperature increases (note how the potential in Fig. 3.3 weakens with increasing temperature). Hence, as the QGP gets hotter, smaller mesons (larger binding energy) will have their inter-quark pontentials screened. This leads to an effect known as sequential suppression [**103**]. As mentioned before, the loosely bound excited heavy quarkonia are expected to melt around T_c. At higher temperatures ($\sim$ 250 MeV [**10**]), the shorter Debye radius can screen the more tightly bound mesons, such as the J/ψ and Υ(2S). Increasing the temperature even further to around 450 MeV will screen even the strongly bound Υ(1S) ground state.

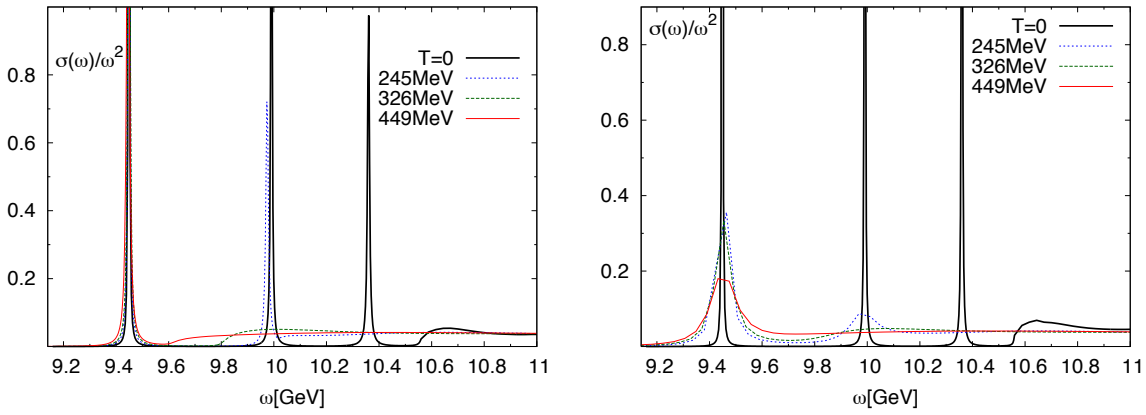

FIGURE 3.8. Bottomonium spectral function calculated with (right) and without (left) the imaginary part of the potential [**10**]. Note the broadening of the line shapes when the imaginary term in included.

The second source of suppression discussed here is known as Landau dampening. In the presence of a colored medium, pQCD calculations show that the inter-quark potentials are modified via the addition of an imaginary term [**10**]. The additional imaginary term leads to a broadening of the quarkonium spectral functions (see Fig. 3.8, right). Note how at even 245 MeV, the Υ(2S) state is so broad as to be but a bump above the $B\bar{B}$ continuum. This implies that any additional kick will cause this state to dissociate into B mesons. This effect is referred to as threshold enhancement.

Besides suppressing quarkonium production, the QGP can also enhance formation rates. In the QGP, quarks are free to traverse the medium as unbound particles. This is not the case in $p+p$ collisions where newly formed quarks quickly hadronize in the vacuum. Hence, unlike in $p+p$ collisions, heavy quarks formed from different partonic collisions

can combine with each other to form quarkonia whereas they would have hadronized into D mesons otherwise. This enhancement is known as recombination. While charmonium production at RHIC and higher energies is affected by recombination, bottom quarks have a much smaller production cross section at RHIC than that of charm (1.34-1.84 μb for bottom [**104**] as compared to 550-1400 μb for charm [**105**, **106**]) making recombination negligible in the analysis of bottomonium production.

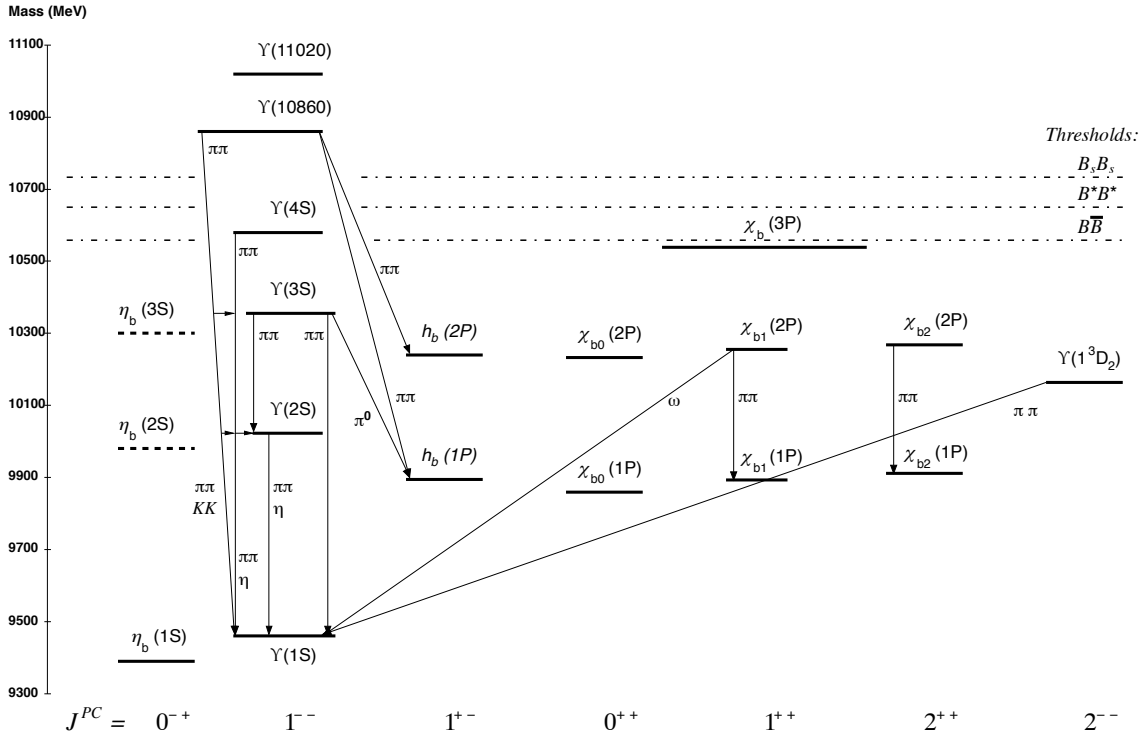

FIGURE 3.9. The feed down pattern of the bottomonium family [**11**]. Note that what we measure as final state Υ(1S) could have been formed as multiple other bottomonium mesons.

There is one final complication to our analysis of bottomonium suppression. Due to their identical quark content, it is common for excited bottomonium states to decay into lower energy states before decaying into the lepton pairs that we see in our detector (see Fig. 3.9). This interwoven decay chain is known as feed-down. Measurements done by CDF at high-p_T have shown that fully 49% of final state Υ(1S) came from Υ(2S) and Υ(3S) decays. We must take this feed-down into account to fully interpret suppression. If we measure that half of Υ(1S) are suppressed, it could be that no initial-state Υ(1S) which

interacted with the plasma were suppressed but all of the Υ(2S) and Υ(3S) were suppressed before they could decay down to Υ(1S).

In the next chapter, we will cover the RHIC accelerator complex used to deliver the relativistic proton and ion beams used for the studies in this thesis.

CHAPTER 4

The Relativistic Heavy Ion Collider

The **R**elativistic **H**eavy-**I**on **C**ollider (RHIC) is a unique and versatile tool for studying the properties of hadronic matter. Situated at **B**rookhaven **N**ational **L**ab (BNL) in Upton, NY, RHIC continues the legacy begun by the success of the **A**lternating **G**radiant **S**ynchrotron (AGS) in the 1960s and its multiple Nobel Prize-winning experiments [**62**, **107**–**109**]. The RHIC facility (shown in Fig. 4.1) is comprised of multiple accelerators and storage rings. RHIC is comprised of two independent synchrotrons, arbitrarily labeled *blue* and *yellow*, which intersect at six interaction points as seen in Fig. 4.2. RHIC is highly versatile, accelerating multiple species (p, d, Cu, Au, U) over a wide range of energies ($\sqrt{s_{NN}}$=7.7-510 GeV). The semi-independent nature of the synchrotrons allows RHIC to easily collide different species of particles at equivalent energies. For example, this analysis focuses partially on d + Au collisions. RHIC has also accelerated Cu beams into Au beams and there are plans in the works for upgrading the accelerator to allow p+Au collisions in the near future. RHIC is also the only facility in the world capable of accelerating and colliding polarized beams of protons, facilitating the study of the proton spin.

4.1. Tandem Van de Graaff

The journey of a gold nucleus begins in the Tandem Van de Graaff facility. Gold atoms are thermally ejected through resistive heating and passed by a cesium grid. The low electronegativity of cesium causes it to donate electrons to the gold, creating negative gold ions. A selector is used to isolate Au^- which is then accelerated via electrostatic attraction towards the first Van de Graaff generator. Stripping foils at the center of the generator removes electrons from the Au ion, converting it to a positive ion. The positive charge on the Van de Graaff generator repels the positive ion, accelerating it further. This process is repeated with a second generator, further ionizing and accelerating the ion, bringing the

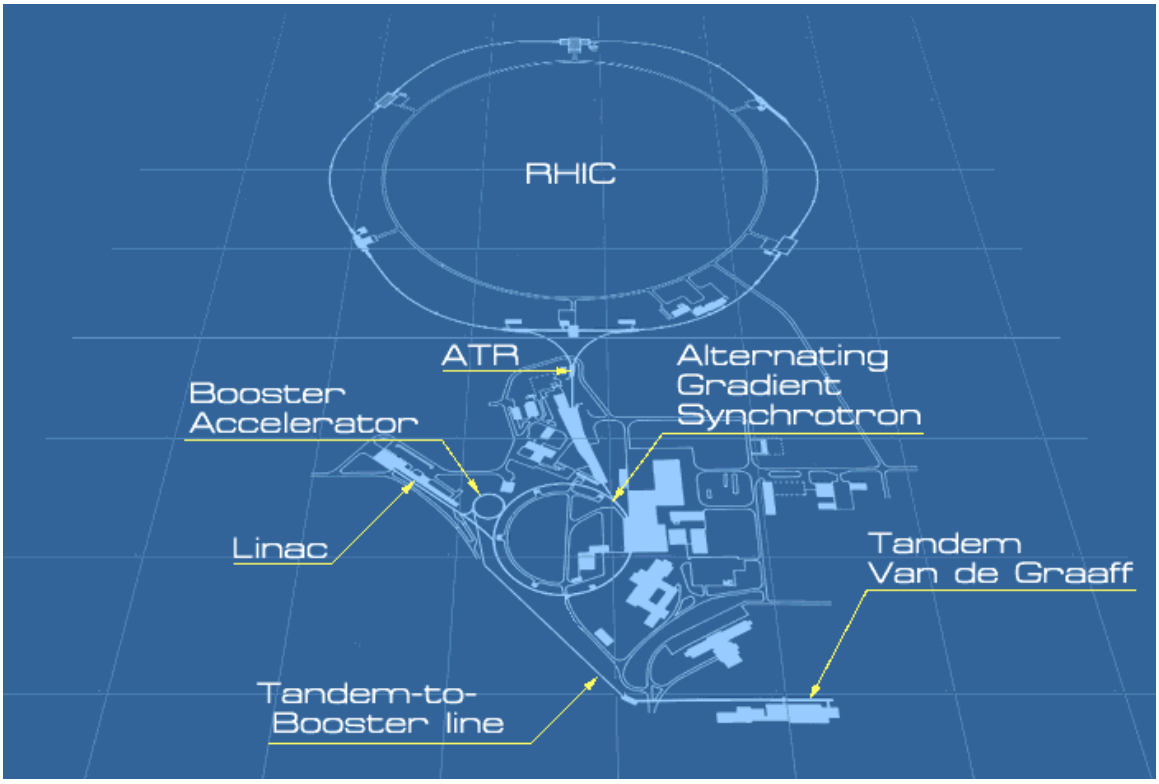

FIGURE 4.1. RHIC and its supporting infrastructure [**12**].

beam to 1 MeV per nucleon [**110**,**111**]. The beam is passed through an additional stripper and the Au^{32+} ions are directed down the Tandem-to-Booster line.

After Run 12 in 2012, the RHIC complex began using the **E**lectron **B**eam **I**on **S**ource (EBIS) as the preinjection source instead of the Tandems. The EBIS uses multiple electron beams to strip away electrons from nuclei through kinetic scattering. The ions are then ejected from the trap and further accelerated by a short linac to 2 *A*MeV before entering the booster ring [**112**]. Since this process does not have the electronegativity constraints of the Tandem system, the EBIS is capable of supplying ions from Helium through Uranium to RHIC experiments.

4.2. BNL Linear Accelerator

Protons begin their journey at the BNL Linear Accelerator (Linac), just west of the AGS. Operating since 1971, the Linac is 459 feet long and consists of nine accelerating RF

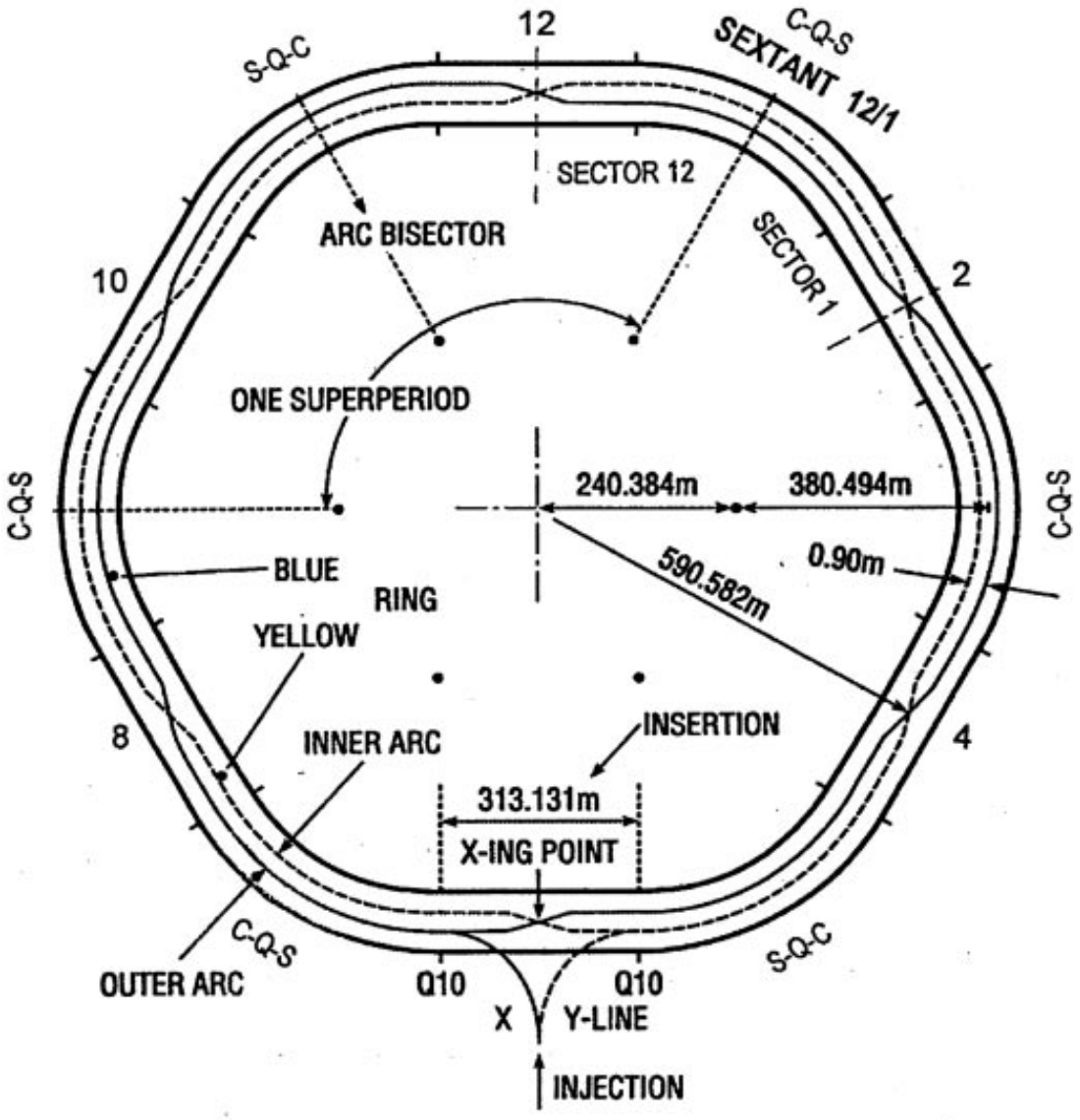

FIGURE 4.2. Layout of the two RHIC rings. The separation of the rings is not to scale. The counter-clockwise-circulating yellow ring is shown as a dashed line and the clockwise-circulating blue ring is solid. The six interaction regions are at 12, 2, 4, 6, 8, and 10 o'clock. [**13**]

cavities [**113**]. Protons exit the Linac with an energy of 200 MeV and are injected directly into the AGS.

4.3. Alternating Gradient Synchrotron

After traveling down the Tandem-to-Booster line, ions from the Tandems get an additional kick in the Booster ring, reaching 72 MeV per nucleon, before being transfered

to the AGS. Between the Booster and the AGS, the ions pass through another stripper and the Au^{77+} ions are directed into the AGS. Two hundred and fifty meters in diameter, the AGS is a powerful accelerator in its own right. The strong focusing established by the alternating magnetic gradients enable the AGS to handle very high intensity proton and ion beams. Gold ions are boosted to 10.8 *A*GeV by the synchroton before departing via the **A**GS-**t**o-**R**HIC (ATR) transfer line where the final two electrons are removed, leaving us with bare Au^{79+} nuclei. Proton beams are accelerated to 33 GeV. When not supplying beam to RHIC, the AGS still acts as a beam source for fixed-target experiments, including NASA radiation testing facilities.

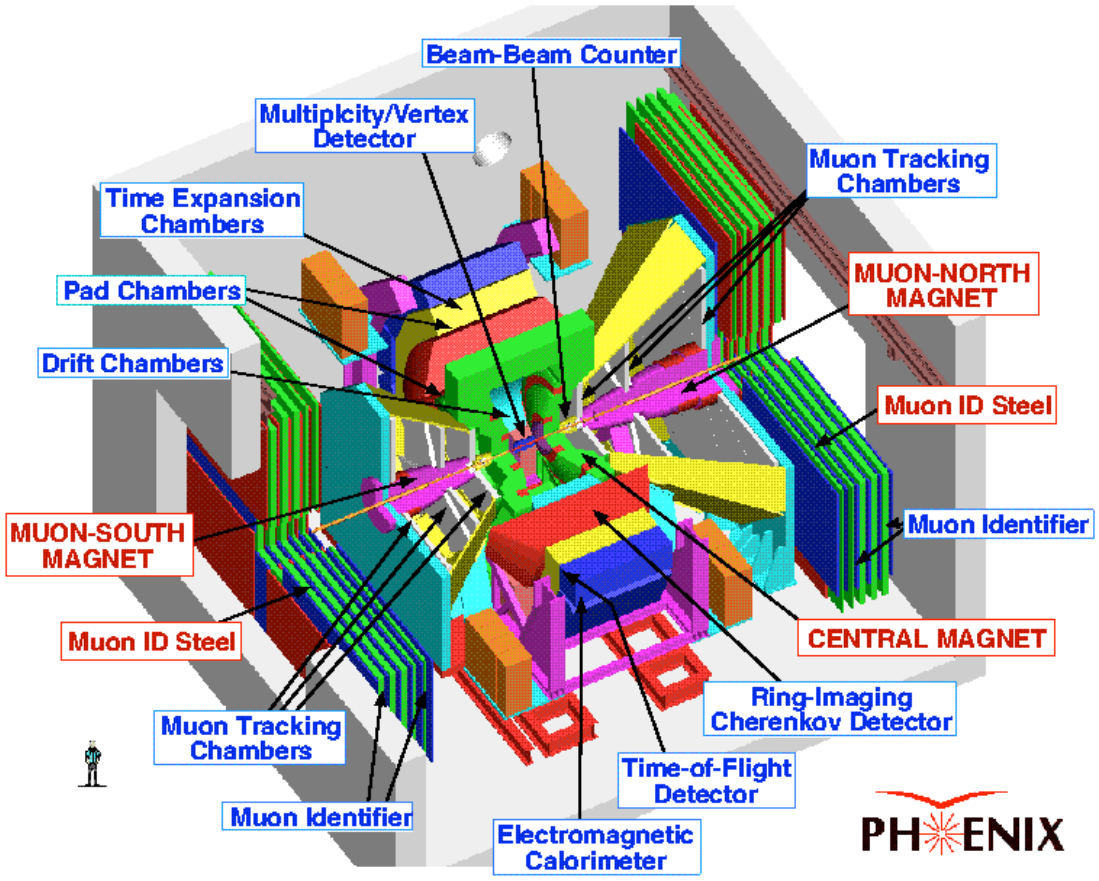

FIGURE 4.3. The PHENIX detector is a general purpose detector with multiple subsystems [**14**]. It currently operates at the eight o'clock position on RHIC.

4.4. RHIC

Once the beam reaches RHIC, it is diverted to either the blue (clockwise) or yellow (counter-clockwise) synchrotron (see Fig. 4.2). Each beam from AGS fills a single bucket, or particle bunch, in one of the synchrotrons. There are 360 possible buckets in total, determined by the 28 MHz acceleration cavity [**114**]. Typically, a number of continuous buckets are left unfilled to act as an abort gap during which the dump magnets can safely turn on without spraying stray beam across the equipment which may cause magnet quenches. Current operating procedures fill around 100 bunches in each ring.

Once both the blue and yellow rings are filled to desired capacity, the synchrotrons accelerate the buckets of ions to the desired energy (100 AGeV for ions or 255 GeV for protons). The beams are focused and aligned to produce collisions at the desired Interaction Regions (IRs). RHIC was designed with six IRs situated at two, four, six, eight, ten, and twelve o'clock. RHIC has two main, general-purpose detectors, STAR and PHENIX, and had two smaller experiments, BRAHMS and PHOBOS. STAR is located at the six o'clock point and PHENIX (**P**ioneering **H**igh **E**nergy **N**uclear **I**nteraction e**X**periment) is at the eight o'clock IR (see Fig. 4.3). BRAHMS (**B**road **Ra**nge **H**adron **M**agnetic **S**pectrometers Experiment at RHIC), shown in Fig. 4.4, was located at the two o'clock position and was designed to measure the momentum distribution of hadrons over a broad range of rapidity and momentum. Located at ten o'clock, PHOBOS was tailored to measure the multiplicity of charged hadrons across a very wide rapidity range (see Fig. 4.5).

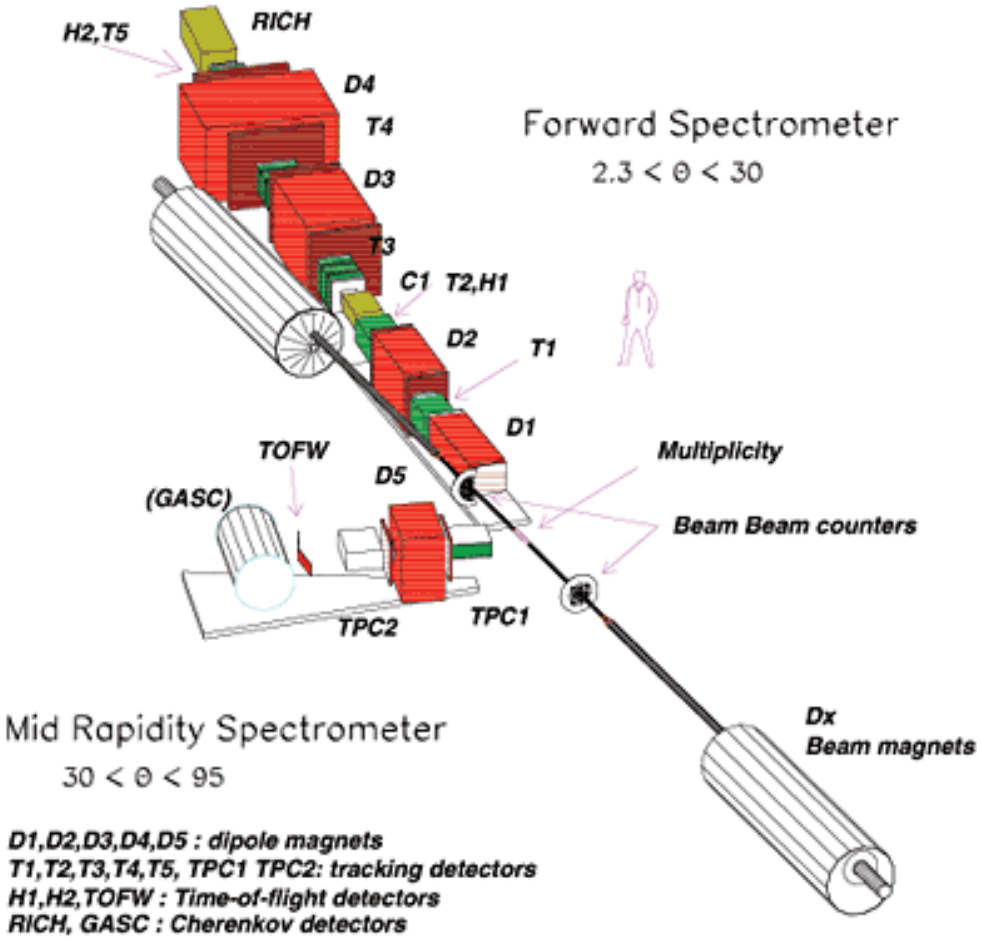

FIGURE 4.4. The BRAHMS detector [**15**]. Located at the two o'clock IR on RHIC.

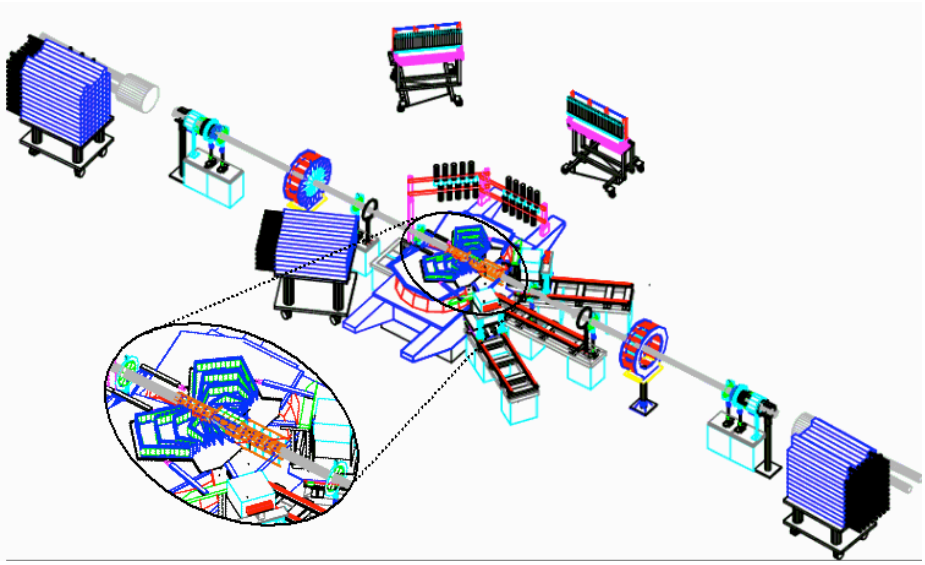

FIGURE 4.5. The PHOBOS detector [**16**]. Located at the ten o'clock IR on RHIC.

CHAPTER 5

The Solenoidal Tracker at RHIC

The **S**olenoidal **T**racker **a**t **R**HIC (STAR) is a multi-purpose particle detector with full azimuthal particle tracking and identification in a wide rapidity range ($|\eta < 1|$). STAR is comprised of a myriad of subsystems, each playing an important role in giving STAR its versatile capabilities [**115**]. However, here we will focus on just the detectors which played a direct role in these analyses.

5.1. Beam-Beam Counter

The **B**eam-**B**eam **C**ounter (BBC) is comprised of two collections of four scintillator annuli centered around the RHIC beam pipe, each located 374 cm from the interaction region [**17**, **116**]. Each detector is comprised of 36 scintillator tiles: 18 smaller ones forming the two inner annuli and 18 larger ones forming the two outer annuli. The inner annuli together cover a pseudorapidity range of $3.3 < |\eta| < 5.0$ while the outer cover $2.1 < |\eta| < 3.6$

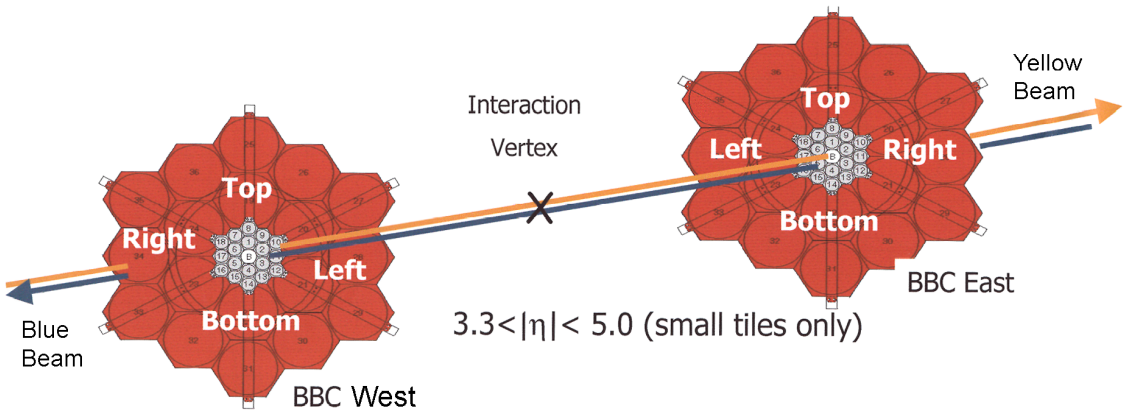

FIGURE 5.1. The STAR BBC is divided into two identical detectors on the east and west sides of the interaction region. The each BBC detector contains two inner annuli of smaller scintillators and two outer annuli of larger scintillators [**17**].

[**117**]. Due to the hexagonal geometry of the individual detectors, there is a slight overlap between the inner and outer rings, as shown in Fig. 5.1.

The BBC is designed to detect high-η particles produced in $p+p$ collisions. Measurement of the relative position of these particles is useful in proton polarization studies done at STAR since RHIC is the only accelerator capable of polarizing its proton beams. The BBC is not used in heavy-ion collisions due to the high multiplicity in such events.

The BBC also acts as the main detector in the $p+p$ minimum bias trigger. The minimum bias trigger requires at least one hit within the eighteen detectors comprising the inner two annuli coincidentally in both the east and west detectors. This signals come from prompt high-η particles produced in most $p+p$ collisions. This trigger corresponds to a $p+p$ cross section of $\sim 26.1 \pm 0.2$ (stat.) ± 1.8 (syst.) mb, $87 \pm 8\%$ of the total $p+p$ inelastic cross section excluding singly diffractive events [**116**, **118**]. The systematic uncertainty in the $p+p$ BBC cross section is one of the dominant sources of uncertainty in the Υ cross section measurement. This highly efficient trigger works in conjunction with the barrel calorimeter (see Sec. 5.5) to create our Υ trigger, as discussed in Sec. 6.3.

5.2. Zero Degree Calorimeter

All four of the original RHIC experiments were equipped with the same set of **Z**ero **D**egree **C**alorimeters (ZDCs). The ZDCs are directly in line with the STAR beam pipe, 18 meters from the interaction point. In heavy-ion collisions, spectator neutrons which survive the collision continue directly down the beam pipe. Since neutrons are uncharged, they are undeflected by the bending magnets and travel directly forward (see Fig. 5.2). The greater the overlap of the ions, the smaller the number of neutrons which do not participate in the collision, and the smaller the signal in the ZDC. This makes the ZDC sensitive to the overlap, or centrality, of the collisions.

The ZDCs are comprised of layers of tungsten-alloy absorber and plastic scintillator. Signals are read out from the scintillator layers via fiber optics and sent to PMTs. The ZDCs are 5.1 interaction-lengths long, making them highly efficient at detecting hadrons. Hence, they have in the past formed the basis of STAR's minimum bias trigger for Au + Au

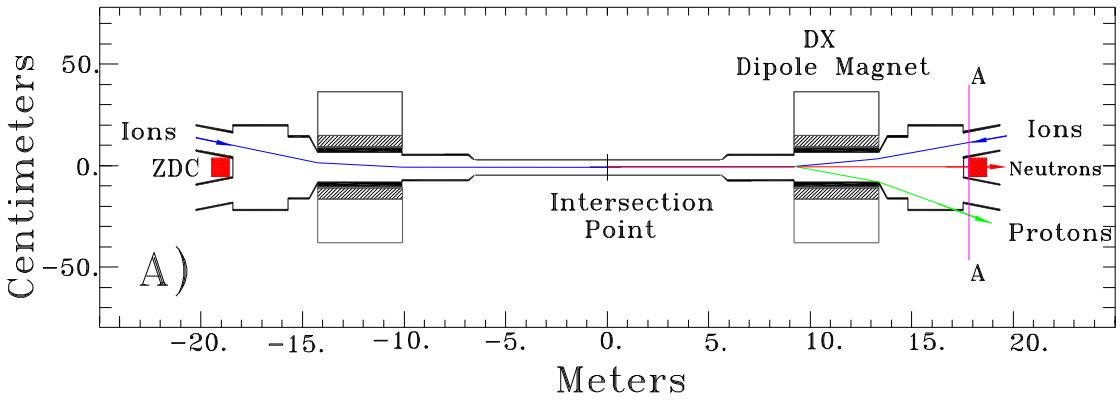

FIGURE 5.2. A bird's-eye view of the RHIC beam pipes at STAR and the ZDC. The blue curve shows the path of incoming ions. The charged protons released in the collision are over-deflected as shown by the green curve. The neutrons are undeflected by the dipole magnet and travel directly forward to the ZDC (shown in red) [**18**].

collisions. However, the ZDC has an energy resolution of 18%, leading to a sizable uncertainty in the number of neutrons detected [**18**]. This has lead the individual experiments to develop additional detectors and techniques for measuring centrality more precisely.

5.3. Vertex Position Detector

Like the BBC, the **V**ertex **P**osition **D**etector (VPD) is comprised of an east and west detector. Each detector is a collection of 19 Pb+scintillator+photomultiplier tubes arranged in an annulus around the beam pipe [**119**]. Each half of the VPD is located 5.6 meters from the interaction region. The time difference between the signals in the east and west detectors is used to determine the vertex location. In $p+p$ collisions, the VPD has a timing resolution of ∼140 ps corresponding to a spatial resolution of ∼4 cm. In $d+$ Au and Au + Au collisions, the timing resolutions are 54 ps and 23 ps, respectively, and the spatial resolutions are 1.6 cm and 7 mm. The VPD can only measure the z-coordinate of the vertex (along the beam pipe). The VPD is unable to determine the x- or y-coordinates. In Au + Au collisions, the minimum-bias trigger requires a coincident signal in both the east and west detectors.

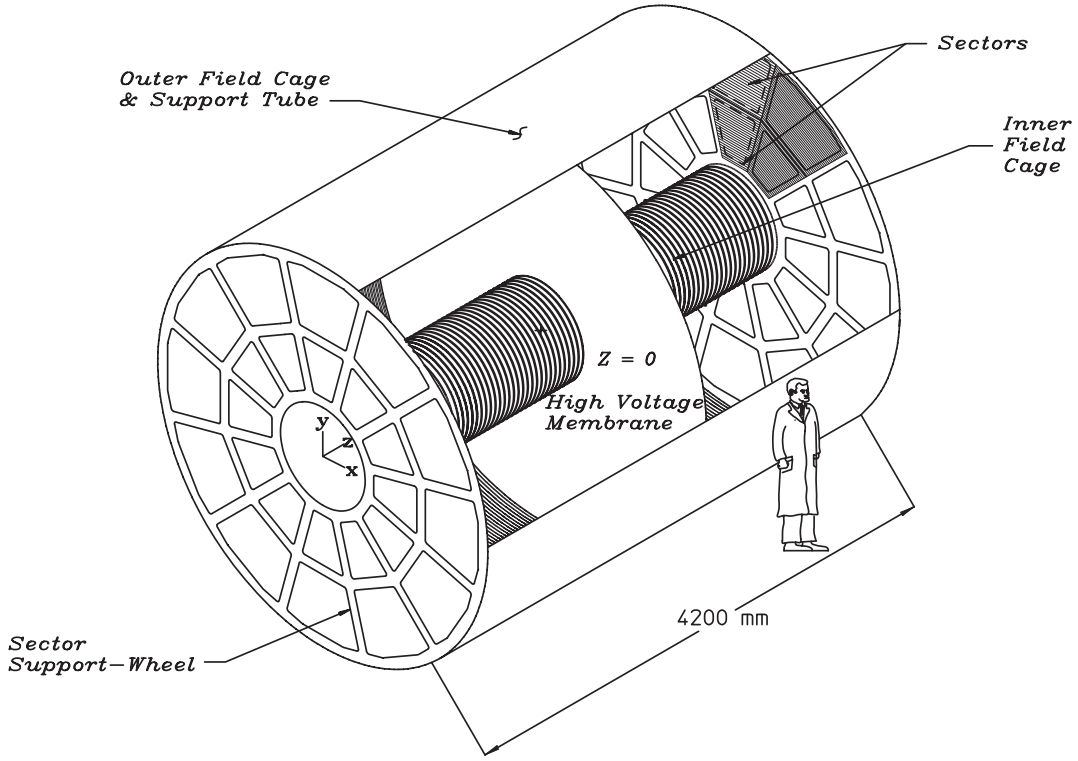

FIGURE 5.3. The STAR Time Projection Chamber. [**19**]

5.4. Time Projection Chamber

At the heart of STAR lies the **T**ime **P**rojection **C**hamber (TPC), which allows for tracking and identification of charged particles via ionization energy loss [**19**]. Shown in Fig. 5.3, the TPC is a gas-based detector with electronic readouts on each end. It sits inside a large, conventional solenoid which produces a 0.5 T magnetic field oriented along the beam axis. The trajectories of charged particles are deflected by this field, allowing for determination of their momenta.

The interior of the TPC is filled with P10 gas (10% methane, 90% argon) held at slightly above atmospheric pressure to prevent oxygen contamination. When a charged particle passes through the gas, it ionizes the argon and a strong electric field of ≈135 V/cm causes the ionized electrons to drift to the **f**ront-**e**nd **e**lectronic readouts (FEEs) at either end. The methane acts as a collisional buffer to maintain a constant drift velocity for the electrons.

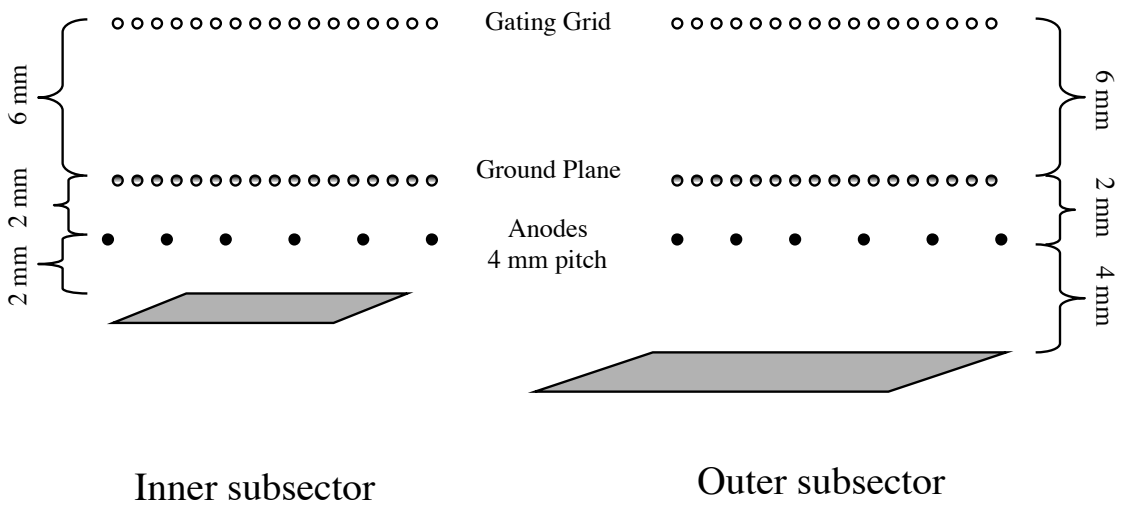

FIGURE 5.4. The TPC wiring grid. The gating grid controls whether drifting electrons make it to the anodes where the image charge can be read out by the FEEs while the ground plane and anodes provide signal amplification through electron avalanches [**20**].

In the readout sections of the TPC, there is a grid of wires just before the FEEs in the direction of electron drift (see Fig. 5.4) [**20**]. The gating grid control control access to the FEEs. When open, all of the wires in the gating grid are biased to the same voltage (~ 110 V), in-line with the potential established by the central membrane and the ground-plane at the end-caps. Hence, the gating grid is essentially "invisible" to the drifting electrons. When closed, alternating wires of the gating grid are biased above or below their standard potential by 75 V, causing electrons and ions to be attracted to the grid and preventing access to the FEEs.

The anode wires are biased to a high voltage ($\sim 1000 - 1390$ V), creating an extremely strong electric field due to the proximity to the ground plane. When electrons are accelerated by these intense fields, they ionize neutral atoms via collisions. These newly-freed electrons are themselves then accelerated by the same field, ionizing more atoms, and leading to a chain reaction known as an avalanche. Being heavy, the ions take longer to dissipate than the electrons, leading to a net positive charge which induces an image charge on the readout pads of the electronics.

Particle tracks are then reconstructed at a software level from individual hits in the TPC. Reconstruction is achieved with a Kalman filter to determine the parameters of a

track [**22**]. All track segments are treated as helices with each additional segment having a slightly smaller radius of curvature to account for energy loss. Reconstruction begins at the outer edges of the TPC where the hit density is lowest. The finder combines nearby hits to form track candidates (seeds). These seeds are then fit to a helix and the parameters are used to predict where the next hit should be, taking into account modification of the curvature of the helix due to energy loss. All tracks are treated as $\pi^{\pm}$ for energy loss assumptions. In this fashion, the track is projected inward towards the center of the TPC where hit-density skyrockets and individual track segments can be a priori ambiguous. Each time a hit is added to a track, the track is refit and the updated parameters are used to predict the next location of the next track point.

The STAR framework distinguishes between three types of tracks: global, primary, and secondary [**22**]. Global tracks are all of the tracks found by the fitter before we calculate the event vertex. Global tracks are then projected back to the beamline and vertices are found by searching for clusters of tracks along the beam axis. For more information on vertex-finding, see Ref. [**120**]. Once the main event vertex is found, all tracks pointing to it are refit using the vertex as another hit. These new tracks are labeled primary tracks. Furthermore, pairs of global tracks that begin mid-TPC are associated by a V0 finder and come from in-flight decays of neutral particles (e.g. $K^0 \rightarrow \pi^+\pi^-$).

Once a track is reconstructed, we can extract many different properties of the particle. Based on the curvature of the track and knowledge of the magnetic field, we can measure the transverse momentum (p_T). However, as the momentum increases, the track approaches a straight line. This makes the momentum determination less precise as momentum increases (see Fig. 5.6).

We can also calculate ionization energy loss by integrating the electron signal amplitude of each hit which is proportional to the energy lost in that track segment. By taking into account track length, particle identification can be achieved via characteristic energy loss (dE/dx) as a function of momentum as predicted by the Bichsel equations [**21**]. An example distribution is shown in Fig. 5.5. However, at the track momenta used in this analysis ($p >\sim 3.0$ GeV/c), the electron band sits alongside the hadron band. This proximity complicates electron identification due to the relatively high number of hadrons compared

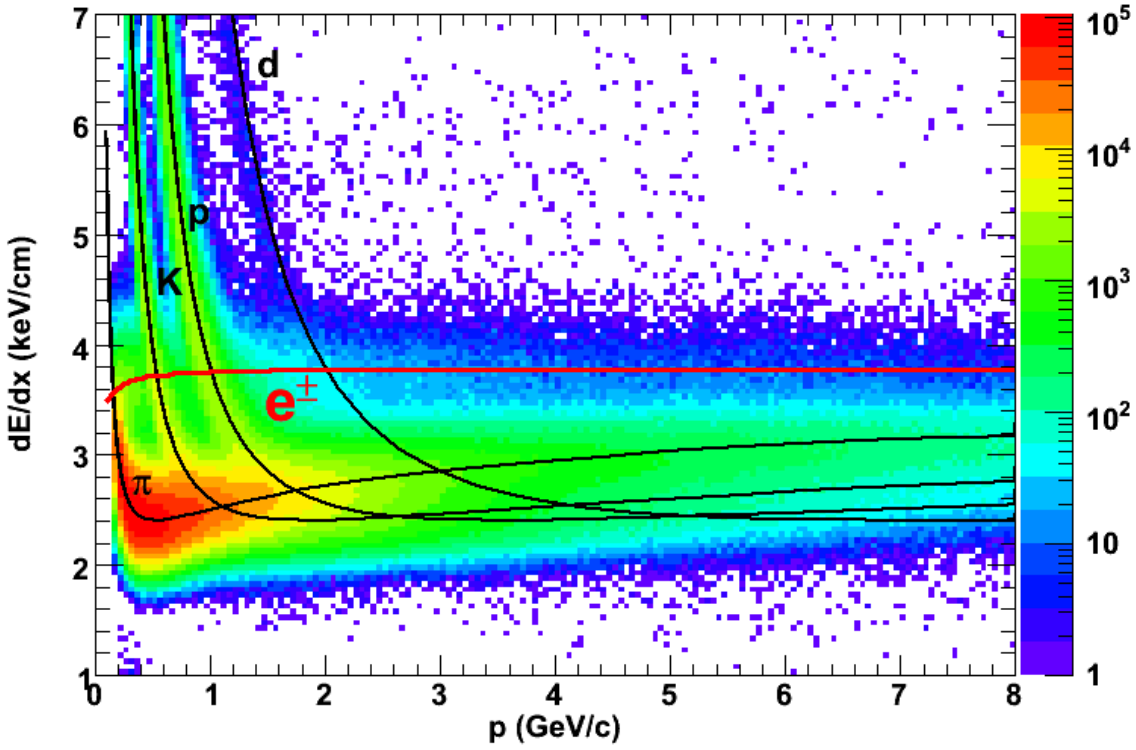

FIGURE 5.5. Characteristic ionization energy loss used to identify charged particles. The curves are predictions from the Bichsel equations [**21**].

to electrons. While this means discrimination based solely on dE/dx will be impure, it can still be used to reject obvious false electrons.

5.5. Barrel Electromagnetic Calorimeter

Outside the TPC sits the **B**arrel **E**lectro**m**agnetic **C**alorimeter (BEMC). The BEMC is a lead and plastic scintillator calorimeter segmented into 4,800 towers with full azimuthal coverage and wide rapidity coverage ($|\eta| < 1$) [**23**]. The towers are 0.05 units wide in both η and ϕ and are skewed to point back towards the interaction region at $z = 0$. Calorimeter towers contain 41 alternating layers of plastic scintillator and lead, as seen in Fig. 5.8. The total depth of a tower at mid-rapidity is 20 radiation lengths, allowing for precise determination of the energy of photons and electrons. Scintillator light is read out via fiber optics and transported to photomultiplier tubes (PMTs) outside the solenoidal magnet where it can be digitized and read out.

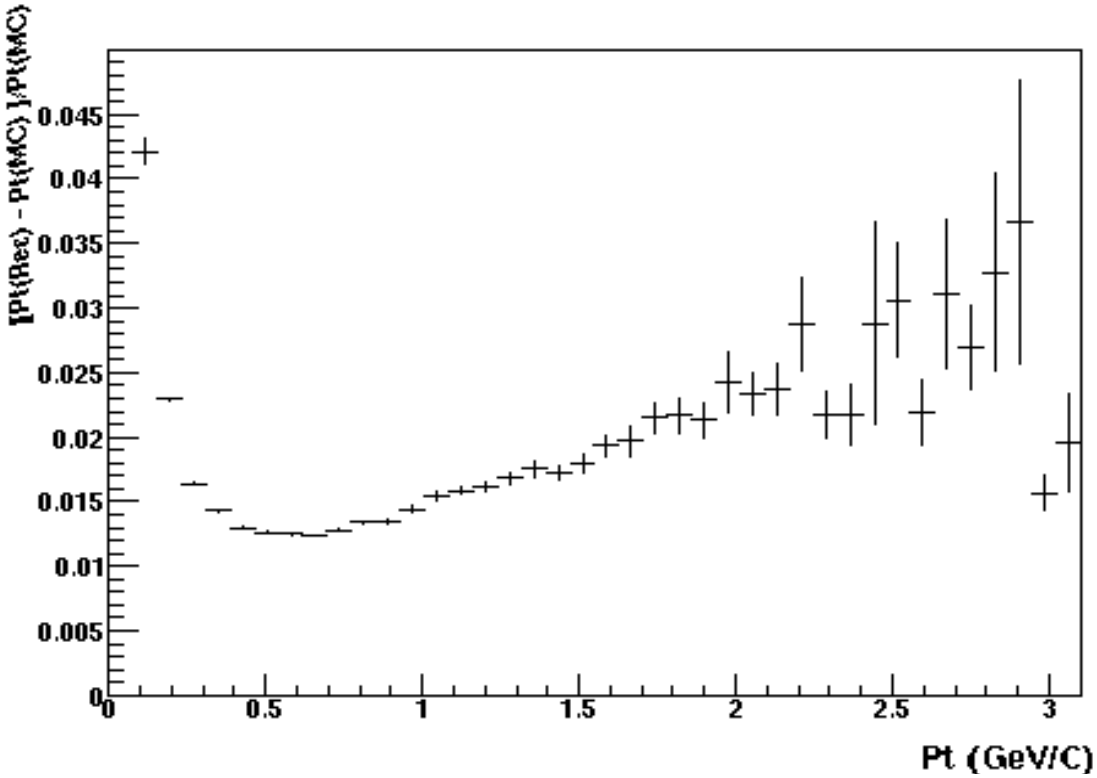

FIGURE 5.6. TPC momentum resolution as a function of momentum as ascertained by Monte-Carlo simulations. [**22**]

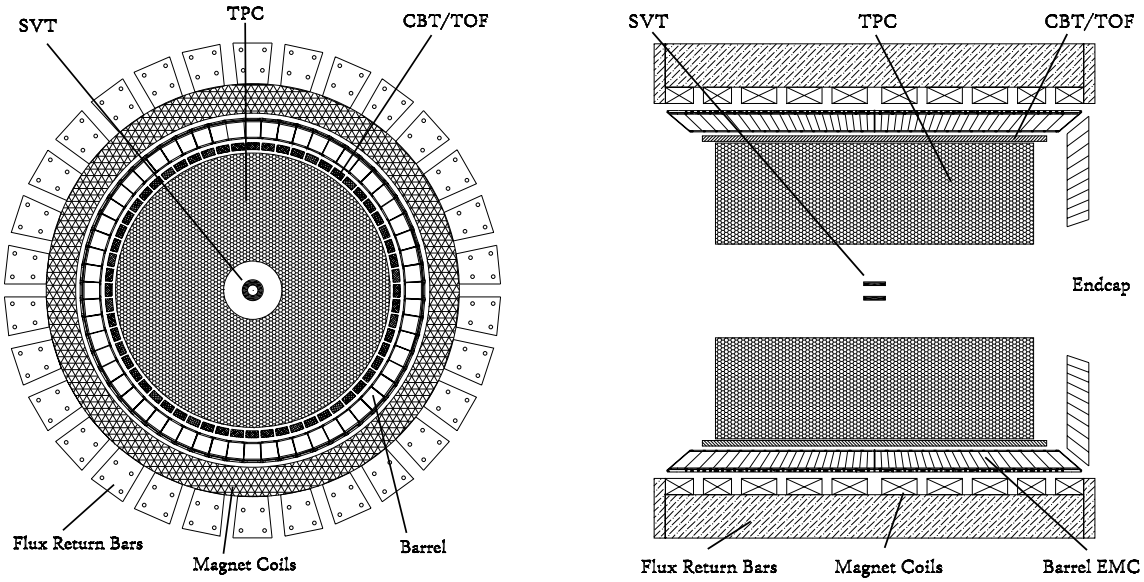

FIGURE 5.7. The STAR BEMC surrounds the TPC [**23**]. The Silicon Vertex Tracker (SVT) was removed in 2007 and will be replaced as part of an enhanced silicon vertex detector starting in 2014.

The BEMC has an energy resolution σ_E/E of $\sim 14\%/\sqrt{E}$ plus a constant term of 1.5% which needs to be added in quadrature [**23**]. For a 5 GeV electron, this gives us a resolution of ∼6.5%. In $A+A$ collisions, the high multiplicity of particles creates a background signal in the BEMC, leading to a deterioration of resolution of the measured energy. However, studies show that at an energy of 3 GeV, this effect only increases the resolution from 9% to 10% [**23**]. As this effect decreases with increasing energy, it is negligible for electrons coming from Υ decays ($>\sim$ 5 GeV).

The BEMC is multipurpose in these analyses: its speed and coverage make it a useful trigger for identifying candidate Υ events and it can be used in conjunction with the TPC to identify high-momentum electrons.

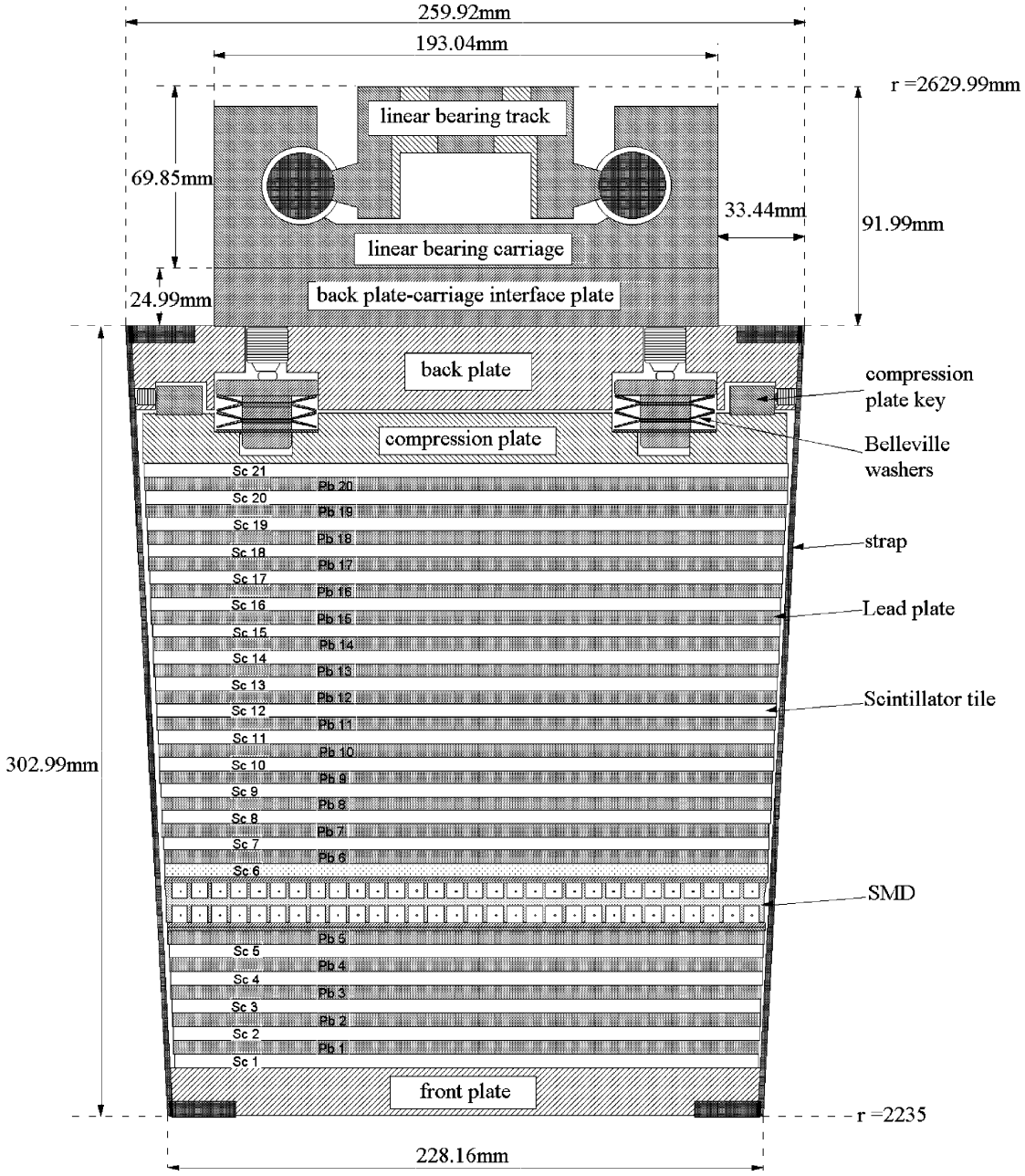

FIGURE 5.8. A single tower of the STAR BEMC. [**23**]

CHAPTER 6

Analysis Methods

This chapter describes in depth the methods used in these analyses. Specifically, we'll cover event triggering, determination of sampeled luminosity, electron identification via dE/dx and E/p, and extraction of the Υ yield from the invariant-mass spectrum.

6.1. Triggering

Υ production is a fairly rare process, occurring approximately once every billion $p+p$ collisions at $\sqrt{s_{NN}} = 200$ GeV. In order to have any meaningful statistics, our trigger needs to be highly efficient. However, until the installation of the DAQ1000 in 2010, data-acquisition was limited to 100 events per second shared amongst all triggers. To record enough candidate Υ events without using too much of the DAQ bandwidth, a dedicated Υ trigger was designed. The Υ trigger had two stages: a level-0 (L0) hardware stage and a level-2 (L2) software stage. The 2008 $d+\text{Au}$ and the 2009 $p+p$ datasets were captured using this two-stage Υ trigger. However, after the acquisition bandwidth was increased by the DAQ1000 upgrade in 2010, we no longer needed the L2 trigger since the L0 trigger could be recorded without any prescaled reduction. Hence, we could sample the full luminosity without the complications imposed by the L2 trigger logic.

6.1.1. L0 Trigger. L0 triggers are used to open the gating grid of the TPC for event acquisition, so they must be fast and simple. All L0 triggers must fire in under 700 ns [**23**]. Since they open the gating grid, L0 triggers are the only triggers which can allow the acquisition of an event; all other triggers may only veto events.

In all three datasets, the L0 trigger was based on the presence of a high amount of energy in at least one BEMC tower, known as a high tower (HT) trigger. At every bunch crossing, the BEMC towers are read out via their PMTs and the signal is digitized. A unique pre-measured background level, or pedestal, is then subtracted from each tower.

For triggering purposes, the data from each tower is coarsened to 6-bit value and sent to the L0 Data Storage and Manipulation hardware (DSM). This value is known as the DSM-ADC. The L0 trigger is fired by a DSM-ADC signal greater than 18 which corresponds to an $E_T >\sim 4.2$ GeV [**121**–**123**]. Due to the high mass of the Υ, the HT trigger detects most Υ events within STAR (see Fig. 6.1).

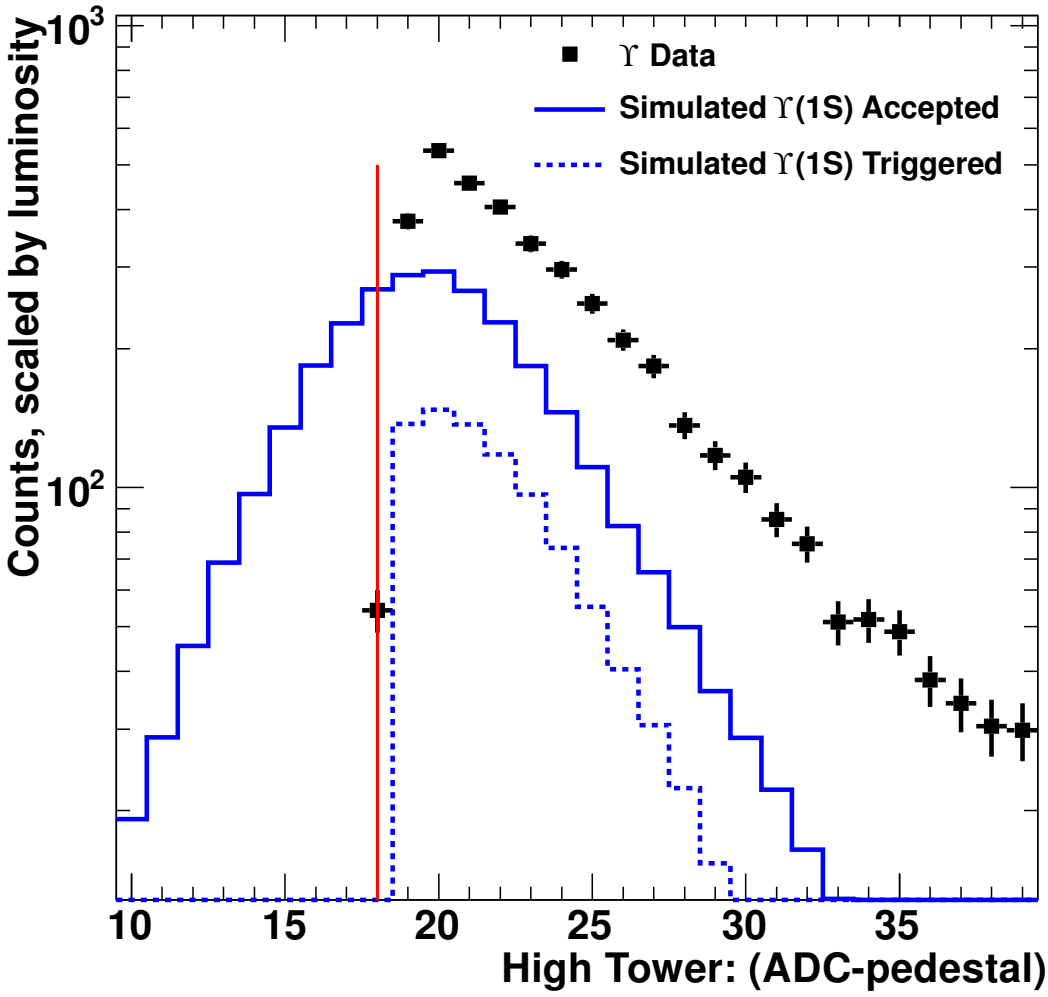

FIGURE 6.1. ADC Distribution for $p+p$ 2009 Υ triggered data (black), showing the L0 threshold. The expected distribution for the signal obtained from embedding is shown in blue for all simulated Υ (solid line) and for those that satisfy all the trigger requirements.

Furthermore, the HT triggers require an additional signal in the highly forward detectors. In $p+p$, this is the VPD; in $d+\mathrm{Au}$ and $\mathrm{Au}+\mathrm{Au}$, the ZDC.

In the $p+p$ and $d+\mathrm{Au}$ runs, events which fired the L0 HT trigger were passed on to the L2 Υ trigger. Furthermore, a fraction of the L0 triggered events are recorded based on prescaling regardless of the result of the L2 trigger. In the $\mathrm{Au}+\mathrm{Au}$ run, all events which satisfied the L0 HT trigger requirements were recorded.

6.1.2. L2 Trigger. As implied by its name, the L2 Υ trigger was designed to record candidate Υ events. The L2 trigger is a software trigger based solely on information from the BEMC. While all events which fire the L0 HT trigger open the TPC gating grid so the FEEs can acquire the data, the L2 trigger determines whether the data is written to disk from the FEEs.

The L2 trigger begins its analysis with the high tower from the L0 trigger. It creates a cluster of energy in the BEMC by combining the two most energetic towers in the eight neighbors surrounding the L0 high tower. Using calibrations from the beginning of the Run and pedestals taken periodically, the trigger calculates the total energy of the cluster, which mush surpass the L0 cluster energy threshold in Table 6.1.

The trigger then finds a lower-energy seed tower (L2 tower) determined by either DSM-ADC or energy based on the year as seen in Tab. 6.1. It then builds a cluster around this tower just like we did with the L0 seed. Assuming the energies measured in each cluster are deposited by electrons, we reconstruct the invariant mass of the parent particle. If it falls around the Υ mass, as seen in Tab. 6.1, we record the event. Example distributions of L2 parameters from simulation as well as actual data from the 2009 $p+p$ run can be seen in Fig. 6.2.

This trigger is highly efficient at finding Υ whose daughters are within our geometrical acceptance. However, since the trigger is based on clusters of energy in the BEMC, it is also highly efficient at collecting dijet events.

6.2. Harvesting Υ Candidates

The framework for harvesting data from STAR is based around modular programs which stage, calibrate, format, and process data known as *makers*. By stringing together

Parameter	$d+$Au Value	$p+p$ Value
L0 DSM-ADC High Tower Threshold	18	18
L2 DSM-ADC High Tower Threshold	5	n/a
Number of consecutive firings to label a Hot Tower	10	20
Hot tower energy threshold	2.5 GeV	10 DSM-ADC
Use Vertex	0	0
Max No. of Hot Towers	25	25
L0 Tower Seed Threshold	n/a	4.0 GeV
L2 Tower Seed Threshold	n/a	1.2 GeV
L0 Cluster Energy	4.5 GeV	4.5 GeV
L2 Cluster Energy	3 GeV	3 GeV
Min. Inv. Mass	6.5 GeV/c^2	5.0 GeV/c^2
Max. Inv. Mass	25.0 GeV/c^2	20.0 GeV/c^2
Max. $\cos(\theta_{12})$	0.0	0.0

TABLE 6.1. Parameters used in the L2 Υ trigger for the 2008 $d+$Au and 2009 $p+p$ datasets: ADC threshold value of the L0 triggering tower (must be met to be considered by the L2 algorithm), ADC threshold value of the partner tower, maximum number of times a tower could fire the tigger in a row before being considered a Hot Tower, signal threshold to be considered a Hot Tower, a flag to use the BBC vertex, maximum number of hot towers to mask, minimum energy of the seed towers, minimum cluster energy around the L0 and L2 towers, minimum and maximum invariant mass from BEMC energy, and minimum opening angle.

a chain of makers, we can calibrate and analyze information from the detectors critical to our analysis without wasting memory and CPU time on detectors that will go unused for our purposes. We used two different makers to analyze and harvest the data stored at the RHIC Computing Facility (RCF). One maker was used for the $p+p$ and $d+$Au datasets in which we needed to recalculate and be mindful of the multiple trigger conditions which apply to both tracks. The other maker was used for the Au + Au analysis where only the L0 trigger was in play and the only condition imposed by the trigger was a single high tower in the BEMC.

First, we discuss the maker used to harvest the Au + Au dataset. In order to avoid random benefit (i.e. counting an Υ candidate which was in a triggered event but did not itself fire the trigger, thereby incorrectly inflating the yield of candidates), we must ensure that our Υ candidate pair satisfied all of the trigger requirements. We search for any tower in the barrel which has a DSM-ADC greater than the L0 threshold (18 DSM-ADC). Next, we search for tracks which originate at our collision vertex and point to a high tower. If

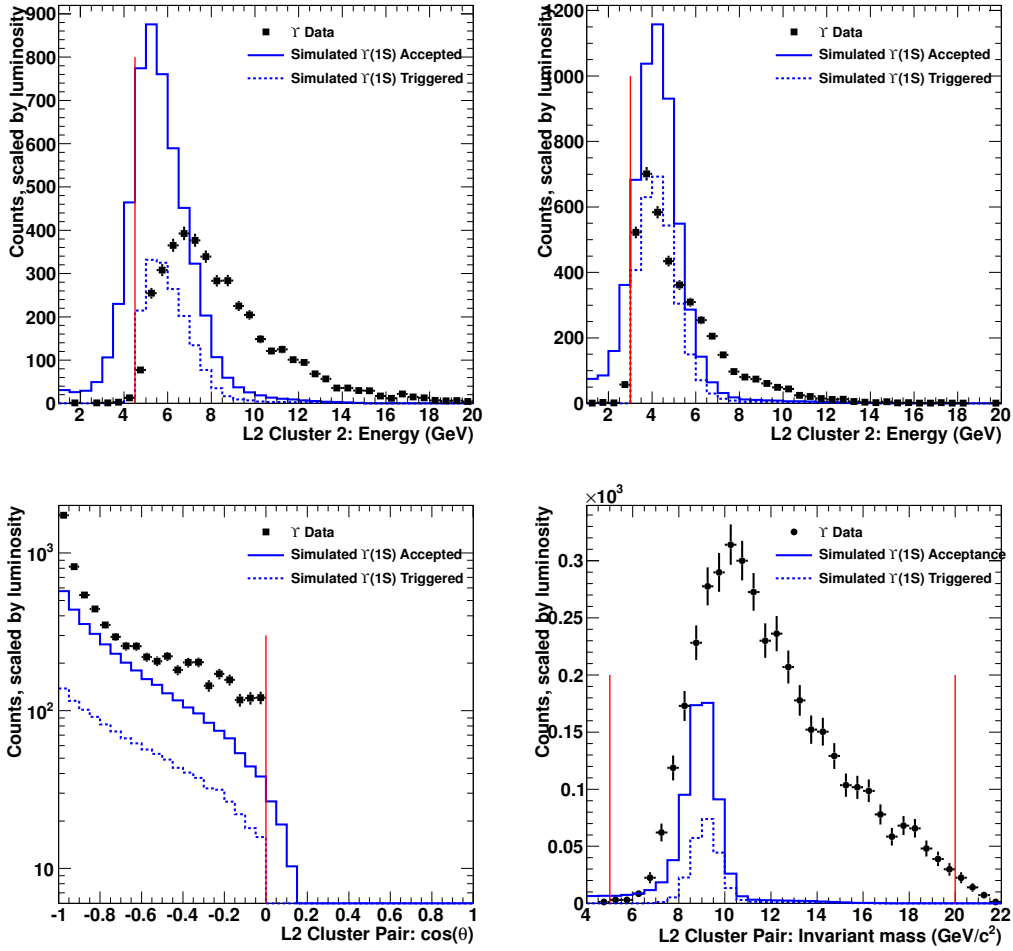

FIGURE 6.2. L2 Trigger distributions: (Top, left) E_{cluster} for daughter above the high L2 threshold, E_1; (Top, right) E_{cluster} for daughter above the low L2 threshold, E_2; (Bottom, left) L2 cosine of the opening angle, $\cos(\theta_{L2})$; (Bottom, right) L2 invariant mass. All cuts shown are from the 2009 values.

these are high quality tracks (many fit points, no bad track flags, decent DCA) and they look somewhat like an electron (via very loose cuts on E/p and ionization energy loss to reject most of the pions), we store them as candidates for the first daughter from an ϒ decay. In the context of the makers and analysis, the first daughter refers to the either the track that fired the trigger (in $\text{Au}+\text{Au}$) or the track which deposited more energy in the calorimeter (in $p+p$ and $d+\text{Au}$). Once we have our collection of tracks which could have fired the trigger, we combine each of them with other tracks which pass similarly loose cuts on E/p and energy loss and also originate from the same vertex to calculate the invariant

mass of a parent particle which could have decayed into that pair. If the mass is near the Υ mass range (5-20 GeV/c^2), we then extrapolate the second track out to the BEMC and try to construct a cluster and match the track to it. These two tracks are logged in an n-tuple along with multiple identifying parameters for later analysis and refinement. We are purposefully loose with our identification cuts in this process; it is easier to exclude tracks, candidates, or events later in the analysis than it is to come back and recollect additional physics thrown out previously.

The maker used for $p+p$ and $d+\mathrm{Au}$ follows similar logic but it constructed differently due to the conditions imposed by the L2 trigger. We again begin by imposing trigger conditions as in the $\mathrm{Au}+\mathrm{Au}$ maker. After finding the L0 seed, we form a cluster, find an L2 seed, and form another cluster as described in detail in Sec. 6.3. If these clusters and their geometry satisfy the conditions in Tab. 6.1, we proceed to the tracks in the TPC. We loop over all tracks and compare them to the triggering clusters in the BEMC. If a high-quality track looking somewhat like an electron points to a cluster, we associate the track-cluster pair. We then combine all associated tracks with each other and if they look like they came from a particle near the Υ mass and their associated tower clusters could have fired the L2 trigger, we record their properties in a tuple for later analysis.

6.3. Acceptance and Triggering Efficiency

In order to estimate geometrical acceptance and trigger efficiency, we employed Monte Carlo simulations. Using GEANT [**124**], we generate Υ with flat rapidity and transverse momentum (p_T) distributions which are reweighed later with a more realistic distribution. All Υ are forced to decay to electrons. The Υ ground state is simulated as well as the first two excited states (2S and 3S). All three Υ states are analyzed separately and the results are combined via weighting by relative production rates.

The daughter electrons are then propagated through a GEANT model of STAR and its subsystems. The electronic response of the detectors are then simulated. To simulate a real environment, we embed the simulated response into the raw data of a recorded event. This combined event is then run through the STAR reconstruction chain.

Since we simulated the embedded tracks, we know their properties, such as position and momentum. We search the reconstructed tracks for the embedded daughter tracks to compare their measured properties to their actual (thrown) values. Using this knowledge, not only can we determine the rate of track reconstruction (needed to tracking efficiency), but we can also estimate geometrical acceptance, triggering efficiency, momentum resolution, and pair-wise mass resolution. Acceptance is directly determined by counting the number of events in which both daughter electrons fall within the active region of the TPC and BEMC. By imposing the L0 and L2 triggering requirements to the embedded Υ events, we can directly measure the triggering efficiency. In Fig. 6.2, we show example distributions of L2 variables from Υ decays embedded in events from the 2009 $p+p$ run. Calculated triggering efficiencies for midrapidity Υ are shown in Tab. 6.2.

State	$p+p$	$d+\mathrm{Au}$	$\mathrm{Au}+\mathrm{Au}$ 0-60% centrality
1S	0.195	0.210	0.213
2S	0.214	0.262	0.235
3S	0.259	0.275	0.245

TABLE 6.2. Geometrical acceptance times triggering efficiency at midrapidity for all three datasets as esitmated through embedding procedures.

In order to correctly apply our measured triggering efficiencies, we must ensure that we only count Υ candidates which could have triggered the DAQ. For the 2009 $p+p$ and 2010 $\mathrm{Au}+\mathrm{Au}$ analyses, we had access to the class StTriggerSimuMaker which reads in calibration tables from the time of data collection and emulates the conditions seen by the trigger. In this way, we can identify the BEMC tower or towers which fired the Υ trigger. Any Υ candidate which could not have fired the trigger is discarded for these analyses.

Unfortunately, we could not use the StTriggerSimuMaker class to emulate the 2008 trigger. Instead, the conditions were manually imposed during our analysis. All of the calibrations for the L2 quarkonia trigger were stored from the run (see Ref. [**125**]). By reading in the calibrations at the beginning of the new run, we could fake the same triggering conditions to make sure we only take Υ candidates which fired the trigger. Also, some of the final values from the trigger, such as the energy in the clusters, were stored in the event information. By comparing the results of our faked trigger with the values stored in the

event information, we can ensure that our calculations are successful. Without reading in online calibrations, our faked trigger values fall near the recorded online values, but there is still a spread (see Fig. 6.3, left). Once we use the correct calibrations, the two results agree for the vast majority ($\sim 99.4\%$) of events (Fig. 6.3, right).

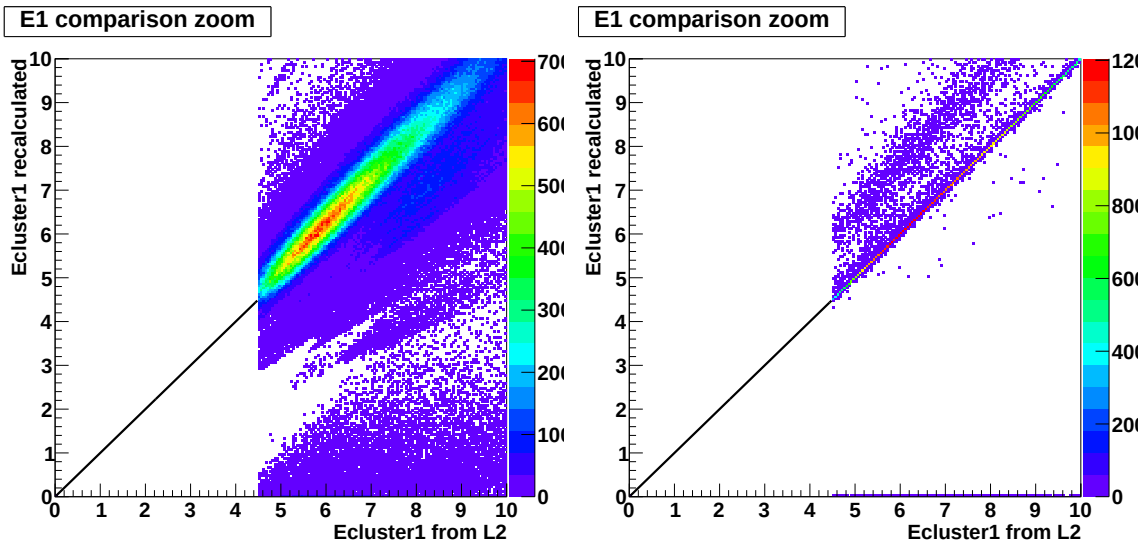

FIGURE 6.3. Illustration of the results of calibrating the 2008 L2 trigger correctly during analysis. The left plot shows the comparison between our reconstructed values when offline calibrations are used (y-axis) and what was recorded online. The right plot shows the reconstructed values when we used the online calibrations. The black line is a guide for the eye and has unity slope. Note the vastly reduced spread in the right, calibrated plot.

6.4. Run Selection and Luminosity

In order to ensure a clean measurement of the cross section, we need a good determination of the sampled luminosity. As a first pass, we reject any run labeled "bad" or "questionable" by the shift leader.

Both the L2 Υ trigger used in $p+p$ and $d+\mathrm{Au}$ and the L0 HT trigger used in $p+p$ are based on high amounts of energy seen in the BEMC. If a BEMC tower gets stuck high, it can cause the triggers to fire erroneously, leading to false positives. While these events should be removed by analyzing tracking from the TPC, we have enough "good" data that it is not worth trying to salvage bad runs.

These errors in the TPC will lead to increased triggering rates. However, changes in the luminosity of the beam over the lifetime of the store will also lead to variations in the triggering rate. To remove the effect of varying luminosity, we compare the triggering rate of our trigger to that of the minimum bias trigger in that system. We make a Gaussian fit to the distribution and reject any run with a MB-to-Υ trigger ratio more than 5-sigma away from the mean.

6.5. Electron Identification

The vast majority of particles produced in hadronic collisions are pions. In order to reconstruct Υ mesons from their decay products, we need to identify their decay products: electrons. Upsilons do decay to pions and other hadrons, but the two-body lepton decay is the easiest to reconstruct with a minimal background compared to hadronic processes. We focus exclusively on electrons in these analyses. Taus immediately shower, making reconstruction difficult, and STAR is unable to distinguish muons from pions, leading to an insurmountable background signal. However, the recent completion of the **M**uon **T**elescope **D**etector (MTD) will allow STAR to accurately identify muons, opening up a new channel to study the Υ [**126**].

6.5.1. Ionization Energy Loss. As discussed in Sec. 5.4, the TPC is capable of measuring the ionization energy loss of charged particles (dE/dx). Each particle has a characteristic energy-loss profile as a function of momentum (see Fig. 5.5). However, at higher momenta ($p >\sim 3$ GeV/c), the hadronic bands approach the electron band, making discrimination difficult.

For ease of analysis, the energy loss is translated into a new variable, $n\sigma_e$, defined as:

$$n\sigma_e = \frac{\log\left(\frac{dE}{dx}_{\text{meas.}}\right) - \log\left(\frac{dE}{dx}_{\text{exp.}}\right)}{\log\left(\sigma_{dE/dx}\right)} \tag{6.1}$$

where $\frac{dE}{dx}_{\text{meas.}}$ is the measured energy loss, $\frac{dE}{dx}_{\text{exp.}}$ is the expected energy loss of an electron at the measured momentum, and $\sigma_{dE/dx}$ is the detector resolution, which depends on, amongst other things, track length, hit position, and track momentum. The resulting distribution of electrons is a normal distribution centered at zero with a width of one. This variable can also

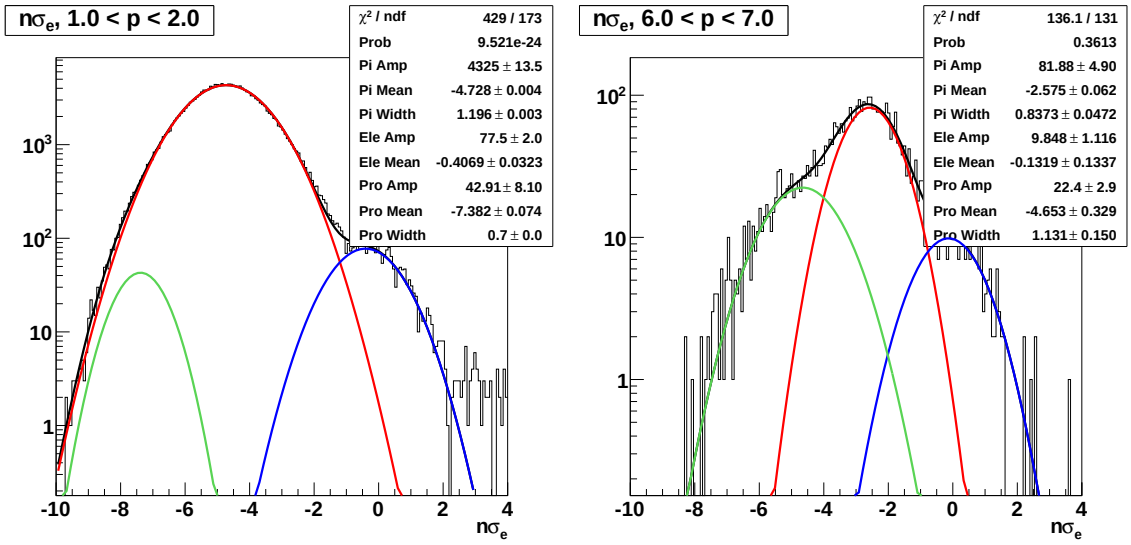

FIGURE 6.4. Example $n\sigma_e$ distributions from the Au + Au dataset. The left figure depicts the distribution at low momentum while the right figure shows higher momenta. Tight cuts on cluster-matching and E/p were applied to enhance the relative number of electrons in the sample. Electrons are shown in blue, pions in red, and protons in green. Notice how the electron curve merges with the pion curve at high momentum.

be calculated for pions, kaons, protons, or any other charged particle. These distributions would look very much like the $n\sigma_e$ distributions shown here, but would instead have a value of zero near the center of the distribution of the chosen particle instead of being zero near the center of the electron distribution. However, slight miscalibrations can lead to an offset in the mean and a change in resolution. To account for this, we fit the distributions from data to get the true parameters. Example $n\sigma_e$ distributions from the Run 10 Au + Au dataset can be seen in Fig. 6.4. Tight cuts on cluster-matching and E/p were applied to enhance the relative number of electrons in the sample. The distributions were fit with the sum of three Gaussians representing electrons (blue), pions (red), and protons (green). Notice how the pion band merges with the electron band at higher momentum, making discrimination difficult. Fortunately, any misidentified pions will only contribute to the combinatorial background.

The results of the fits across all momenta are shown in Fig. 6.5. Green curves show proton fits, red curves show pion fits, and the blue show electron fits. The black lines are constant fits to the electron results.

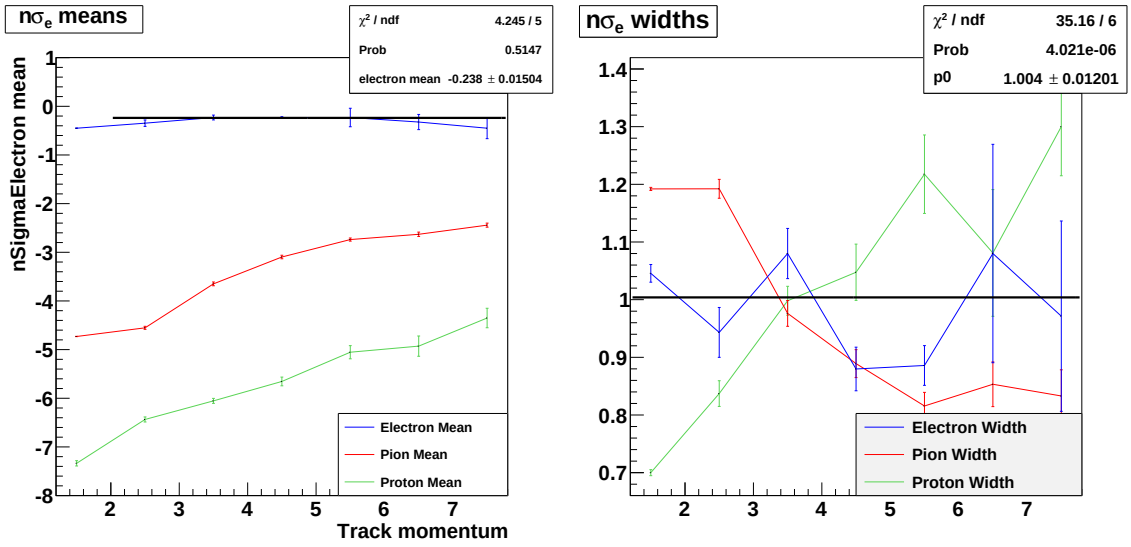

FIGURE 6.5. Summaries of the $n\sigma_e$ fits in Au + Au. Gaussian means as a function of momentum are shown on the left; widths on the right. Electrons are in blue, pions are in red, and protons are in green.

To choose cuts, we optimized the effective Υ signal:

$$S_{\text{eff}} = \frac{S}{2B + S}$$

where S, the signal, is the number of electron-electron pairs, and B, the background, is the number of electron-hadron and hadron-hadron pairs. Since the means of all but the rarest hadrons fall below electrons in $n\sigma_e$, we fixed the upper bound at $n\sigma_e < 3.0$.

To choose the appropriate lower bound, we optimized the pair-wise effective signal through Monte Carlo simulations. First, we obtained the electron, pion, and hadron yields in each momentum bin by loosening the E/p cut to $0.1 < E/p < 1.9$ to allow most particles back in. We then refit the $n\sigma_e$ spectra, keeping the means and widths fixed from the previous fits but allowing the yields to float. Using the shapes obtained from these fits, we calculate the relative fraction of electrons and hadrons for a given lower $n\sigma_e$ cut which we then use to calculate S_{eff}. S_{eff} as a function of the lower $n\sigma_e$ cut for the momentum bin $4 < p < 5$ is shown in Fig. 6.6. Note the slight difference between the peaks of the effective signal for single electrons (red) and electron pairs (blue). The final cut was chosen by taking the average of the maximum S_{eff} for the bins $4 < p < 5$ and $5 < p < 6$, as many of our candidate electrons fall in these ranges. Cuts for all systems are shown in Tab. 6.3.

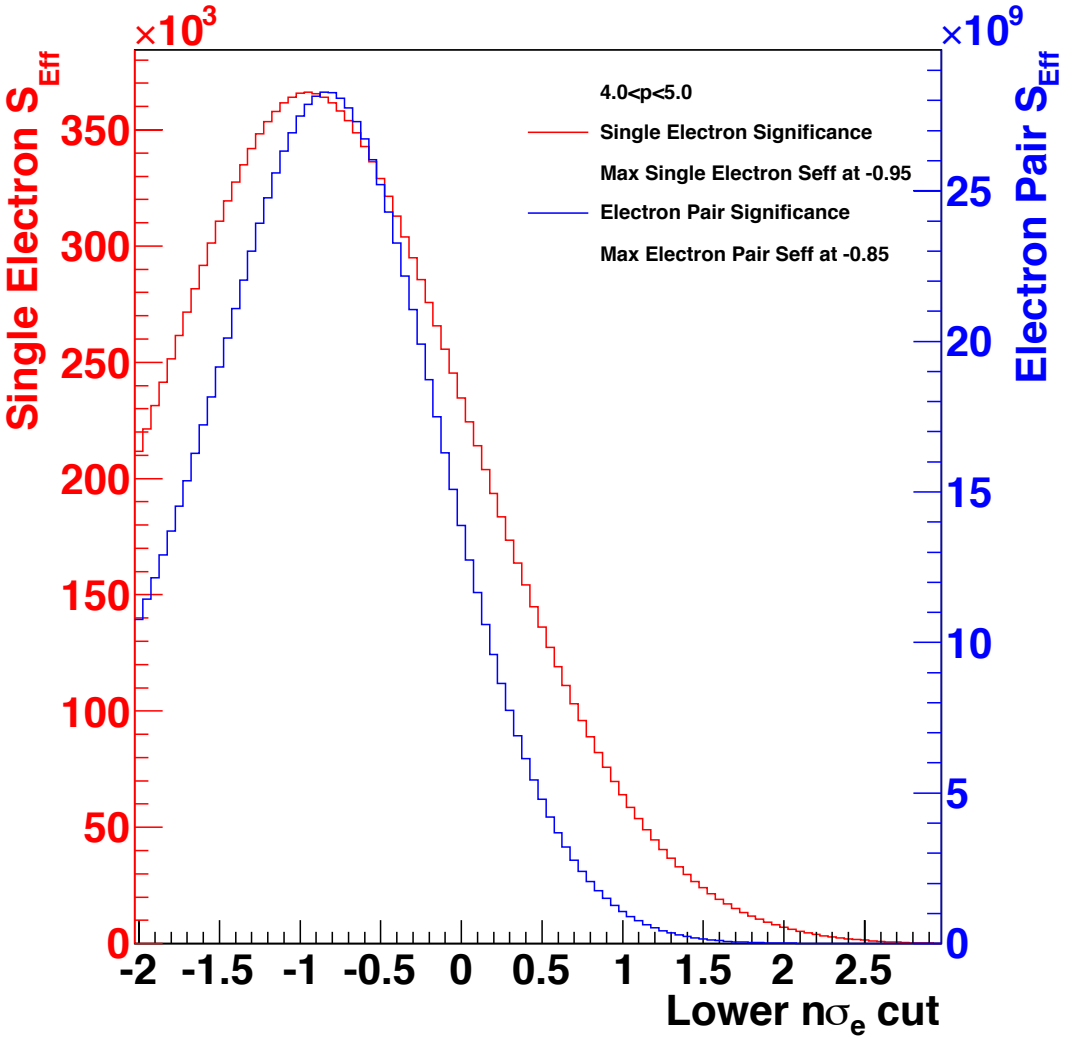

FIGURE 6.6. Effictive signal in $p+p$ for a typical momentum bin. The red curve shows the effective signal for single electrons whereas the blue curve shows the effective signal for electron pairs.

6.5.2. Cluster Matching. Electrons and photons will deposit energy in the BEMC via showering. Pions and muons are too massive to effectively dissipate their energy in the

System	Low $n\sigma_e$ cut	High $n\sigma_e$ cut	Efficiency of $n\sigma_e$ cut
$p+p$	-1.23	3.0	$0.854^2 = 0.729$
$d+\mathrm{Au}$	-1.45	3.0	$0.858^2 = 0.736$
$\mathrm{Au}+\mathrm{Au}$	-1.20	3.0	$0.77^2 = 0.593$

TABLE 6.3. Cuts in $n\sigma_e$ for each system. The cuts were chosen by optimizing S_{eff} for each system.

same manner as electrons within the length of a BEMC tower. However, pions can deposit energy in the calorimeter if they happen to collide with a Pb nucleus, sending a spray of slower protons through the tower. Fortunately, some of the pion's initial energy typically escapes, allowing us to remove them via judicious E/p cuts. We can identify electrons by looking for tracks in the TPC which point to appropriately energetic in the BEMC.

Clustering starts by finding seed towers. In $p+p$ and $d+\mathrm{Au}$, the seed towers are defined by the L0 and L2 triggers since we are only interested in electrons which fire the L2 Υ trigger. In $\mathrm{Au}+\mathrm{Au}$, we can use the L0 HT trigger to define the seed for one of the daughter electrons. However, the second daughter is unrelated to the trigger, giving us freedom to define it. Seed towers for the second daughter are chosen those above 1.5 GeV without any neighbors with more energy. This threshold was chosen as a compromise between two competing factors: raising the cut removes the large soft background and lowering the cut expands our p_T space. By placing the seed threshold at 1.5 GeV, we end up with cluster energies on the order of 2.0 GeV. At this level, all of the soft processes are removed and we lose only the most geometrically unfortunate Υ decays in the range 3 GeV/c $< p_T <$ 7 GeV/c.

Using each seed, a cluster is formed using the two most energetic neighbors. Studies of the cluster shapes have found them to be compact (i.e. the two additional towers shared an edge or corner). The center of the cluster is defined as the energy-weighted average of the position of the towers used to form this cluster.

Each track in the TPC is modeled as a piecewise helix (as discussed in Sec. 5.4) which can be extended beyond the active region of the detector. Using the helical parameters of the final track segment, tracks are projected out to the SMD layer of the BEMC. The distance between the projected track and cluster center, $\Delta R = \sqrt{\Delta\eta^2 + \Delta\phi^2}$, where $\Delta\eta$ is the distance in η between the location of the track projection and the energy-weighted center of the cluster and $\Delta\phi$ is the analogous quantity in azimuth, can then be used to identify electrons. An example distribution from the $p+p$ dataset can be seen in Fig. 6.7.

6.5.3. E/p. Once we match a track to a BEMC cluster as described in the previous section, we can compare the momentum of the track as measured by the TPC to clusters of energy deposited in the BEMC. Energy carried by a relativistic particle is described

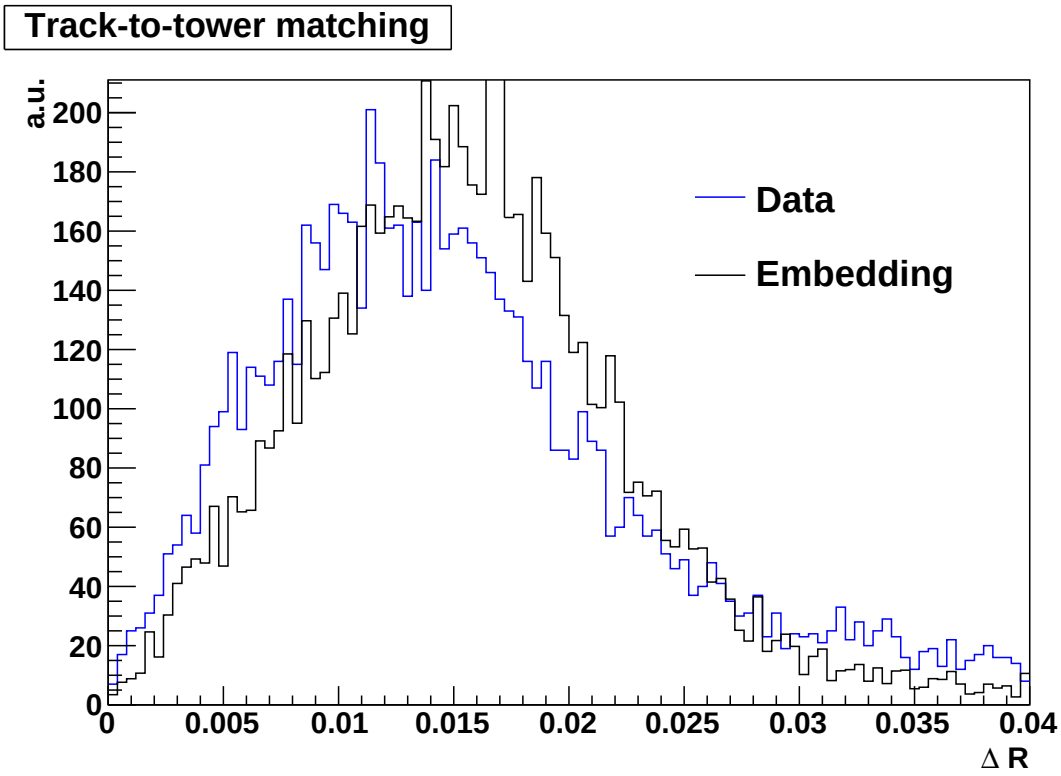

FIGURE 6.7. Distance between projected TPC track and BEMC cluster from $p+p$ data (blue) and embedded simulations (black).

by the equation $E^2 = p^2 + m^2$. Decay daughters from an Υ at rest have a momentum of ~ 4.5 GeV/c. Since electrons are quite light in comparison, their energy-to-momentum ration (E/p) should be very close to one. The width of the E/p resolution due to detector resolution effects is much larger than the natural difference from one, so for our intents and purposes, we can consider it to be one. Pions and other light hadrons will also have an E/p close to one at this energy. However, they are too heavy to effectively deposit their energy in the BEMC and will thus have an E/p value well below one.

To study the E/p distributions, we harvested a collection of individual tracks from real data. In order to enhance the fraction of electrons in the sample relative to hadrons, we used overly-tight $n\sigma_e$ cuts ($0.5 < n\sigma_e < 3.0$). These cuts were chosen for their high electron purity despite their low efficiency ($< 50\%$). Example distributions from the $p+p$ and $d+$Au datasets can be see in Fig. 6.8.

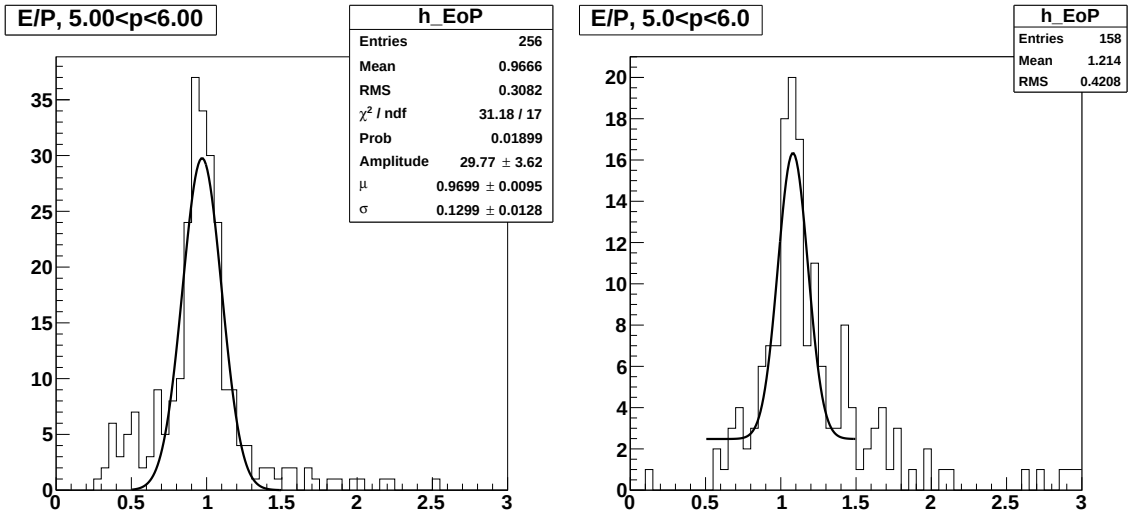

FIGURE 6.8. E/p distributions in the range 5 GeV/c $< p <$ 6 GeV/c for $p+p$ (left) and $d+\mathrm{Au}$ (right).

When analyzing the E/p distributions in the $\mathrm{Au}+\mathrm{Au}$ dataset, we split the tracks into two sets: those that matched a tower which could have fired the L0 trigger (Fig. 6.9) and those that did not (Fig. 6.10). Since the $\mathrm{Au}+\mathrm{Au}$ dataset was collected without the L2 trigger, the trigger only required one high tower in the BEMC instead of two clusters. Hence, only one track is guaranteed to match to a clean signal in the BEMC. By comparing the tracks that matched the triggering tower (Fig. 6.9) to those that did not (Fig. 6.10), the broadened distribution is readily apparent. The fits to the untriggered track were not robust to different fitting methods. We chose, therefore, to only cut on the E/p of the triggering track. The second track was only required to match to a cluster of energy in the BEMC as imposed by the R_{match} cut (see Sec. 6.5.2). We also used a much wider set of cuts in this dataset than in $p+p$ and $d+\mathrm{Au}$ due to the broader distribution in order to match the single-track efficiency of the cut (see Tab. 6.4).

6.6. Invariant Mass Spectrum

System	Low E/p cut	High E/p cut	Efficiency of E/p cut
$p+p$	0.7	1.3	$0.965^2 = 0.931$
$d+\mathrm{Au}$	0.8	1.23	$0.955^2 = 0.912$
$\mathrm{Au}+\mathrm{Au}$ (0-60%)	0.7	1.5	0.967

TABLE 6.4. Cuts in E/p for each system.

6.6.1. Line Shapes. Inherent limitations in the detectors lead to modifications of the invariant-mass line shape. Furthermore, material between the interaction region and the TPC can lead the daughter electrons to bremsstrahlung, creating a tail in the mass distribution. To model these effects, we simulate Υ decays, run the results through GEANT to simulate detector effects, and embed the results in real data (see Sec. 6.3). Using our standard analysis maker, we can extract the embedded Υ.

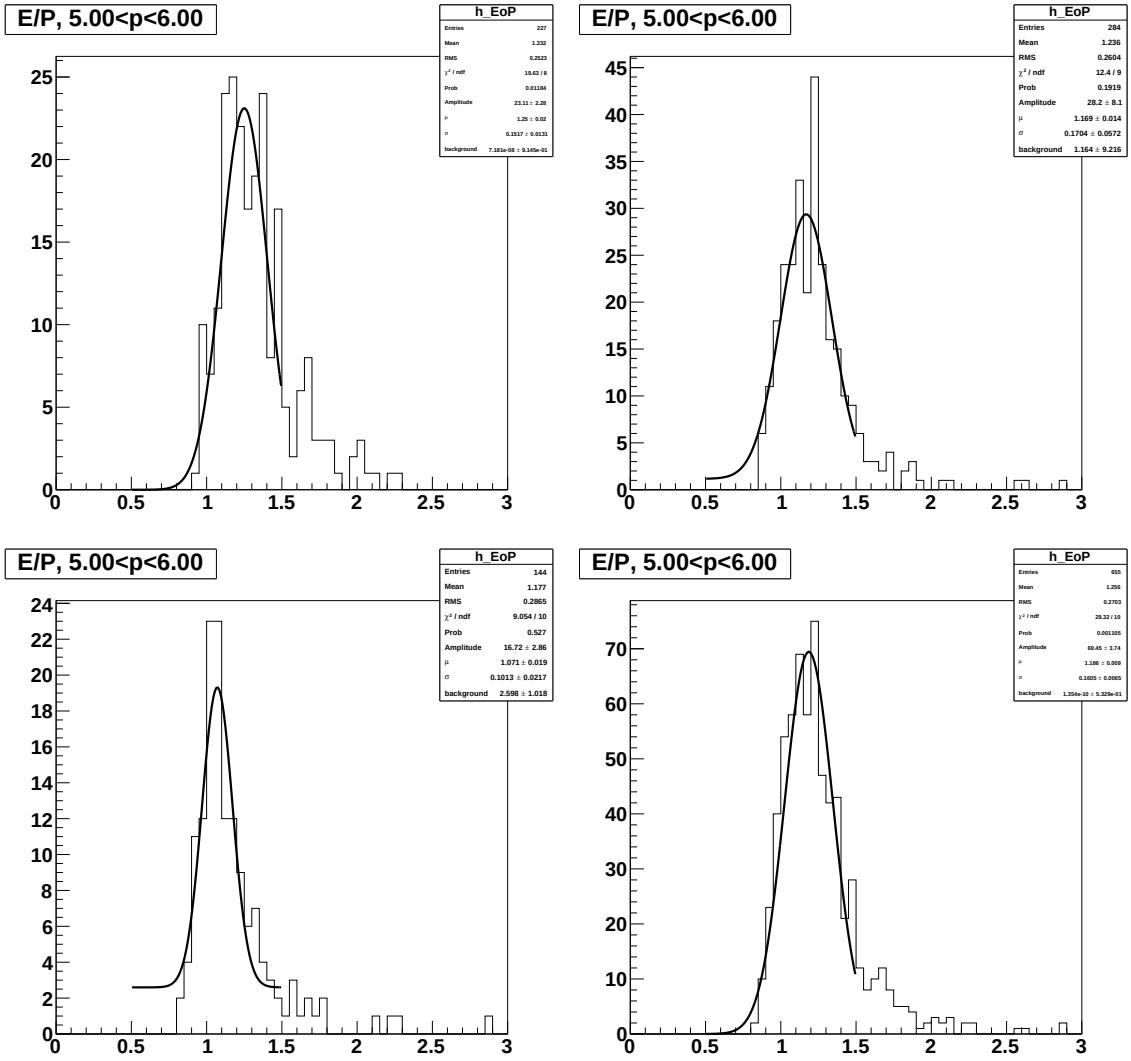

FIGURE 6.9. Examples of E/p distributions in Au + Au for tracks matched to a tower which could have fired the L0 trigger. From left to right, top to bottom, we show data from 0-10%, 10-30%, 30-60%, and 0-60% centrality collisions. Note the broadening of the E/p distribution as we move to more central collisions and the TPC occupancy increases.

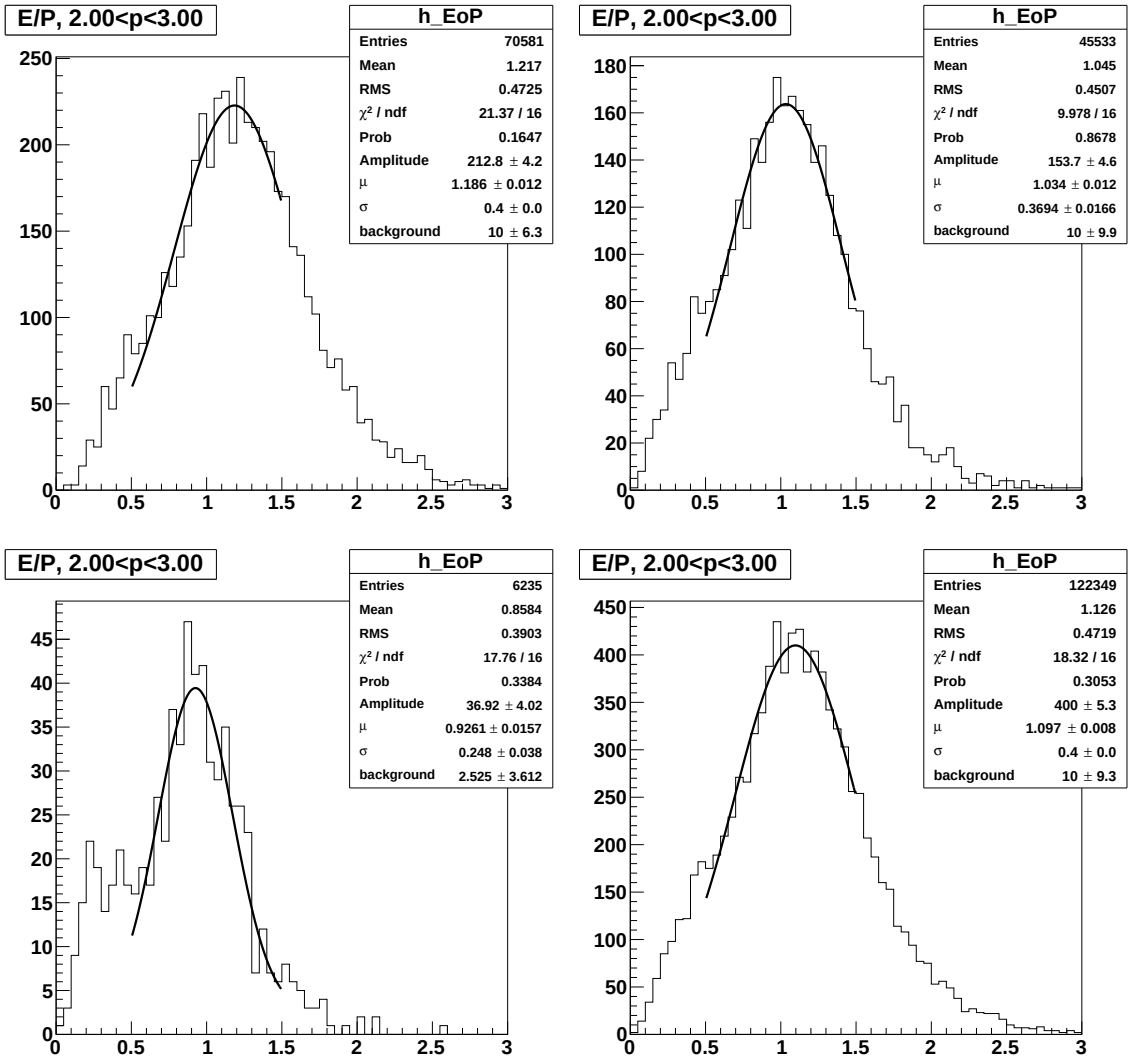

FIGURE 6.10. Examples of E/p distributions in Au + Au for tracks not matched to a tower which could have fired the L0 trigger. Almost all tracks paired with a L0-triggering track are of this class. From left to right, top to bottom, we show data from 0-10%, 10-30%, 30-60%, and 0-60% centrality collisions. The distributions here are much wider than for the L0-matched tracks (Fig. 6.9).

We fit the line shape with a Crystal Ball function, so named for the Crystal Ball experiment [**127**]. The Crystal Ball function pairs a Gaussian with a power-law tail (see Fig. 6.11). It is used to model "lossy" functions, such as possible bremsstrahlung radiation, and is continuous and differentiable at all points. Along with the parameters for a Gaussian (mean (μ) and standard deviation (σ)), the Crystal Ball function has two additional parameters: α and n. The parameter α is the distance in standard deviations (σ) below the

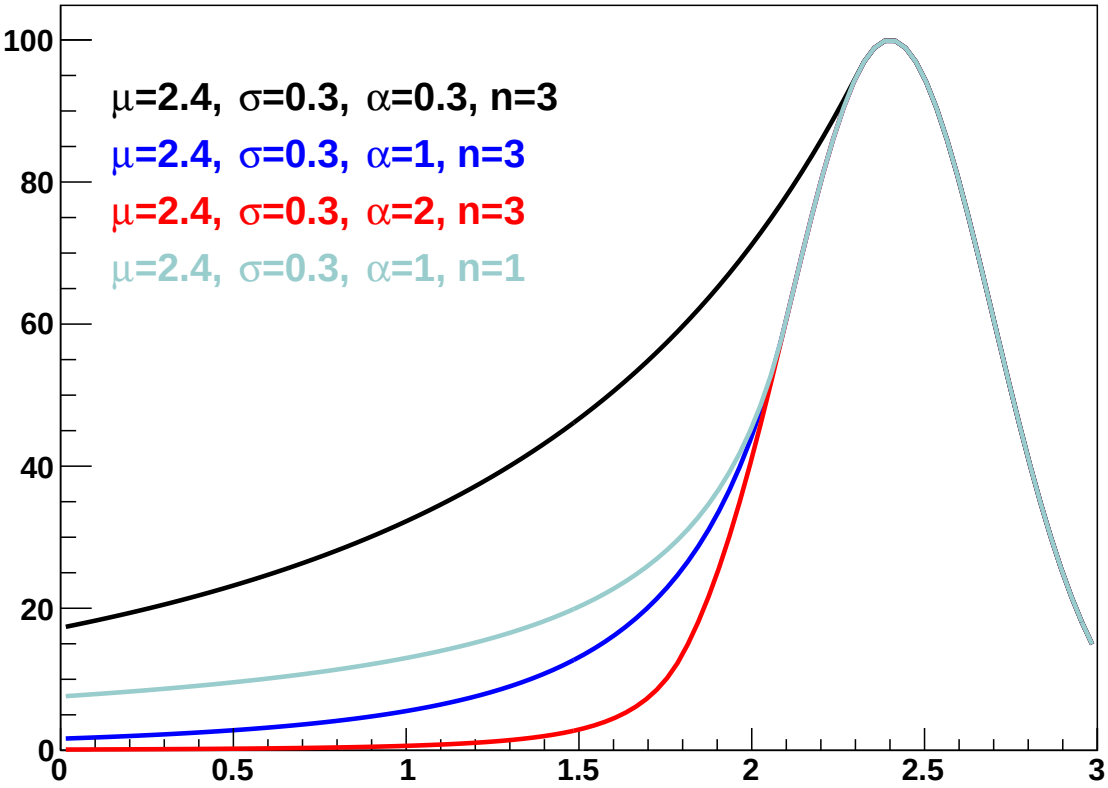

FIGURE 6.11. Four examples of Crystal Ball functions. The normalization (not shown) and Gaussian parameters are left unchanged. The α parameter controls when the function transitions from a Gaussian to a power law. The n parameter is the power in the power law.

mean (μ) where the function transitions from a Gaussian to a power law. The parameter n is the exponent in the power law.

After applying our analysis cuts and reweighing the rapidity and transverse momentum distributions of the embedded data to have realistic distributions, the reconstructed invariant-mass spectrum is fit for each individual state. Example fits to the reconstructed $p+p$ mass spectrum for a wide rapidity range ($|y| < 1.0$) are shown in Fig. 6.12.

Due to resource constraints, we were unable to produce Υ embedding in the 2010 Au + Au environment. However, single electrons were embedded into 2010 Au + Au events. Since Υ decay within a few picometers of the event vertex, the detector only sees two, primary electrons. Using PYTHIA we simulated $\Upsilon \rightarrow e^+e^-$ decays and used the electron

embeddings to recreate the detector response to each electron. By analyzing these combined events, we can extract our desired information about the detector response, such as the Υ line shape.

Fortunately, we had both Υ and electron embedding in $p+p$. As a proof of concept, we recreated the Υ embedding results (e.g. triggering efficiencies and acceptance) from the electron embedding and compared the results to the direct Υ embedding. We had remarkable agreement. Example plots can be seen in Fig. 6.13.

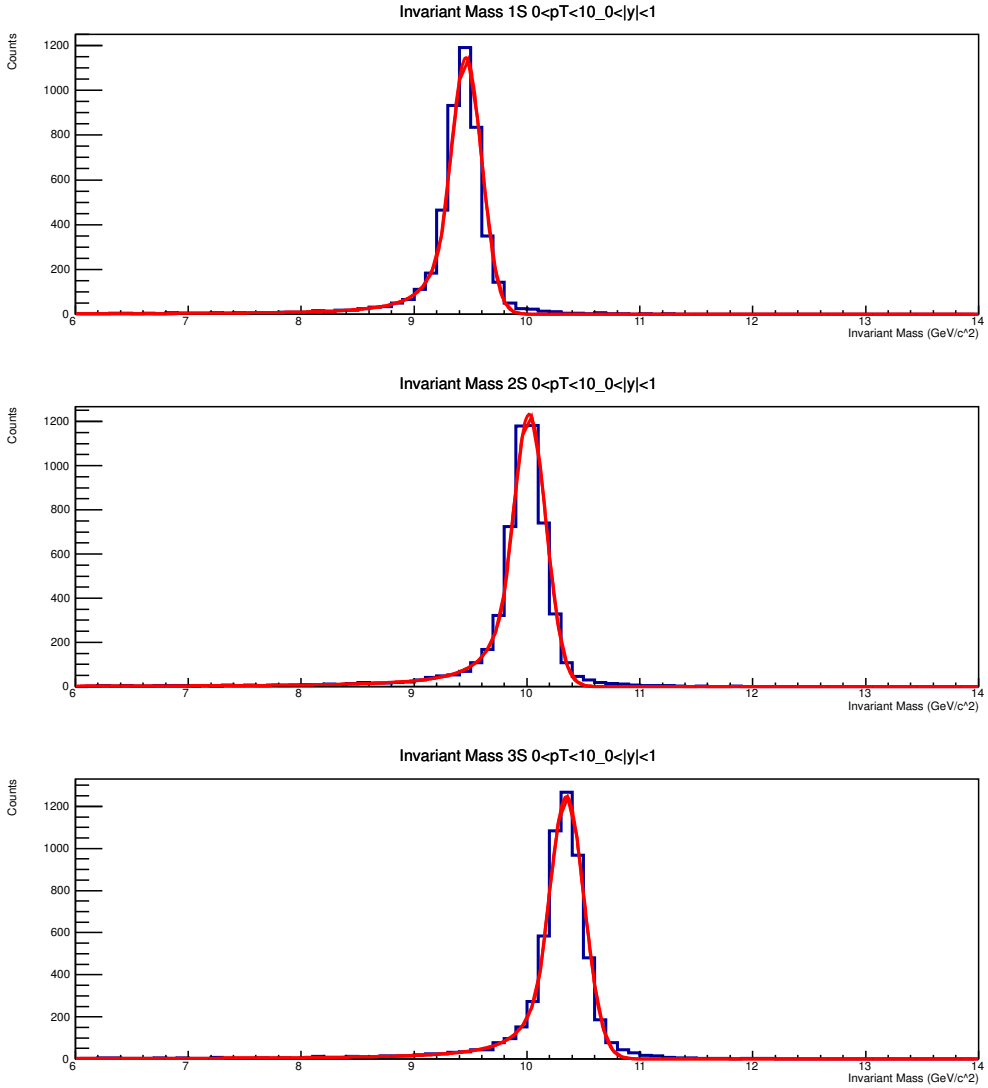

FIGURE 6.12. Crystal Ball fits to results from $p+p$ embedding for $|y| < 1.0$. The top is $\Upsilon(1S)$, the middle is $\Upsilon(2S)$, and the bottom is $\Upsilon(3S)$.

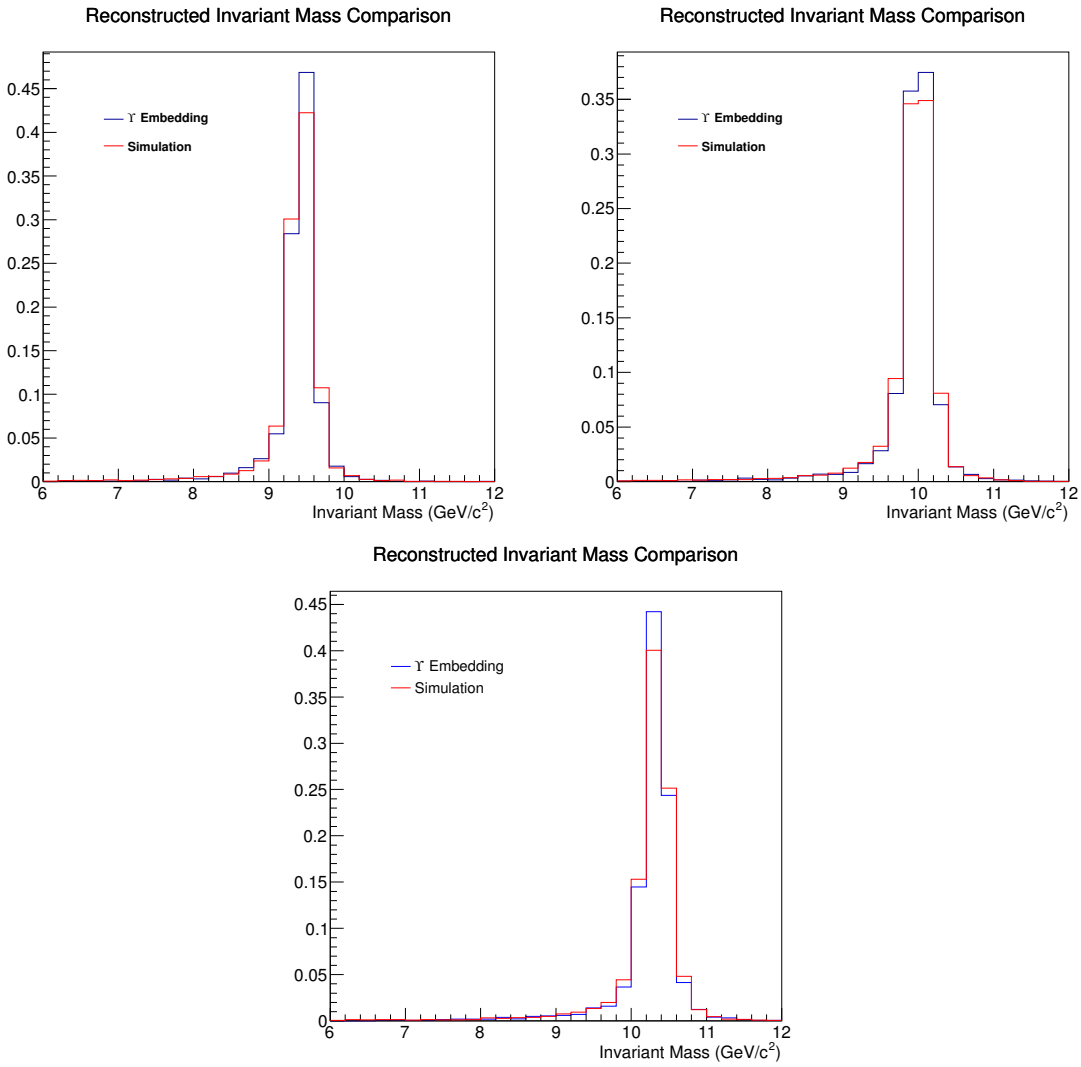

FIGURE 6.13. Comparison between line shapes extracted from direct Υ embedding (blue) and from simulations using electron embeddings (red). From left to right, top to bottom, we show $\Upsilon(1S)$, $\Upsilon(2S)$, and $\Upsilon(3S)$.

In 2007, a new set of TPC alignment measurements were taken. After being used for data production through 2010, an alignment issue was discovered. In one half of the TPC, the ratio of positively charged to negatively charged particles ($h+/h-$) diverged from unity as transverse momentum increased. When the TPC calibrations have a rotational misalignment, tracks of one charge are reconstructed with additional curvature and those of the other charge are reconstructed with less. This problem affected all three of our datasets. Fortunately, this problem could be corrected by using the 2003 alignment calibrations, but this required a complete reproduction of the data.

Due to resource constraints, STAR chose only to reproduce the 2009 $p+p$ dataset. We reran our analysis maker on the corrected data. By comparing Υ found in both productions, we can see the effect of the misalignment on reconstructed mass. For the purposes of studying the effects of the misalignment, we restricted our analysis to Υ with the following properties: 1) an Υ was found in the same event in both the corrected and uncorrected data; 2) the two reconstructed vertices had values of V_z within 1.0 cm of each other; 3) the reconstructed daughter electrons in both datasets are within 0.2 in η and 0.2 in ϕ. A two-dimensional histogram showing the difference between the reconstructed mass in the corrected and uncorrected datasets against the mass found in the uncorrected dataset can be seen in Fig. 6.14.

To account for this effect in the uncorrected $d+\mathrm{Au}$ and $\mathrm{Au}+\mathrm{Au}$ datasets, we modified the line shapes based on the differences seen in the $p+p$ dataset. The histogram in Fig. 6.14 was projected onto the x-axis and fit with a Gaussian as shown in Fig. 6.15. We then smeared the line shape obtained from embedding with a Gaussian of the same width as the fit in Fig. 6.15. An example refit is shown in Fig. 6.16.

6.6.2. Fitting. We used the RooFit [**128**] analysis package to fit to our invariant mass spectra. This allowed us to perform simultaneous fits to the like-sign and unlike-sign spectra. In the past, we subtracted the like-sign spectrum from the unlike-sign to remove the combinatorial background. However, we greatly reduce the signal-to-uncertainty ratio in the lower-mass bins by not subtracting our spectra.

Furthermore, in the $p+p$ and $d+\mathrm{Au}$ datasets, the like-sign spectrum contains information about the turn-on imposed by the conditions of the L2 trigger. This effect is modeled by an error function with two parameters: a mean and a width. The mass threshold for the L2 turn-on (the mean of the error function) is near the mass of the Υ, making it difficult to disentangle the exact turn-on position and width from the $\Upsilon(1S)$ mass peak. The like-sign spectrum is solely comprised of the combinatorial background, which is modeled by an exponential function. This makes the turn-on effect from the L2 trigger much less ambiguous than in the unlike-sign spectrum. By fitting to the like-sign spectrum at the same time as the unlike-sign, we gain additional constraints on the L2 parameters compared to

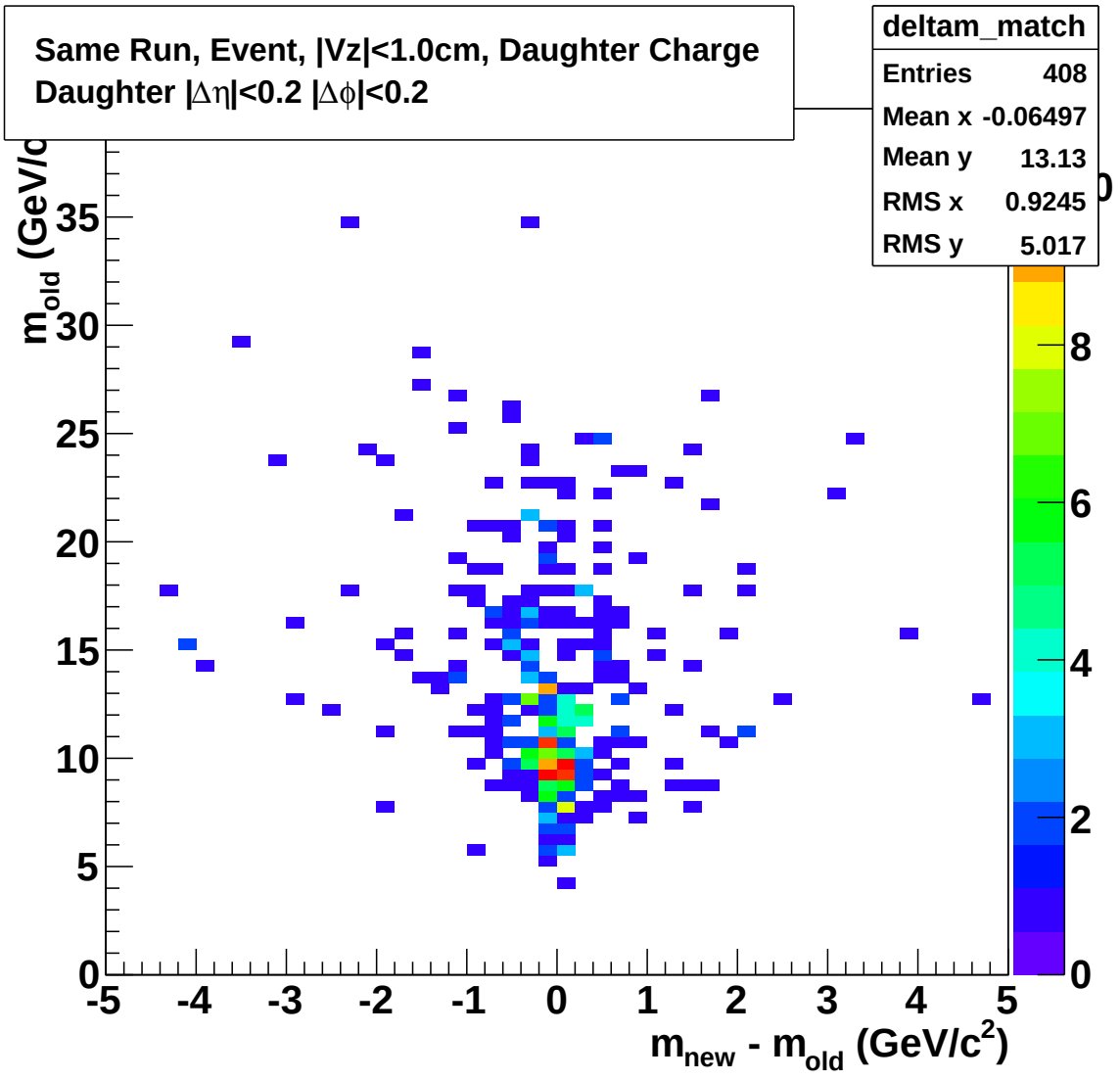

FIGURE 6.14. Difference between reconstructed mass in the corrected and uncorrected $p+p$ datasets compared to the mass found in the uncorrected dataset.

fitting after subtraction. The increased precision in the L2 parameters translates to reduced uncertainty in our extracted yields.

In $p+p$ fits, the ratios of Υ(1S) to Υ(2S) and Υ(3S) were fixed. The ratios were calculated through two methods: 1) using relative production measurements from Fermilab [**129**] and 2) $\Upsilon \rightarrow e^+e^-$ branching ratios from the PDG data book [**11**] combined with production cross sections from NLO calculations (for further details, see [**8**], section IV). The PDG data book does not have a branching ratio for $\Upsilon(3S) \rightarrow e^+e^-$, so the branching

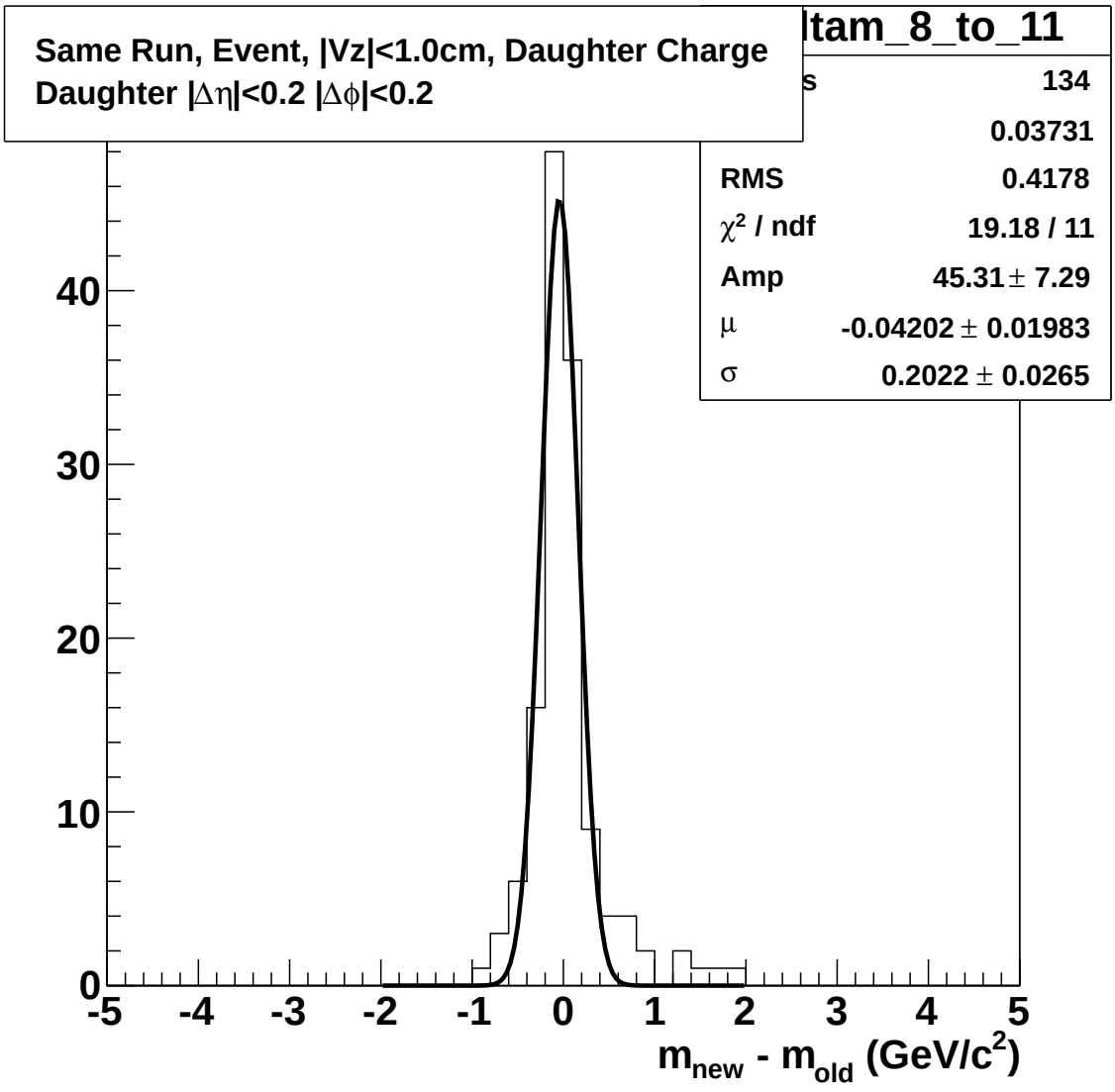

FIGURE 6.15. Projection of Fig. 6.14 onto the Δm axis. The black curve is a Gaussian fit to the projection. Parameters are listed in the upper right corner.

ratio for muons was used instead assuming lepton universality. In $d+\mathrm{Au}$ and $\mathrm{Au}+\mathrm{Au}$ fits, the ratio of $\Upsilon(2S)$ to $\Upsilon(3S)$ was fixed, but their combined yield was allowed to float relative to the $\Upsilon(1S)$. The ratio of the excited states to the ground state was constrained such that it could never go above its value in $p+p$ system. That is, in $d+\mathrm{Au}$ and $\mathrm{Au}+\mathrm{Au}$ collisions, it was assumed that the ground state would never be more suppressed than the excited states.

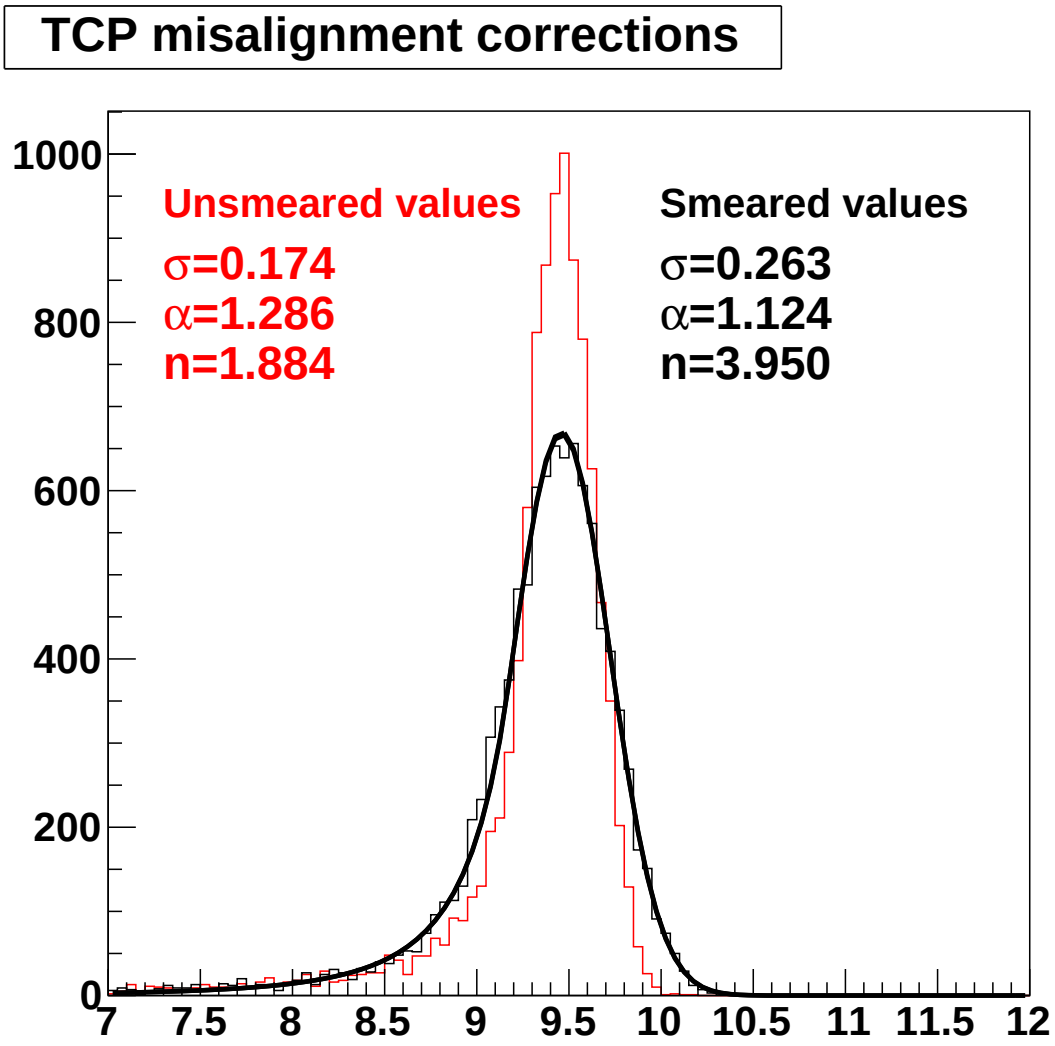

FIGURE 6.16. Υ(1S) line shape before (red) and after (black) the additional smearing from the TPC misalignment. This example is from 0-60% centrality Au + Au.

Fitting was performed using RooFit. Specifically, the like-sign and unlike-sign spectra were fit simultaneously using a maximum likelihood method. In the $p+p$ fits, there were seven parameters:

(1) yield of the combinatorial background (CB)

(2) CB exponential slope parameter

(3) L2 error function turn-on location

(4) L2 turn-on width

(5) Drell-Yan yield

(6) correlated $b\bar{b}$ decays

(7) Υ(1S+2S+3S) yield.

Fits to the d + Au signals have all of the same parameters as well as a parameter controlling the fraction of excited states to Υ(1S). The Au + Au fits have a slightly different set of parameters due to the lack of L2 trigger. Au + Au fits have the following eight parameters:

(1) two combinatorial background yields

(2) two combinatorial background exponential slope parameters

(3) Drell-Yan yield

(4) yield of correlated $b\bar{b}$ decays

(5) Υ(1S+2S+3S) yield

(6) the relative fraction of excited states to what one would expect in $p+p$ collisions

For each dataset, we split the signal up into different kinematic regions for various reasons. In all cases, the signals are p_T-integrated. In the $p+p$ system, the signal was split into two rapidity regions: $|y| < 0.5$ and $0.5 < |y| < 1.0$ (see Fig. 6.17). The main purpose for this split is the shape of the background imposed by the L2 trigger. The mass cuts in the L2 trigger assume a vertex at $V_z = 0$ (see Tab. 6.1). Vertices displaced from the center of the TPC have increased acceptance of either forward or backward Υ, depending on the direction of the shift. As the reconstructed parent particle moves further away from $y \approx 0$, the average vertex position shifts further and further away from $V_z = 0$. Hence, it made sense to split the $p+p$ Υ measurement into these two rapidity bins. This also allows us to report a rapidity spectrum (see Sec. 7.1).

The d + Au signal was split into three regions: $-1.0 < y < -0.5$, $|y| < 0.5$, and $0.5 < y < 1.0$ (see Fig. 6.18). Unlike in $p+p$, we did not combine the forward and backward rapidity regions since the system is no longer symmetric in rapidity. As can be seen in Fig. 6.18, the Au-going direction ($-1.0 < y < -0.5$) has a much larger Drell-Yan and correlated $b\bar{b}$ decay background than the deuteron-going direction ($0.5 < y < 1.0$).

Since the Au + Au dataset was collected with only the L0 trigger and not the L2 trigger, the mass turn-on is well below the Υ mass (~ 5.0 GeV/c^2) and is not sensitive to the vertex position. This makes it possible to combine the dataset across rapidities when fitting to

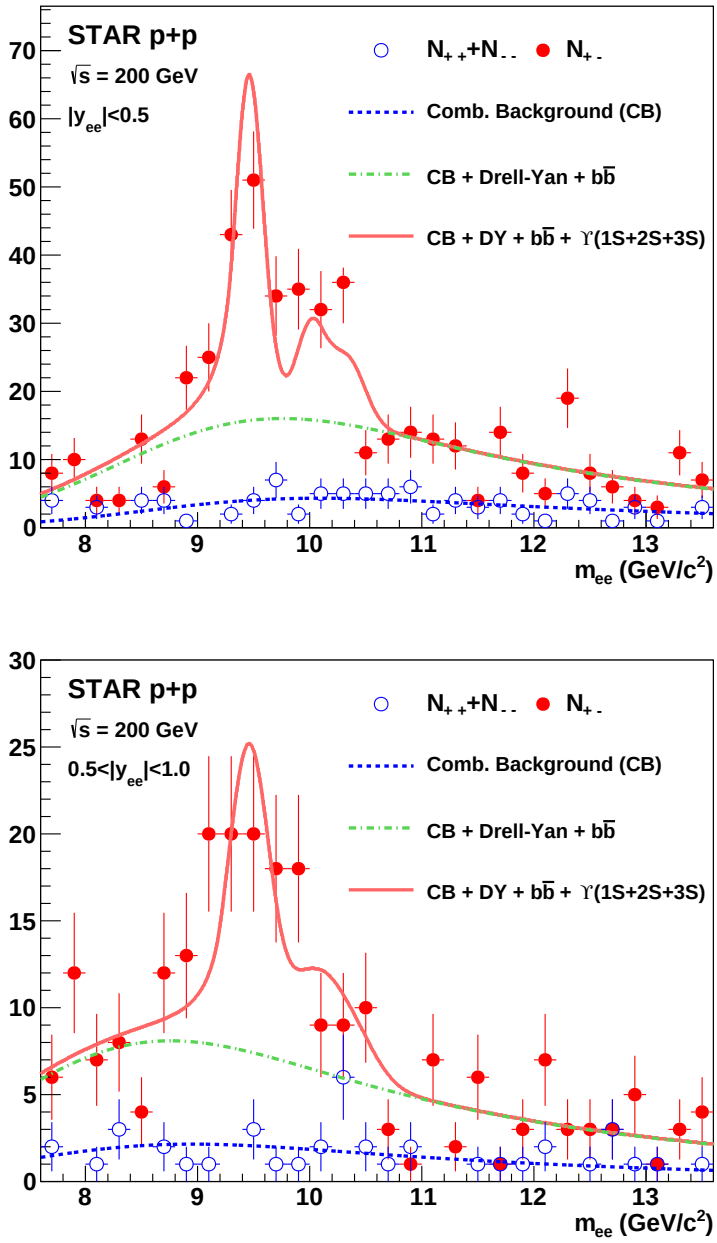

FIGURE 6.17. Fits to the Υ signal in $p+p$. The top plot shows midrapidity ($|y| < 0.5$) and the bottom plot shows "side" rapidity ($0.5 < |y| < 1.0$). The hollow blue circles are the like-sign counts and the fit to the background is shown as a dashed blue line. The filled red circles are the unlike-sign counts and the total fit to the signal and background is shown as a solid red line. The dot-dashed green line shows the combined fits to the background, Drell-Yan signal, and correlated $b\bar{b}$ signal.

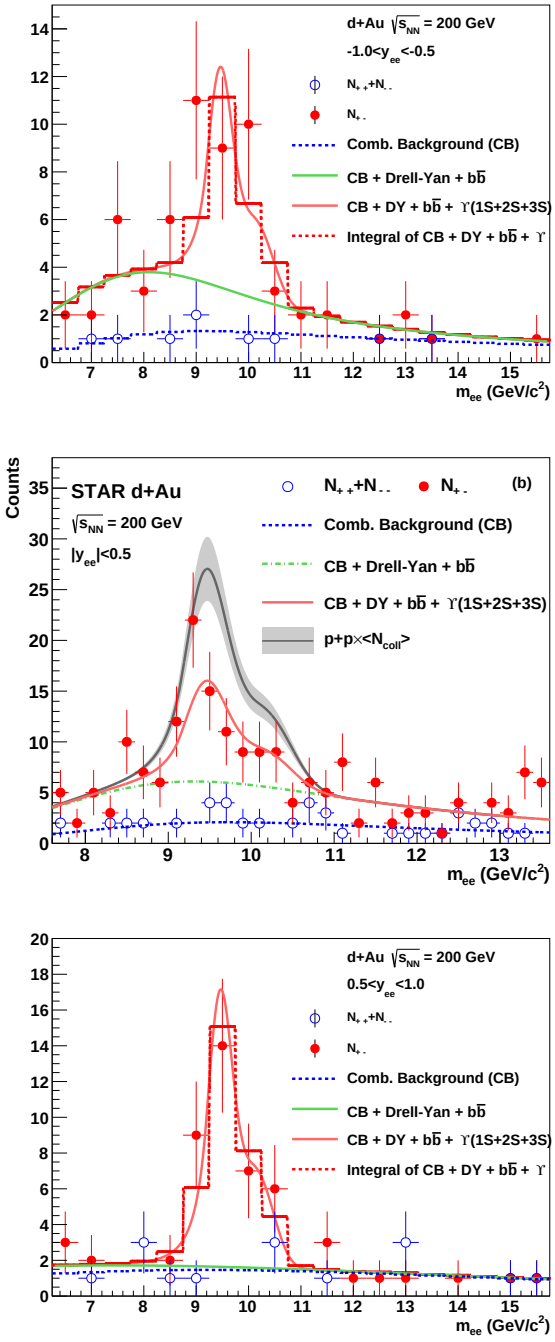

FIGURE 6.18. Fits to the Υ signal in $d+\mathrm{Au}$. From top to bottom, the fits cover the ranges $-1.0 < y < -0.5$, $|y| < 0.5$, and $0,5 < y < 1.0$. Explanation of most the legend can be found in the caption of Fig. 6.17. In addition, the gray band in the center plot shows the expected N_{coll}-scaled Υ(1S+2S+3S) signal if there is no suppression.

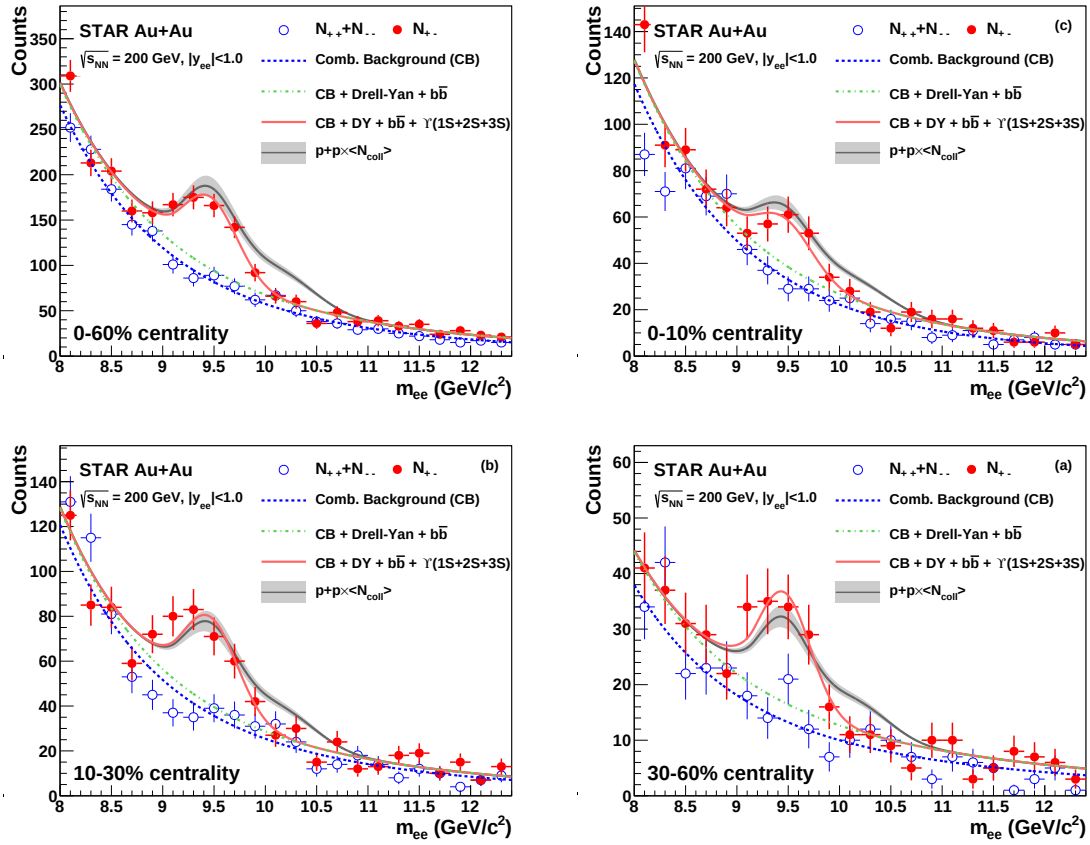

FIGURE 6.19. Fits to the Υ signal in Au + Au in the rapidity range $|y| < 1.0$. From left to right, top to bottom, the fits cover the centrality ranges 0-60%, 0-10%, 10-30%, and 30-60%. Explanation of the legend can be found in the captions of Figs. 6.17 and 6.18.

the invariant mass spectrum. With this in mind, we had two rapidity bins: $|y| < 0.5$ and $|y| < 1.0$. Using the STAR StRefMultCorr class [**130**], which deduces centrality from a corrected reference multiplicity based on instantaneous luminosity and vertex position, we split the data into four centrality bins: 0-60%, 0-10%, 10-30%, and 30-60%.

6.6.3. Yield Extraction. The yield was extracted using a combination of the fit results and the raw data. The Υ(1S+2S+3S) yield is obtained from the mass range $8.8 - 11.0$ GeV/c^2 (see Fig. 6.21, solid black lines). This range was chosen due to its high efficiency even in the poorest detector conditions ($\sim 92\%$ in Au + Au, 0-10% centrality). The total fit except the Υ(1S+2S+3S) signal (dot-dashed green curve in Figs. 6.17, 6.18, and 6.19) was integrated in the range $8.8 - 11.0$ GeV/c^2 and subtracted from the unlike-sign data

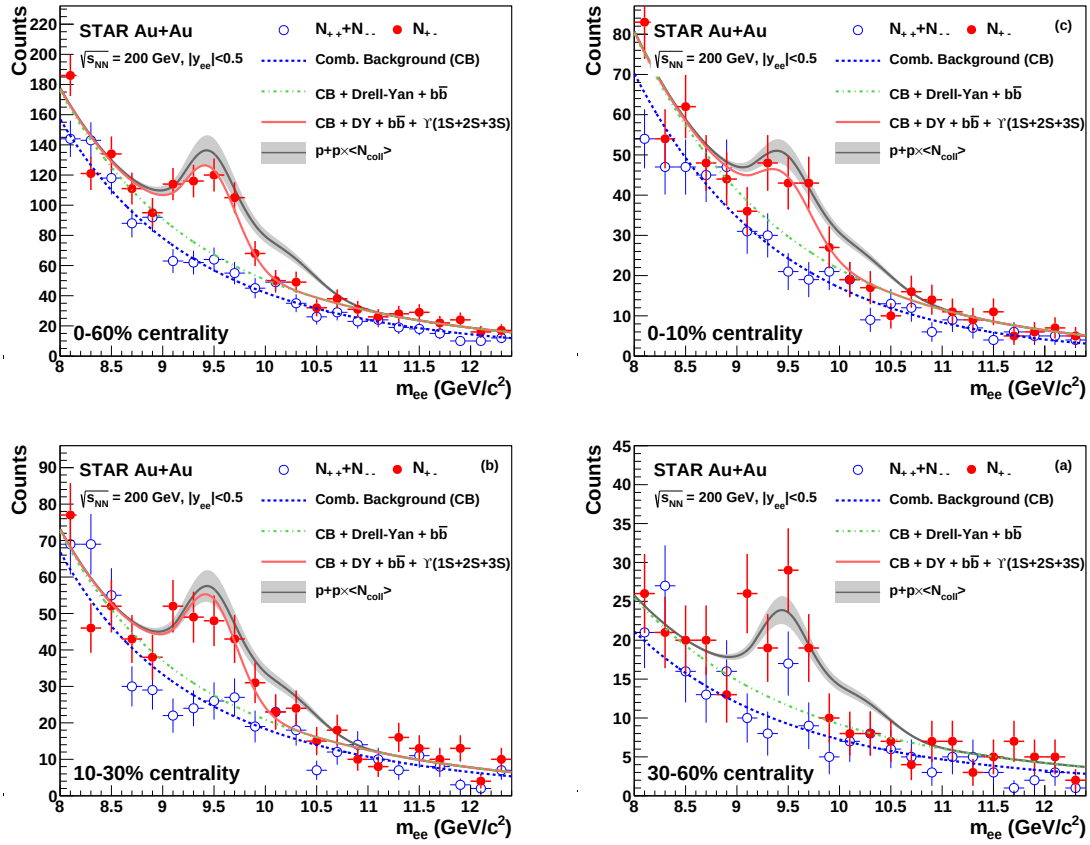

FIGURE 6.20. Fits to the ϒ signal in Au + Au in the narrower rapidity range $|y| < 0.5$.

(red filled circles) integrated in the same range. By extracting the yield this way, we help protect ourselves from biases arising from errors in the assumed line shapes.

To isolate the ground state, ϒ(1S), the counts were extracted from a narrower mass window of $8.8 - 10.0$ GeV/c^2 (see Fig. 6.21, dashed black line). This window was chosen to balance purity, efficiency, and size of systematics. As the upper edge of the mass cut for the ϒ(1S) moves higher in mass, the cut becomes more efficient but less pure as more excited ϒ pass the cut. We also need to take into account sources of systematics when choosing the cuts. There are two dominant sources from this cut: changing ϒ(1S) efficiency as we vary the line shape within fit errors and changing purity as we vary the relative ratio of excited ϒ to ϒ(1S). Using a mass cut lower than 10.0 GeV/c^2 (such as 9.8 or 9.6 GeV/c^2, since the cut can only change by increments of 0.2 GeV/c^2 due to binning) greatly increases our systematic uncertainty since the efficiency becomes very sensitive to the width of the

Gaussian portion of the Crystal Ball line shape. Using a mass cut greater than 10.0 GeV/c^2 leads to a lower purity without much gain in efficiency.

6.6.3.1. *Excited State Upper Limit.* By inspecting the invariant mass spectra shown in Fig. 6.19, one can easily see a lack of signal in the mass range of the Υ(2S+3S) ($\sim$ 10.0−11.0 GeV/c^2). To quantify the suppression of the excited states, we calculate an upper limit using the so-called Rolke method [**131**]. This method is designed to calculate an upper limit in the case of a signal with Poisson statistics and a Gaussian uncertainty in the background. To isolate the Υ(2S+3S) from the Υ(1S) we integrate our signal and background in the range $10.0 - 11.0$ GeV/c^2. As can be see in Fig. 6.21, the signal in this mass region is dominated by the excited states.

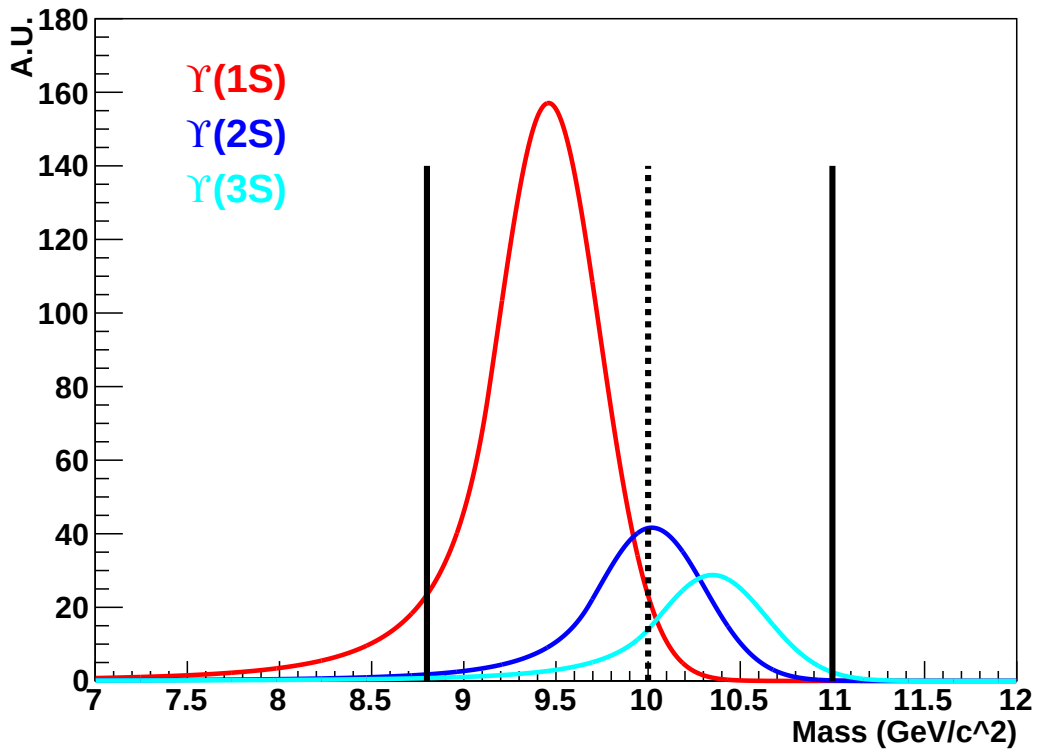

FIGURE 6.21. Mass cuts used for yield extraction shown on an example line shape from Au + Au. For the Υ(1S+2S+3S) yield, the signal is integrated from 8.8 GeV/c^2 to 11.0 GeV/c^2 (solid black lines). The Υ(1S) yield is extracted by lowering the upper mass cut to 10.0 GeV/c^2 (dashed black line).

6.7. Systematics

We had five major sources of systematics: 1) Estimation of integrated luminosity; 2) Geometrical acceptance; 3) Triggering; 4) Electron identification; 5) Fitting. A summary of all investigated sources of systematics can be found in Tab. 6.5.

6.7.1. Luminosity. In the $p+p$ system, the luminosity is determined using measurements from the BBC. Uncertainty in the luminosity measured by the BBC comes from two sources: uncertainty in the $p+p$ non-single defractive (NSD) cross section and uncertainty in the BBC efficiency. Studies have found the NSD cross section to be 26.1 ± 0.2 (stat.) ± 1.8 (syst.) [**132**, **134**]. For our purposes, the systematic error is $1.8/26.1 = 7\%$. The uncertainty in BBC efficiency comes from varying the event generator from PYTHIA to HERWIG. This gives us a relative uncertainty of 9% [**132**].

In $d+\mathrm{Au}$ and $\mathrm{Au}+\mathrm{Au}$, the luminosity is measured by the ZDC.

6.7.2. Geometrical Acceptance. The first aspect of triggering uncertainty comes from the geometrical acceptance which is somewhat distinct from triggering threshold effects. The acceptance uncertainty itself has two main components: dynamically masked BEMC towers and Υ polarization uncertainty.

6.7.2.1. *Masked Towers.* If the electrons do not decay within the acceptance of STAR's BEMC, then we cannot trigger on the decay. Geometrical acceptance is calculated via PYTHIA simulations run through a GEANT model of STAR. We define an electron as falling within the BEMC if it deposits at least 1.0 GeV of energy in the calorimeter towers. The GEANT simulation assumes all 4,800 BEMC towers are active and in use at all times. However, the L2 trigger dynamically masks up to 25 towers to prevent hot towers from firing the trigger. We recalculate the acceptance while randomly masking out up to 25 towers. This study found a 0.5% drop in the acceptance from masked towers.

6.7.2.2. *Polarization.* The acceptance is also affected by assumptions about the Υ polarization. All simulations are done with the assumption that the Υ is unpolarized. By applying the methods described in Ref. [**136**], we can correct for the change in acceptance from two possible polarization modes: transverse and longitudinal. In the transverse case, the acceptance decreases by 1.6%. In the longitudinal case, the acceptance increases by

2.9%. We take these values as upper and lower limits for the systematic uncertainty for the systematic uncertainty on acceptance due to polarization.

6.7.3. Triggering. Both the L0 and L2 triggers are based on signals in the BEMC. Hence, any uncertainties in our simulation of the BEMC response will drive triggering uncertainties.

6.7.3.1. *L0 Trigger.* The L0 trigger is an ADC threshold. By comparing the ADC distributions of electrons from simulation to those from data, we find a 3% shift in the ADC (see Fig. 6.1). The L0 HT threshold is DSM-ADC=18, which is 303 in full ADC counts. To account for this uncertainty, we shift the threshold by 9 ADC counts (3% of 303) and recalculate the triggering efficiency for the Υ(1S). We find a relative change in the efficiency of +8.7% and -2.3%. This effect is smaller for the Υ(2S) and Υ(3S), but the Υ(1S+2S+3S) signal is dominated by the Υ(1S), so taking the relative change calculated for the Υ(1S) is a conservative yet fairly accurate estimate of the systematic effect.

6.7.3.2. *L2 Trigger.* The L2 trigger uses calculated energy instead of ADC for triggering decisions. By comparing the E/p distributions in narrow momentum bins in embedding to data, we can quantify the difference between the response used to calculate our triggering efficiency and the real response. This analysis find a 0.71% shift in the BEMC energy. Running this shift through our embedding results, we find a systematic change due to energy uncertainty of +1.2% and -0.6%.

The L2 trigger also has a cut on track-pair opening angle (see Tab. 6.1). These cuts were far enough away from the signal region as to have a negligible systematic effect.

6.7.4. Electron Identification. To calculate the systematic uncertainty of the E/p cuts, we use the results of our fits described in Sec. 6.5.3. Both the width and mean were varied higher and lower by the fit uncertainty in all combinations. The highest and lowest efficiency were used to calculate the systematic uncertainty in Tab. 6.5.

We followed a similar procedure with the $n\sigma_e$ fits.

6.7.5. Mass Fitting. There are multiple sources of uncertainty with regards to fitting. The first source is the uncertainty in the mass line shape itself through uncertainty in the parameters extracted from the Crystal Ball fits. Second is the uncertainty in the additional

smearing from the TPC misalignment in the $d+\mathrm{Au}$ and $\mathrm{Au}+\mathrm{Au}$ datasets. Finally, we have the change in overall efficiency for detecting the Υ(1S+2S+3S) due to the relative suppression of Υ(2S) and Υ(3S) compared to Υ(1S).

6.7.5.1. *Line Shape Uncertainties.* The uncertainties in the parameters in the Crystal Ball fits to the reconstructed mass line shape from embedding (see Sec. 6.6.1) are used to calculate the systematic effect from imprecise determination of the line shape. We varied each of the free line shape parameters within their measured errors, refit the signal, and extracted the yield. We took the extremes of the fit results as the systematic uncertainties listed in Tab. 6.5.

6.7.5.2. *Smearing from TPC Misalignment.* As mentioned in Sec. 6.6.1, due to a TPC calibration error, the $d+\mathrm{Au}$ and $\mathrm{Au}+\mathrm{Au}$ datasets have an additional mass smearing of 0.2 GeV/c^2 RMS. There is an uncertainty of $\pm$0.03 GeV/c^2 in the measured smearing. To account for the uncertainy from this, we refit the parameters of the Crystal Ball functions after varying the smearing parameter from 0.17 GeV/c^2 to 0.23 GeV/c^2 and then refit and extract the signals. The fractional errors were taken as a systematic in Tab. 6.5.

6.7.5.3. *Change in Efficiency.* In the $d+\mathrm{Au}$ and $\mathrm{Au}+\mathrm{Au}$ fits, the yield of the Υ(2S) and Υ(3S) were allowed to float relative to the Υ(1S). Due to triggering threshold, the heavier excited states have a higher detection efficiency than the ground state. Since we combine the signals from Υ(1S). Υ(2S), and Υ(3S), when the excited state yields are suppressed relative to the Υ(1S), as in the $d+\mathrm{Au}$ and $\mathrm{Au}+\mathrm{Au}$ systems, the weighted efficiency to detect Υ(1S+2S+3S) decreases. We varied the relative yield of excited state to the ground state within fit errors and recalculated the total Υ(1S+2S+3S) efficiency.

By the same logic, the purity of the Υ(1S) varies as the yield of excited states changes. We again varied the relative yield of the excited states and recalculated the purity of the Υ(1S) measurement. This systematic only affects the Υ(1S) yield and R_{AA}(1S).

Source	Estimation Procedure	σ (Relative) Uncertainty
Luminosity, Vernier Scan(pp)	BBC NSD cross-section [**118**, **132**–**134**]	$\pm 7\%$
BBC efficiency	pp NSD event generator, PYTHIA vs. HERWIG [**132**]	$\pm$ 9%
ZDC-Au trig. effic. ($d+$Au)	Comparison to Glauber [**6**]	$\pm 3\%$
Vertex finding effic. ($p+p$)	Vertexing for BTOW triggers [**135**]	$\pm 1\%$
Vertex finding effic. ($d+$Au)	Minbias dAu events w/o vertex, unc. [**6**]	$\pm 0.1\%$
Vertex finding effic. (Au + Au)	NPE18 Events w/o vertex	$\pm 0.1\%$
$d+$Au minbias σ	Glauber [**6**]	$0.09/2.21 = 4\%$
$d+$Au $\langle N_{bin} \rangle$	Glauber [**6**]	$0.4/7.5 = 5.3\%$
For R_{dAu}, T_{AA} uncertainty	Vary σ_{pp}, redo $\langle N_{bin} \rangle$, see variation in T_{AA}	$+0.9\%, -0.5\%$
Acceptance	Masked towers and Polarization	$+1.7\%, -3.0\%$
L0 ADC Threshold	L0 HT thresold $\pm$ 9 ADC	$+8.7\%, -2.3\%$
L2 E_{cluster}	L2 E_{cluster} thres. $\pm$ 0.71%	$+1.2\%, -0.6\%$
L2 $\cos\theta$ cut	$\theta \pm$ 0.05	$\sim 0\%$
L2 mass cut	L2 mass threshold $\pm$500 MeV	$\sim 0\%$
Tracking Efficiency	STAR embedding, hit reconstruction	$\pm 2 \times 5.88\%$
R_{MATCH} cut Efficiency	R_{MATCH} threshold $\pm$ 0.008	+0.2%, -1.1%
E/p cut Efficiency	Vary μ and σ of E/p fit	$\pm 3\%$
$n\sigma_e$ cut efficiency	Vary μ, σ of e^- Gaussian within uncertainty	$\pm 2 \times 2.2\%$
$d+$Au, Au + Au excited state ratio	Take ratio from data, recalculate efficiency	$^{+0}_{-2}\%$ ($d+$Au), $^{+1}_{-2}\%$ (Au + Au)
Υ $p+p$ Line shape	Vary line shape parameters within fit errors.	$+6.0\%, -4.1\%$
Υ $d+$Au Line shape	Vary line shape parameters within fit errors.	$+1.8\%, -1.2\%$
Υ Au + Au Line shape	Vary line shape parameters within fit errors.	$+0.8\%, -0.9\%$
Υ p_T shape	Vary T, from 1.0 to 1.3 (nominal value: $T = 1.13$)	$\pm 1.7\%$
Υ(1S) purity, $d+$Au, Au + Au	Vary suppression of excited states	+0%, -7.5%
Total syst., σ_{pp}		$+21.1\%, -19.0\%$
Total syst., σ_{dAu}		$+17.5\%, -15.6\%$
Total syst., σ_{AuAu}		$+16.0\%, -14.1\%$
Common Normalization syst.		$+12.9\%, -12.2\%$
R_{dAu}, syst.		$+3.5\%, -3.8\%$
R_{dAu} (1S), syst.		$+3.5\%, -8.4\%$
R_{AA}, syst.		$+3.2\%, -3.6\%$
R_{AA} (1S), syst.		$+3.2\%, -8.3\%$

TABLE 6.5. Systematic uncertainties affecting the cross section.

CHAPTER 7

Results

7.1. Yields and Cross Sections

The yields were extracted using the methods described in Sec. 6.6.3. Fits are show in Figs. 6.17, 6.18, and 6.19. Yields are shown in Tab. 7.1. The error shown comes from a combination of the statistics and the fit. We calculate the measured error with the following formula:

$$\sigma_{\rm meas} = N_{\rm meas} \times \frac{\sigma_{Fit}}{N_{Fit}}$$

The yield is transformed into a differential cross section as follows:

$$\frac{d\sigma_\Upsilon}{dy} \times B_{ee} = N_{\rm meas}/\epsilon/a_{\rm det}/\Delta y$$

where $N_{\rm meas}$ is the number of measured Υ, ϵ is the product of all efficiencies (e.g. EID, triggering, mass cut, etc.), $a_{\rm det}$. is the geometrical acceptance of the detector, and Δy is the rapidity window. Measured yields and cross sections for all systems, rapidities, and centralities are summarized in Tab. 7.1.

By combing the midrapidity and forward rapidity measurements in $p+p$ and $d+$Au, we can calculate production cross sections for the range $|y| < 1.0$. In $p+p$, the cross section for Υ(1S+2S+3S) production was found to be $B_{ee} \times d\sigma/dy|_{|y|<1} = 61 \pm 8({\rm stat.} + {\rm fit})^{+13}_{-12}({\rm syst.})$ pb. The cross section in $d+$Au collisions is found to be $B_{ee} \times d\sigma/dy|_{|y|<1} = 19 \pm 3({\rm stat.} + {\rm fit}) \pm 3({\rm syst.})$ nb.

We compare our Υ(1S+2S+3S) production measurement to the global Υ(1S+2S+3S) dataset as a function of $\sqrt{s_{NN}}$ in Fig. 7.1. We show the results from multiple $p+p$ and $p+\bar{p}$ experiments that have measured $\Upsilon \to l^+l^-$ production covering a vast range of $\sqrt{s}$, from the edge of the production threshold to the current energy frontier [**24**–**34**]. As can be seen from visual inspection, our result (red star) follows the global trend. The blue curve is a next-to-leading order color evaporation model calculation done by R. Vogt [**37**]. Only

System	Centrality	States	Rapidity	Counts	$d\sigma/dy \times B_{ee}$
$p+p$	Min. Bias	1S+2S+3S	$\|y_\Upsilon\|$ <0.5	152.0 ± 23.0	64.4 $\pm 9.7^{+13.6}_{-12.2}$ pb
			0.5 < $\|y_\Upsilon\|$ < 1.0	68.0 ± 14.0	57.5 $\pm 12.1^{+12.1}_{-10.9}$ pb
		1S	$\|y_\Upsilon\|$ <0.5	99.9 ± 15.0	42.2 $\pm 6.3^{+8.9}_{-9.4}$ pb
			0.5 < $\|y_\Upsilon\|$ < 1.0	52.9 ± 11.1	44.6 $\pm 9.4^{+9.4}_{-10.0}$ pb
$d+$Au	Min. Bias	1S+2S+3S	-1.0< y_Υ <-0.5	17.7 ± 8.0	19.0 $\pm 9.0^{+3.3}_{-3.0}$ nb
			$\|y_\Upsilon\|$ <0.5	46.0 ± 12.7	12.2 $\pm 3.4^{+2.1}_{-1.9}$ nb
			0.5 < y_Υ < 1.0	29.6 ± 6.3	32.0 $\pm 7.0^{+5.6}_{-5.0}$ nb
		1S	-1.0< y_Υ <-0.5	11.3 ± 5.1	13.0 $\pm 6.0^{+2.3}_{--2.5}$ nb
			$\|y_\Upsilon\|$ <0.5	36.0 ± 10.0	10.4 $\pm 2.9^{+1.8}_{--2.0}$ nb
			0.5 < y_Υ < 1.0	20.2 ± 4.3	23.0 $\pm 5.0^{+4.0}_{--4.4}$ nb
Au + Au	0-10%	1S+2S+3S	$\|y_\Upsilon\|$ <0.5	42 ± 4	3950 $\pm 416^{+632}_{-557}$ nb
			$\|y_\Upsilon\|$ <1.0	61 ± 16	3990 $\pm 1020^{+638}_{-563}$ nb
		1S	$\|y_\Upsilon\|$ <0.5	42 ± 4	3940 $\pm 416^{+632}_{-698}$ nb
			$\|y_\Upsilon\|$ <1.0	58 ± 15	3840 $\pm 986^{+638}_{-705}$ nb
	10-30%	1S+2S+3S	$\|y_\Upsilon\|$ <0.5	90 ± 20	3040 $\pm 676^{+486}_{-429}$ nb
			$\|y_\Upsilon\|$ <1.0	144 ± 35	3430 $\pm 827^{+549}_{-484}$ nb
		1S	$\|y_\Upsilon\|$ <0.5	72 ± 16	2450 $\pm 544^{+486}_{-537}$ nb
			$\|y_\Upsilon\|$ <1.0	133 ± 32	3180 $\pm 766^{+549}_{-606}$ nb
	30-60%	1S+2S+3S	$\|y_\Upsilon\|$ <0.5	38 ± 10	905 $\pm 225^{+145}_{-128}$ nb
			$\|y_\Upsilon\|$ <1.0	58 ± 12	950 $\pm 198^{+152}_{-134}$ nb
		1S	$\|y_\Upsilon\|$ <0.5	41 ± 10	976 $\pm 243^{+145}_{-160}$ nb
			$\|y_\Upsilon\|$ <1.0	60 ± 12	984 $\pm 205^{+152}_{-168}$ nb
	0-60%	1S+2S+3S	$\|y_\Upsilon\|$ <0.5	183 ± 30	2170 $\pm 357^{+347}_{-306}$ nb
			$\|y_\Upsilon\|$ <1.0	266 ± 30	2180 $\pm 250^{+349}_{-307}$ nb
		1S	$\|y_\Upsilon\|$ <0.5	165 ± 27	1950 $\pm 321^{+347}_{-383}$ nb
			$\|y_\Upsilon\|$ <1.0	254 ± 29	2080 $\pm 239^{+349}_{-385}$ nb

TABLE 7.1. Yield and measured cross sections.

the curve for a single choice of bottom quark mass and renormalization scale is shown for plot clarity.

The Υ(1S+2S+3S) rapidity distribution in both $p+p$ and $d+$Au is shown in Fig. 7.2. The $p+p$ measurement is shown as blue stars and the $d+$Au measurement is shown as red circles. In the $p+p$ measurement, the forward ($0.5 < y < 1.0$) and backward ($-1.0 < y < -0.5$) rapidity ranges are combined into one measurement; hence, the blue star at reverse rapidity is hollow to denote that it is not an independent measurement. The $d+$Au data points are scaled down by a factor of 1,000 so they fit on the same scale as the $p+p$ data points. PHENIX results at far forward and backward rapidities are shown as diamonds [**36**].

Calculations done using a next-to-leading order pQCD color evaporation model are shown as shaded bands [**37**]. The STAR and PHENIX $p+p$ results all undershoot the

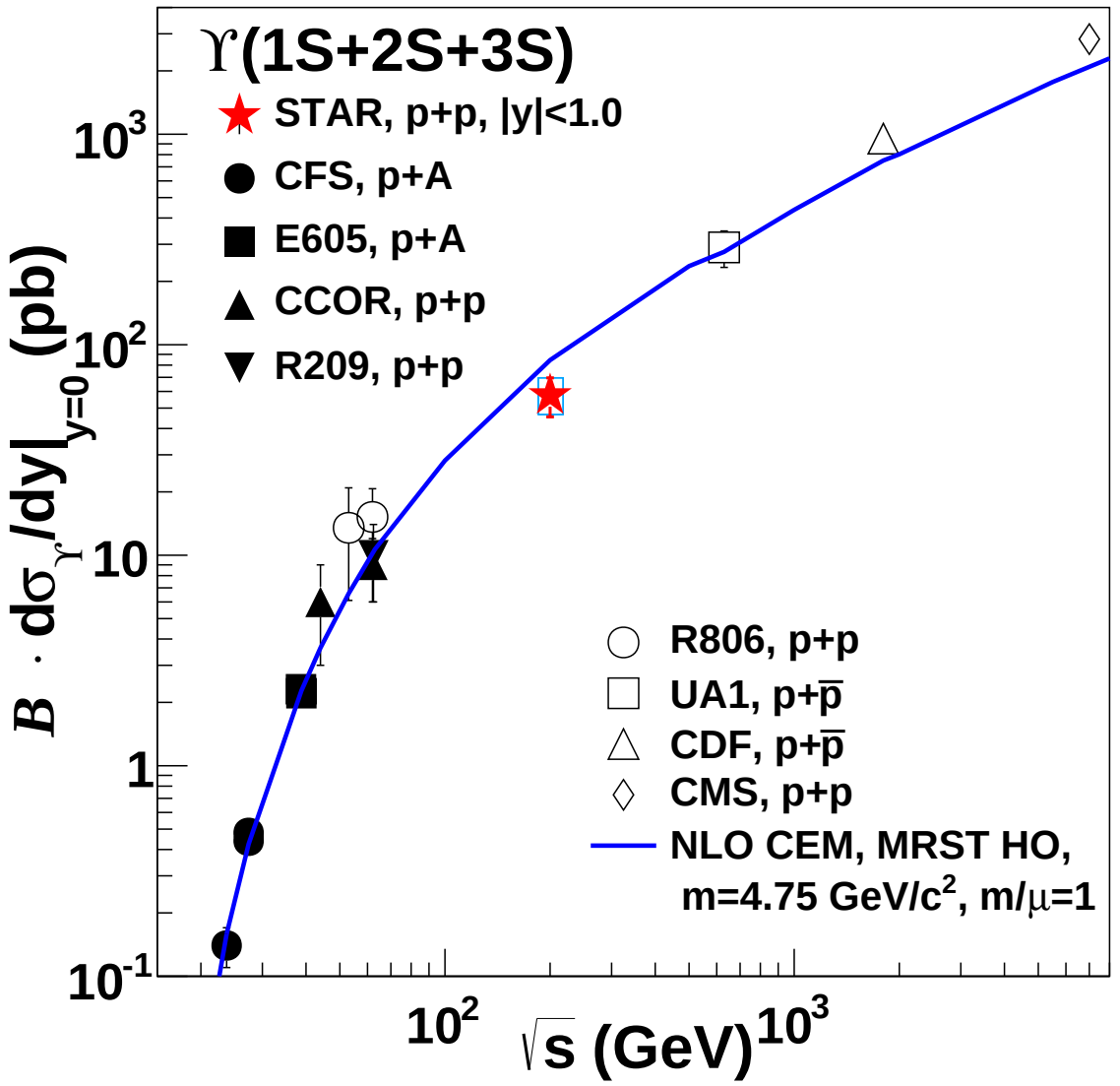

FIGURE 7.1. Comparison of our $p+p$ measurement (red star) to the global set of Υ(1S+2S+3S) production measurements [**24**–**34**]. The blue curve is a NLO Color Evaporation Model calculation of Υ(1S+2S+3S) production done by R. Vogt [**35**].

NLO CEM predictions by approximately 25%. The overall shape of the RHIC $p+p$ results follows the pQCD calculations.

The interpretation of the $d+$Au results is less straightforward. At both forward and backward rapidities, both STAR and PHENIX results are consistent with CEM predictions within errors. However, even with both statistical and systematic errors taken into account, our result for Υ(1S+2S+3S) production in $d+$Au collisions for $|y| < 0.5$ is $\sim 5\sigma$ below the

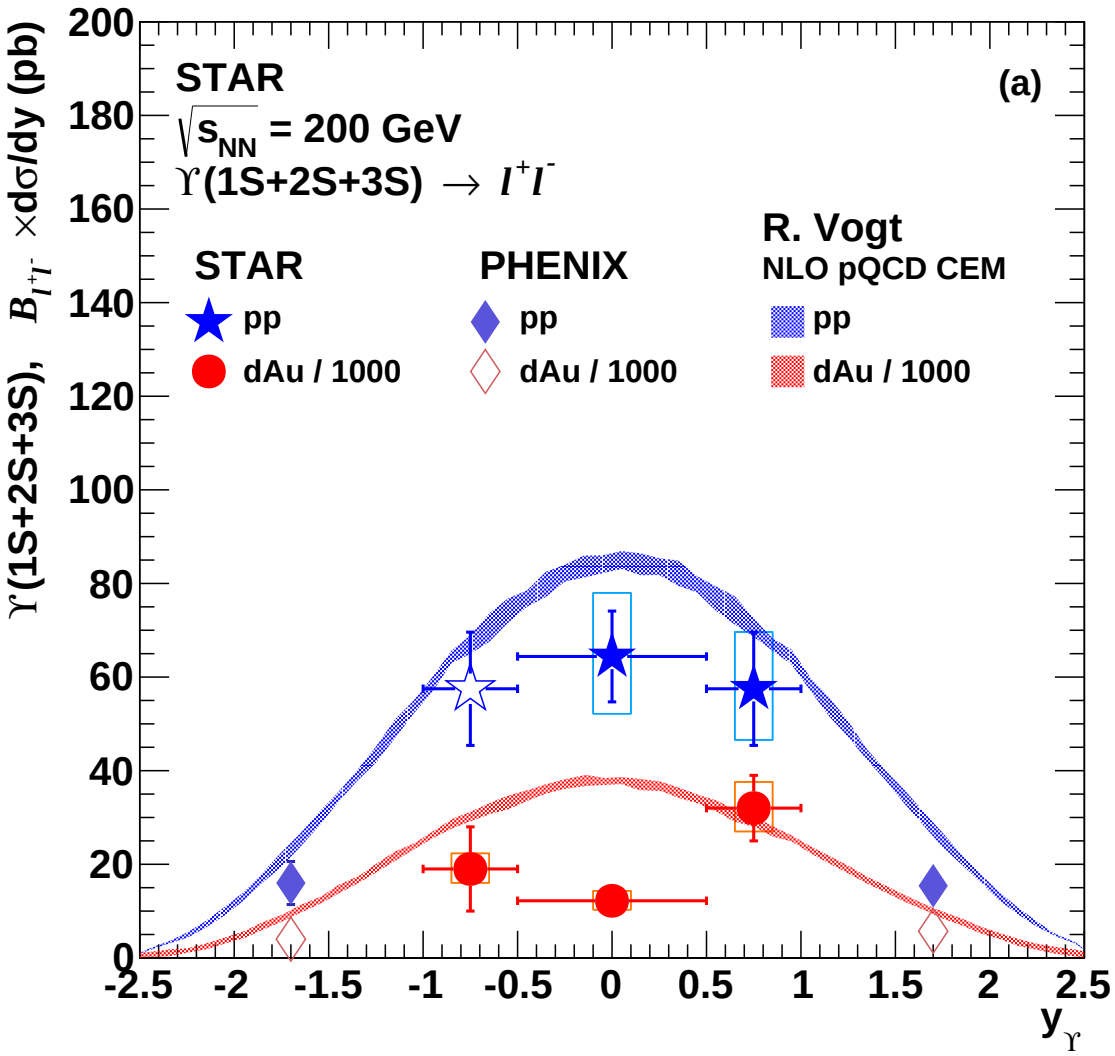

FIGURE 7.2. Υ(1S+2S+3S) production as a function of rapidity in both $p+p$ and $d+$Au collisions. The blue stars show the $p+p$ measurement with horizontal error bars denoting the width of the rapidity bins. The blue star at negative rapidity is hollow to denote that it is a reflection of the forward rapidity $p+p$measurement. The red circles show our $d+$Au measurements scaled down by a factor of 1,000 to fit on the same scale. PHENIX measurements are denoted by diamonds [**36**]. The shaded bands denote NLO pQCD CEM calculations [**37**].

pQCD prediction. As mentioned above, calculations using the same model over-predicted the yield in $p+p$. If we scale the expected yield in $d+$Au down by 25%, the discrepancy at midrapidity falls to $\sim 3\sigma$.

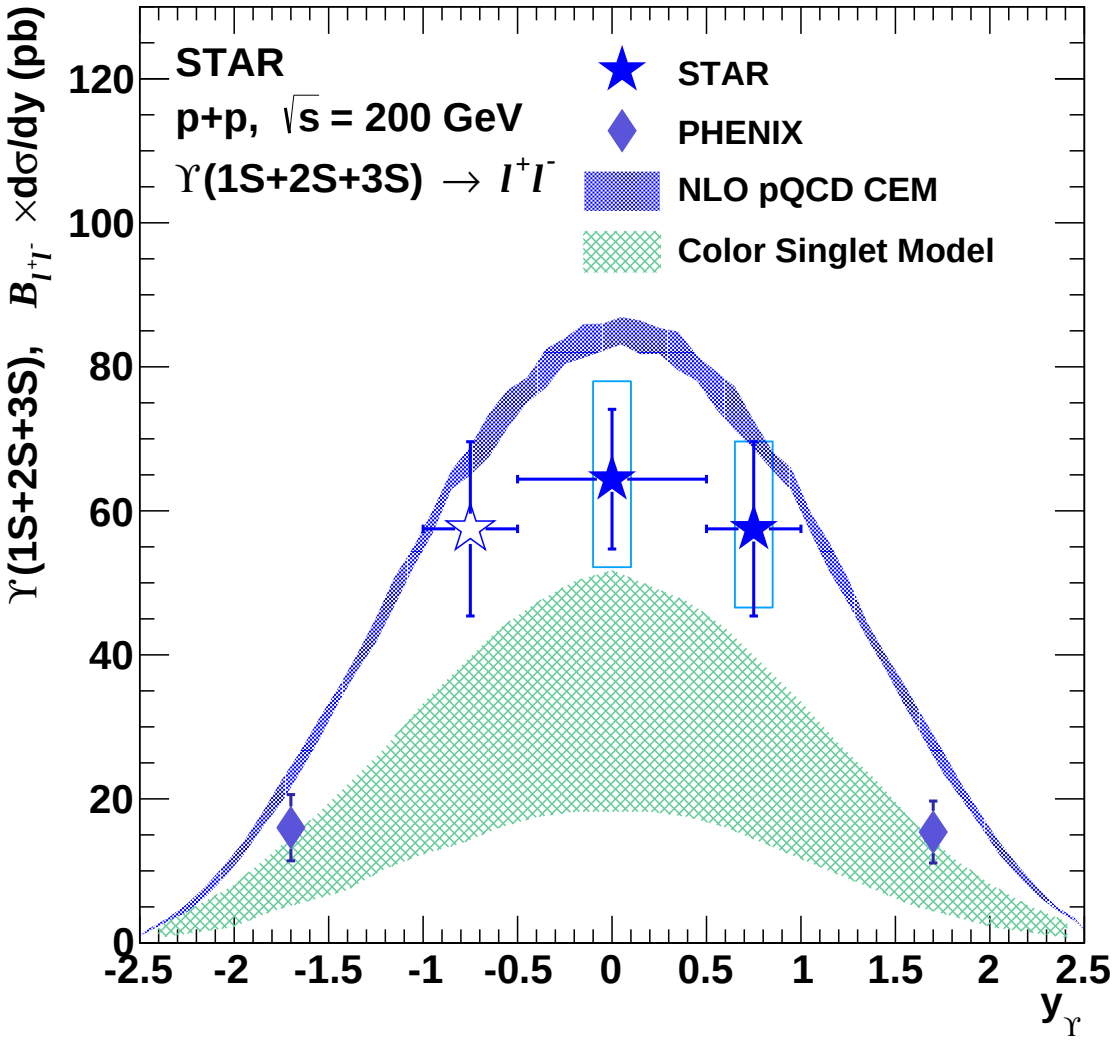

FIGURE 7.3. Υ(1S+2S+3S) production in $p+p$ collisions as a function of rapidity. STAR results are shown as blue stars and the forward-rapidity data point is reflected as in Fig. 7.2. The green hatched band shows predictions from QCD-based NLO Color Singlet Model calculations [**38**]. PHENIX measurements are denoted by diamonds [**36**]. The blue shaded band denotes NLO pQCD CEM calculations [**37**].

Alternative production cross section calculations done by Stanley Brodsky and Jean-Philippe Lansberg are shown as a green hatched band in Fig. 7.3. These calculations use a next-to-leading order Color Singlet Model [**38**]. The same CEM predictions from Fig. 7.2 are reproduced as a blue band for the sake of comparison. While disfavored by the previous

Υ measurements from STAR, it is clear from ocular inspection that neither the CEM nor CSM is favored by our $p+p$ results.

7.2. Nuclear Modification Factor

To quantify the effect of nuclear matter on particle production, we calculate the nuclear modification factor (R_{AA}, $R_{d\mathrm{Au}}$) defined as follows:

$$R_{AA} = \frac{1}{\frac{\sigma_{AA}}{\sigma_{pp}}} \times \frac{1}{\langle N_{\mathrm{coll}} \rangle} \times \frac{B_{ee} \times \left(\frac{d\sigma_{AA}}{dy}\right)^{\Upsilon}}{B_{ee} \times \left(\frac{d\sigma_{pp}}{dy}\right)^{\Upsilon}} \tag{7.1}$$

where σ_{xx} is the total nuclear inelastic cross section and $\langle N_{\mathrm{coll}} \rangle$ is the average number of binary nucleon collisions as calculated by a Glauber model [**130**]. The first term in the equation controls for the relative chance to have any nuclear collision at all. The second term accounts for the number of nuclear collisions within a typical event. The third term is the actual ratio of production rates.

R_{AA} (or $R_{d\mathrm{Au}}$ in the case of $d+\mathrm{Au}$ collisions) is a very useful and easy-to-interpret quantity. When $R_{AA} = 1$, there is no nuclear modification at all; the number of particles produced in a typical event is the same as if $< N_{\mathrm{coll}} >$ independent $p+p$ collisions were overlaid. If $R_{AA} = 0$, no particles are produced–often referred to as complete suppression. If $R_{AA} > 1$, nuclear effects have enhanced the yield of particles.

Using the 2009 $p+p$ results as the baseline, we calculated R_{AA} and $R_{d\mathrm{Au}}$ for multiple states, rapidities, and centralities. The nuclear modification factors were calculated using the following total inelastic cross sections: $\sigma_{pp} = 42$ mb, $\sigma_{d\mathrm{Au}} = 2.2$ b, and $\sigma_{\mathrm{AuAu}} = 6$ b. The results are summarized in Tab. 7.2. The reported uncertainties on our measured R_{AA} and $R_{d\mathrm{Au}}$ values are fourfold: (1) uncertainty from statistics and fitting from the $d+\mathrm{Au}$ or $\mathrm{Au}+\mathrm{Au}$ cross section; (2) statistical and fitting uncertainty from $p+p$; (3) $d+\mathrm{Au}$ or $\mathrm{Au}+\mathrm{Au}$ systematics which do not cancel with the $p+p$ measurement and are not joint to both the $d+\mathrm{Au}$ and $\mathrm{Au}+\mathrm{Au}$ measurements; and (4) systematic uncertainties from the $p+p$ measurement which do not cancel with the $d+\mathrm{Au}$ or $\mathrm{Au}+\mathrm{Au}$ measurement along with systematics joint to both the $d+\mathrm{Au}$ and $\mathrm{Au}+\mathrm{Au}$ measurements.

System	Centrality	States	Rapidity	$R_{AA,dA}$
$d+\mathrm{Au}$	Min. Bias	1S+2S+3S	-1.0< y_Υ <-0.5	$0.84 \pm 0.40 \pm 0.18 \pm 0.03 \pm 0.10$
			$\lvert y_\Upsilon\rvert$ <0.5	$0.48 \pm 0.14 \pm 0.07 \pm 0.02 \pm 0.06$
			0.5 < y_Υ < 1.0	$1.42 \pm 0.32 \pm 0.30 \pm 0.05 \pm 0.17$
			$\lvert y_\Upsilon\rvert$ <1.0	$0.79 \pm 0.14 \pm 0.10 \pm 0.03 \pm 0.09$
		1S	-1.0< y_Υ <-0.5	$0.74 \pm 0.34 \pm 0.16^{+0.03}_{-0.06} \pm 0.09$
			$\lvert y_\Upsilon\rvert$ <0.5	$0.63 \pm 0.18 \pm 0.09^{+0.02}_{-0.05} \pm 0.08$
			0.5< y_Υ <1.0	$1.31 \pm 0.29 \pm 0.28^{+0.05}_{-0.11} \pm 0.16$
			$\lvert y_\Upsilon\rvert$ <1.0	$0.83 \pm 0.15 \pm 0.11^{+0.03}_{-0.07} \pm 0.10$
$\mathrm{Au}+\mathrm{Au}$	0-10%	1S+2S+3S	$\lvert y_\Upsilon\rvert$ <0.5	$0.46 \pm 0.05 \pm 0.07 \pm 0.02 \pm 0.05$
			$\lvert y_\Upsilon\rvert$ <1.0	$0.49 \pm 0.13 \pm 0.07 \pm 0.02 \pm 0.06$
		1S	$\lvert y_\Upsilon\rvert$ <0.5	$0.69 \pm 0.05 \pm 0.10^{+0.02}_{-0.06} \pm 0.08$
			$\lvert y_\Upsilon\rvert$ <1.0	$0.66 \pm 0.13 \pm 0.10^{+0.02}_{-0.05} \pm 0.08$
	10-30%	1S+2S+3S	$\lvert y_\Upsilon\rvert$ <0.5	$0.69 \pm 0.16 \pm 0.10 \pm 0.02 \pm 0.08$
			$\lvert y_\Upsilon\rvert$ <1.0	$0.82 \pm 0.20 \pm 0.12 \pm 0.03 \pm 0.10$
		1S	$\lvert y_\Upsilon\rvert$ <0.5	$0.85 \pm 0.16 \pm 0.13^{+0.03}_{-0.07} \pm 0.10$
			$\lvert y_\Upsilon\rvert$ <1.0	$1.07 \pm 0.20 \pm 0.16^{+0.03}_{-0.09} \pm 0.13$
	30-60%	1S+2S+3S	$\lvert y_\Upsilon\rvert$ <0.5	$0.74 \pm 0.22 \pm 0.11 \pm 0.03 \pm 0.09$
			$\lvert y_\Upsilon\rvert$ <1.0	$0.82 \pm 0.22 \pm 0.12 \pm 0.03 \pm 0.10$
		1S	$\lvert y_\Upsilon\rvert$ <0.5	$1.22 \pm 0.22 \pm 0.18^{+0.04}_{-0.10} \pm 0.15$
			$\lvert y_\Upsilon\rvert$ <1.0	$1.19 \pm 0.22 \pm 0.18^{+0.04}_{-0.10} \pm 0.14$
	0-60%	1S+2S+3S	$\lvert y_\Upsilon\rvert$ <0.5	$0.62 \pm 0.11 \pm 0.09 \pm 0.02 \pm 0.07$
			$\lvert y_\Upsilon\rvert$ <1.0	$0.66 \pm 0.09 \pm 0.10 \pm 0.02 \pm 0.08$
		1S	$\lvert y_\Upsilon\rvert$ <0.5	$0.85 \pm 0.11 \pm 0.13^{+0.03}_{-0.07} \pm 0.10$
			$\lvert y_\Upsilon\rvert$ <1.0	$0.88 \pm 0.09 \pm 0.13^{+0.03}_{-0.07} \pm 0.11$

TABLE 7.2. R_{AA} and $R_{d\mathrm{Au}}$ for all measured Υ states, rapidities, and centrality bins. The results are listed in the form $a \pm b \pm c \pm d \pm e$ where a is $R_{d\mathrm{Au}}$ or R_{AA}, b is the $d+\mathrm{Au}$ or $\mathrm{Au}+\mathrm{Au}$ statistical uncertainty, c is the $p+p$ statistical uncertainty, d is the $d+\mathrm{Au}$ or $\mathrm{Au}+\mathrm{Au}$ systematic uncertainty, and e is the $p+p$ systematic uncertainty.

We show the $R_{d\mathrm{Au}}$ results for both PHENIX (green diamonds) and STAR (red stars) as a function of rapidity in Fig. 7.4. The RHIC results are compared to CEM predictions using EPS09 NLO shadowing predictions [**37**] (green band). The width of the band at highly negative rapidities is dominated by uncertainty in the magnitude of the Gluon EMC effect. Elsewhere, the bulk of the uncertainty comes from the range of individual EPS09 parameterizations. Note that this prediction actually predicts and enhancement on the order of $R_{d\mathrm{Au}} \approx 1.1$ at midrapidity whereas our results show a suppression of $R_{d\mathrm{Au}} = 0.48 \pm 0.16$ (stat.) ± 0.06 (syst.). Similar calculations using other nPDFs (EKS90, EPS09, and nDSg) also find an enhancement at midrapidity on the order of 5-20% [**137**].

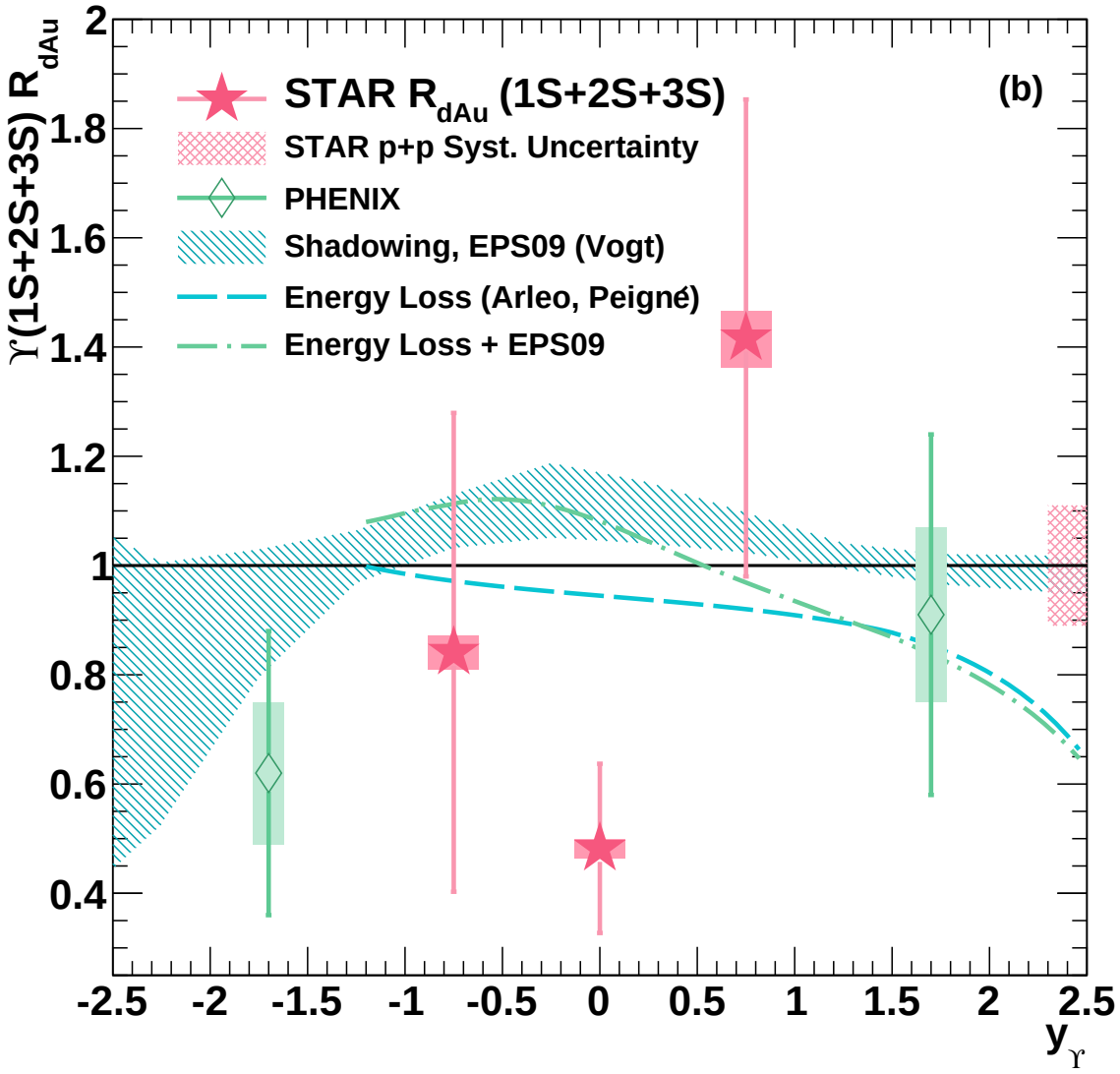

FIGURE 7.4. $R_{d\mathrm{Au}}$ as a function of rapidity. Our results are shown as red stars. PHENIX results are shown as green diamonds. The blue hatched band shows predictions based on shadowing from EPS09 done by R. Vogt. Calculations performed by F. Arleo and S. Peignè based on suppression from initial-state parton energy loss but without EPS09 are shown as a blue dashed line [**39**]. The green dot-dashed line shows the combination of energy loss and EPS09.

An alternate approach to explaining the observed Υ suppression in $d+\mathrm{Au}$ is explored in Ref. [**39**]. The authors explore the concept of final-state parton energy loss. In this model, the early $b\bar{b}$ state interacts with the cold nuclear-matter in the nucleus, causing them to undergo induced gluobremsstrahlung radiation. The lost energy in the incoming parton then decreases the likelihood of creating a heavy meson. This process is not unique to

bottomonium production and were initially applied to J/ψ production. These calculations do not include suppression from nuclear absorption (also known as break-up). Furthermore, these calculations are only valid for the range $y \sim< 1.2$ in which the initial-state partons are close to the frame of the Au nucleus. The prediction based on energy loss alone is shown as a dashed blue curve in Fig. 7.4. When effects from shadowing as parameterized by EPS09 are included, a slight enhancement is predicted ad midrapidity as shown by the dot-dashed green curve. STAR and PHENIX results are in agreement with all three calculations except for the point at $|y| < 0.5$. Hence, the suppression at midrapidity is indicative of suppression effects beyond shadowing and initial-state parton energy loss.

However, despite not being predicted by any of the models, this level of suppression of Υ production in $p(d)$+A collisions has been seen before. Measurements done by the E772 collaboration at Fermilab studied Υ production in fixed-target p+A collisions with a 800 GeV proton beam [**40**]. This roughly translates to a center-of-mass energy of $\sqrt{s_{NN}}$=40 GeV. Multiple ion targets covering a wide range of A were used: Carbon, Calcium, Iron, and Tungsten (see Fig. 7.5(a)). The E772 collaboration used a deuterium target to measure baseline $p + d$ collisions.

In Fig. 7.5(a), we show the E772 results for both Υ(1S)(circles) and Υ(2S+3S) (squares) as a function of mass number (A). Our Υ(1S) result is shown as a red star with systematic uncertainty shown as red box. There is a notable suppression of both Υ(1S) and Υ(2S+3S) in all systems. The gray line denotes the model used by E772, where $\sigma_{pA} = A^{\alpha}\sigma_{pp}$. A fit to the E772 data gives $\alpha = 0.962 \pm 0.006$. Substituting into our definition of $R_{d\mathrm{Au}}$ and dividing our yield by a factor of two to account for the fact that we measure d+A collisions instead of p+A collisions, we can relate α to $R_{d\mathrm{Au}}$:

$$R_{d\mathrm{Au}} = \frac{2}{\langle N_{bin} \rangle} \frac{\sigma_{pp}}{\sigma_{dA}} A^{\alpha} \tag{7.2}$$

As can be seen by eye, the STAR result is in strong agreement with this scaling. However, given the size of the statistical and systematic uncertainties on all measurements, one could easily fit the data with a constant of $\alpha \approx 0.9$. When Au is the ion in question, a value of α=0.9 implies a nuclear modification factor of $R_{d\mathrm{Au}}$=0.59.

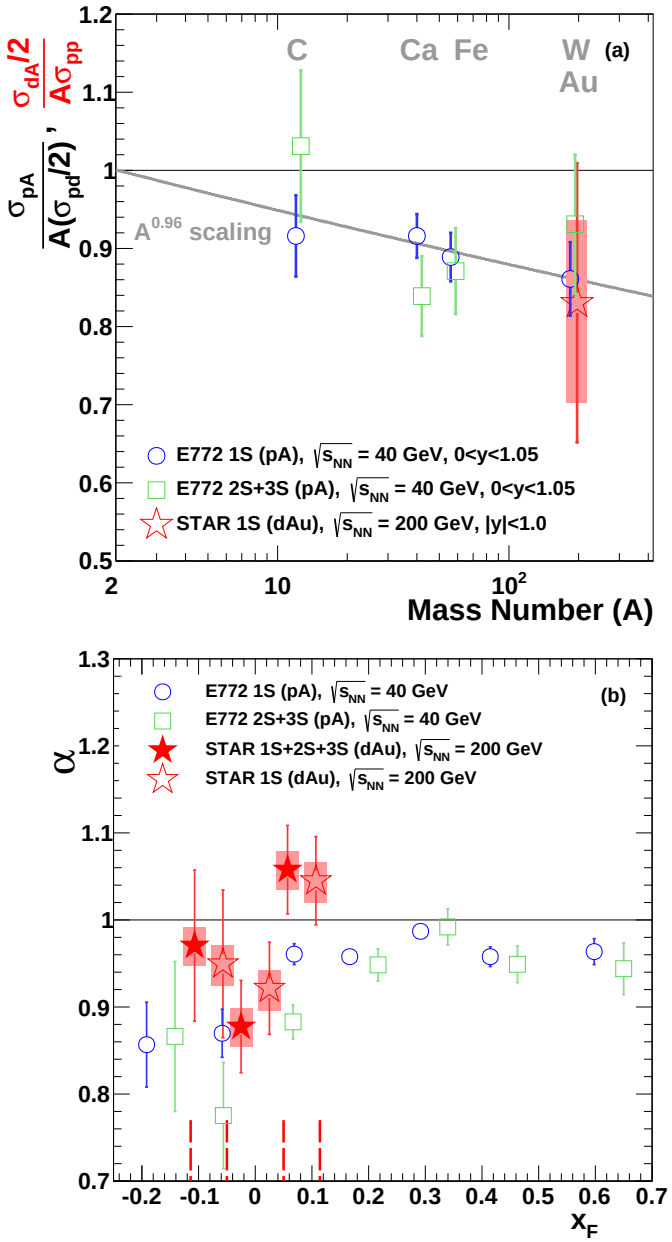

FIGURE 7.5. Comparison of our d + Au results to the p+A results of E772 [**40**]. (a): Ratio of Υ production in $p(d)$+A to production in p+$d(p)$ as a function of the ion mass number. E772 results are shown as blue circles (Υ(1S)) and green squares (Υ(2S+3S)). Our result for Υ(1S) is shown as a red star. The gray line denotes the model used by E772 where $\sigma_{pA} = A^{\alpha}\sigma_{pp}$. (b): Suppression exponent α as a function of Feynman-x. The vertical dashed lines at the bottom denote the estimated bin widths of our measurements. Note that the results are offset in x_F for clarity.

Figure 7.5(b) shows the measured suppression exponent, α, as a function of Feynman-x for both E772 and STAR using the same color scheme as Fig. 7.5(a). The dashed red lines at the bottom denote the estimated width of our measurement bins in x_F. To calculate x_F from rapidity, we begin with their definitions:

$$y = \frac{1}{2} \ln \frac{E + p_z}{E - p_z} \tag{7.3}$$

$$x_F = \frac{p_z}{p_z(\text{max.})} \tag{7.4}$$

Noting that $E^2 = m^2 + p^2 = m^2 + p_z^2 + {p_T}^2$, we can solve for p_z as a function of y:

$$p_z = \sqrt{m^2 + {p_T}^2} \sinh(y) \tag{7.5}$$

To obtain x_F, we need two additional pieces of information: p_T and p_z(max.). Knowing that the beam momentum is nearly 100 GeV/c and using the mass of the upsilon, we obtain p_z(max.) = 99.6 GeV/c. Furthermore, from previous studies [**8**] and estimates of the p_T spectrum from interpolation (see Sec. 6.3), we find that the average p_T of an Υ produced at RHIC energies is around 1 GeV/c. Given this information, it is trivial to calculate the x_F for any given rapidity.

The STAR midrapidity Υ(1S) and Υ(1S+2S+3S) results are consistent with both the Υ(1S) and Υ(2S+3S) measurements made by E772 around $x_F \sim 0$. That Υ suppression in CNM has been seen by both STAR and E772 is intriguing and warrants further studies of sources of enhanced suppression at midrapidity. However, this is the first measurement of Υ production in the presence of cold nuclear matter at midrapidity at RHIC energies. Given the size of our statistical errors, future $d + A$, $p + A$, or even ^{3}He+A studies would be very useful to shrink our errors and to extend our measurements to a higher p_T range to see if the effect persists in different kinematic regimes.

The nuclear modification factor as a function of N_{part} is shown in Fig. 7.6. We show the measured suppression of Υ in both d + Au (green square) and Au + Au (black circles). The hollow circle denotes the centrality-integrated (0-60%) Au + Au measurement. Also shown for comparison in Fig. 7.6 is the measured R_{AA} in U + U collisions [**138**]. Systematic uncertainties are shown as shaded boxes around the central values. The dotted blue box

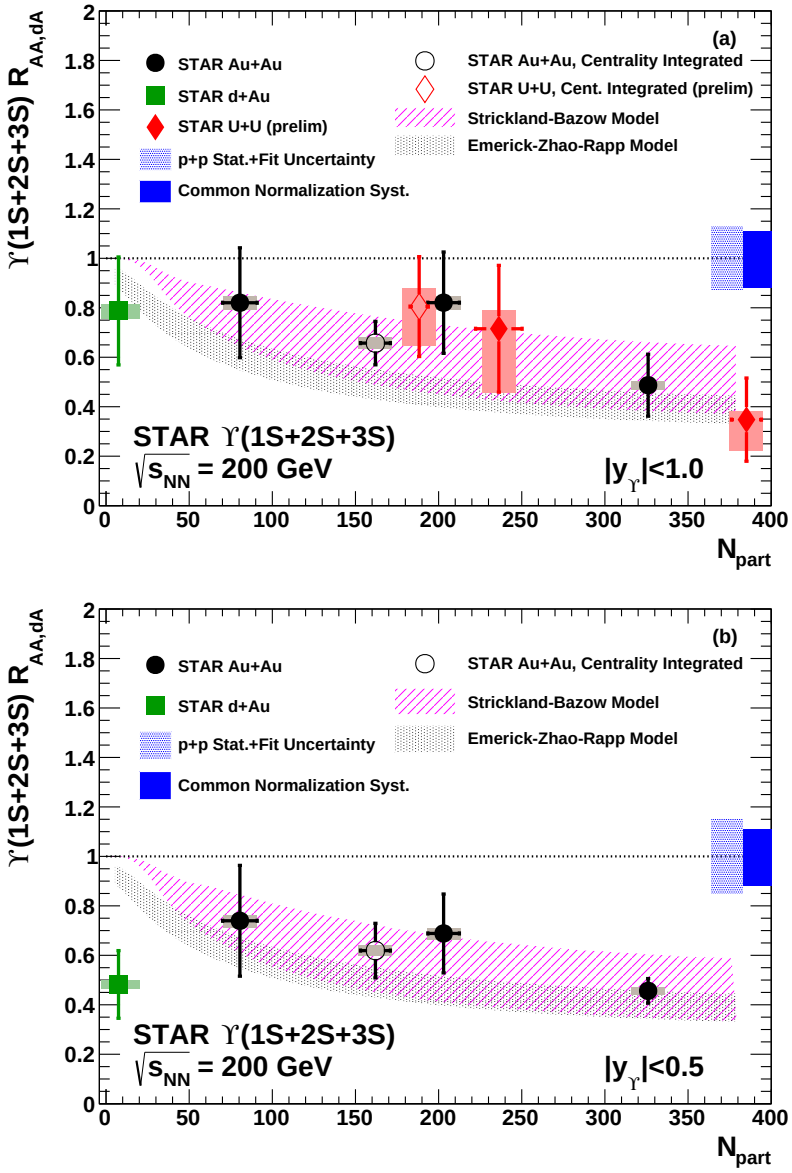

FIGURE 7.6. Υ(1S+2S+3S) R_{AA} as a function of $N_{\rm part}$. Figure (a) shows R_{AA} for $|y| < 1.0$ whereas Figure (b) shows the same for $|y| < 0.5$. The R_{AA} in Au + Au collisions is shown as black circles; the filled circles are split by centrality and the hollow circle is the centrality integrated result. $R_{d\rm Au}$ is shown as a green square. The shaded blue box around one denotes the statistical uncertainty of the $p + p$ measurement. The solid blue box shows systematics joint to all d + Au and Au + Au results. For $|y| < 1.0$ (Fig. (a)), we also show R_{AA} as measured in U + U collisions as red diamonds. The magenta band shows the predicted R_{AA} from calculations by Strickland and Bazow [**41**]. Predictions by Zhao and Rapp are in gray [**42**].

shows the statistical and fit uncertainty in the $p+p$ measurement, which is common to all R_{AA} measurements. The solid blue box shows the systematic uncertainty joint to the $d+\mathrm{Au}$ and $\mathrm{Au}+\mathrm{Au}$ measurements.

In $\mathrm{Au}+\mathrm{Au}$, we see a clear trend of greater suppression with increasing N_{part}, as expected. Our results for $R_{d\mathrm{Au}}$ paint a less clear picture. For the range $|y| < 1.0$, the suppression in $d+\mathrm{Au}$ is comparable to peripheral $\mathrm{Au}+\mathrm{Au}$, which is expected if peripheral collisions do not create a QGP of great enough temperature to dissociate Υ, leaving us solely with effects from CNM. At midrapidity ($|y| < 0.5$), the suppression in $d+\mathrm{Au}$ is greater than in peripheral or mid-central collisions (though within the lower bound of errors), and is at the same level of suppression as central $\mathrm{Au}+\mathrm{Au}$ collisions. This behavior is unexpected by all current models. While it could be a statistical fluctuation, similar suppression was seen at midrapidity in p+W collisions by E772, making timely future analyses of Υ production in the presence of CNM prudent.

Theoretical predictions by M. Strickland and D. Bazow are shown in magenta [**41**]. These calculation seek to incorporate lattice-QCD results, which reflect such effects as screening of the bottomonium potential, broadening of the line shape, and correctly modeling the dynamic propagation of the Υ meson through the colored medium with a bulk, time-evolving, hydrodynamic model. This model assumes a hydrodynamically expanding fireball with a temperature profile that falls off with time as the plasma expands and cools. Feed-down from higher bottomonium states [**139**] is taken into account. This model uses the internal energy of the bottomonium state as the heavy-quark binding potential. The internal energy is the energy required to create a new system in a vacuum whereas the aforementioned free energy takes into account the energy available from spontaneous heat transfer from a local thermal bath. Unfortunately, this model does not take into account sources of suppression from CNM effects beyond modification of the nPDF. The authors vary the viscosity-to-entropy ratio, η/S, in the range $[1/4\pi, 3/4\pi]$, while keeping particle production at midrapidity constant. To achieve this, the initial temperature at the center of the QGP was also varied in the range 428-442 MeV. Our results for all three nuclear systems reflect the predictions very well for $|y| < 0.5$. When we examine the smaller range

of $|y| < 0.5$ on the other hand, we see that the model again predicts the Au + Au results well, but fails to predict the suppression seen in d + Au.

The gray band shows the results of calculations by A. Emerick, X. Zhao, and R. Rapp (EZR) [**42**]. In this lattice-QCD-based model, pre-bottomonium states interact with hard gluons in the colored medium, causing them to dissociate before they can finish hadronizing into fully-fledged mesons. The initial temperature in this model is 330 MeV. Unlike the Strickland model, EZR does contain CNM effects beyond modified nPDFs. This model contains a cross section for nuclear absorption of bottomonium which is varied in the range 0-3 mb (as denoted by the width of the band). This absorption cross section can account for an R_{AA} as low as ~ 0.7 in central Au + Au collisions. The additional suppression needed to bring the R_{AA} down to ~ 0.5 all comes from QGP effects. As with the Strickland model, our results are in good agreement with the predictions except for $R_{d\mathrm{Au}}$ at $|y| < 0.5$.

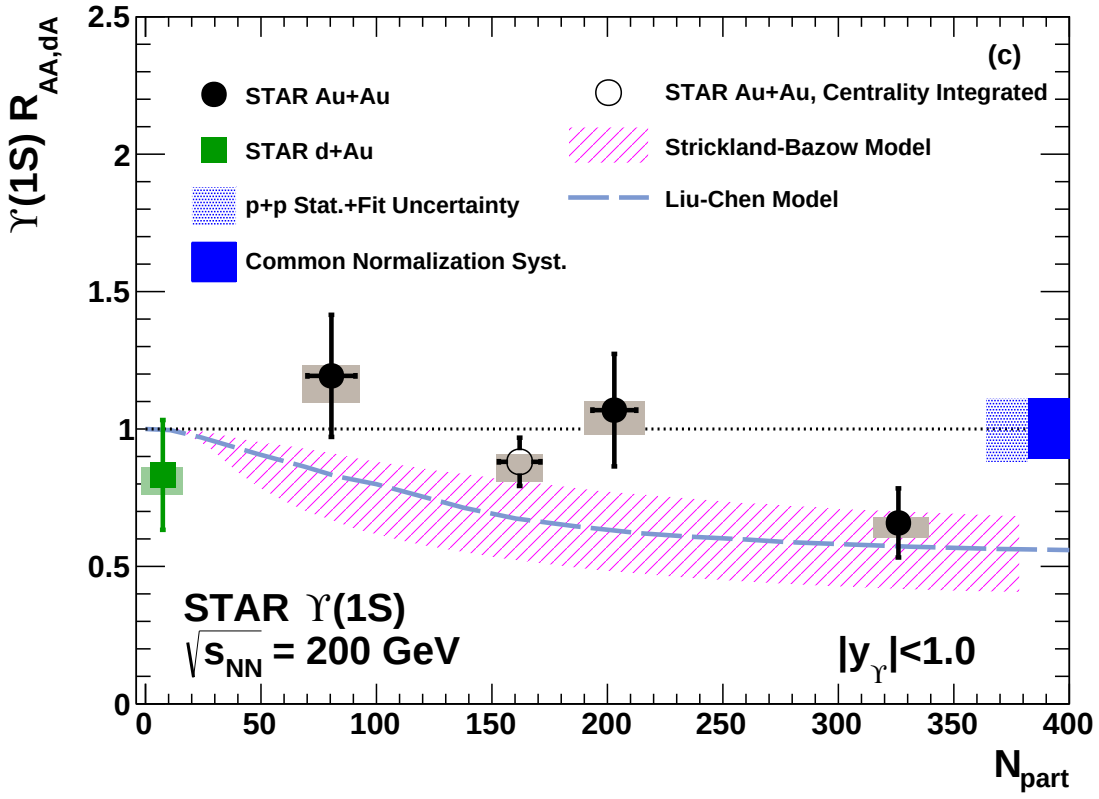

FIGURE 7.7. Υ(1S) suppression as a function of N_{part}. Calculations of Υ(1S) suppression by Liu et al. are shown as the dashed blue line [**43**].

In Fig. 7.7, we show the R_{AA} for the Υ(1S) alone. As expected due to the strong binding energy of the Υ(1S), R_{AA}(1S) is consistent with one for all systems except the most-central Au + Au events. This behavior indicates that we only reach temperatures hot enough to affect the Υ(1S) in 0-10% central Au + Au collisions. Most of this suppression, though, is likely due to suppression of excited bottomonium states which would have fed down to the Υ(1S). Measurements performed by CDF at high p_T($p_T > 8$ GeV/c) find onlt 51% of Υ(1S) to be direct; the other 49% come from Υ(2S), Υ(3S), and χ_b decays [**139**]. Recent measurement by LHCb of feed-down from the χ_b(1P) to Υ(1S) are in strong agreement with these results [**140**]. An R_{AA} for the Υ(1S) of 0.51 or greater could hence be due solely to excited state suppression without any suppression of directly produced Υ(1S).

As before, we compare to calculations by Strickland and Bazow shown in magenta. These calculations follow the same procedure as described above, but predict R_{AA}(1S) instead of R_{AA}(1S+2S+3S). The model slightly underpredicts the suppression in 10-30% and 30-60% centralities. However, once you fold in the $p + p$ uncertainties, both results are within 1σ of the predictions.

Also shown as a dashed blue line is a prediction by Liu et al. [**43**]. This model again uses the internal energy as the binding potential and includes feed-down. The initial temperature of the fireball is 340 MeV, which lattice-QCD results indicate should not be hot enough to directly dissociate the Υ(1S). Hence, all suppression of the inclusive Υ(1S) is due to dissociation of higher states before it in the decay chain. Though assumed to be small in magnitude, the Liu et al. calculations do not include any CNM effects.

Fig. 7.8 shows a summary of quarkonium results from STAR. The Υ(2S+3S) results are reported as a 95% upper limit. The horizontal bar on the limit spans from the binding energy of the Υ(3S) to that of the Υ(2S); the arrow is placed at the weighted average of their $p + p$ yields as calculated in Sec. 6.6.2. Suppression of J/ψ is shown as a blue diamond (see Ref. [**44**]). We show the results for high-p_T J/ψ here since they have a similar Q^2 to Υ mesons. As expected, we see greater suppression of the lightly bound Υ(2S+3S) states compared to the more tightly bound J/ψ and Υ(1S).

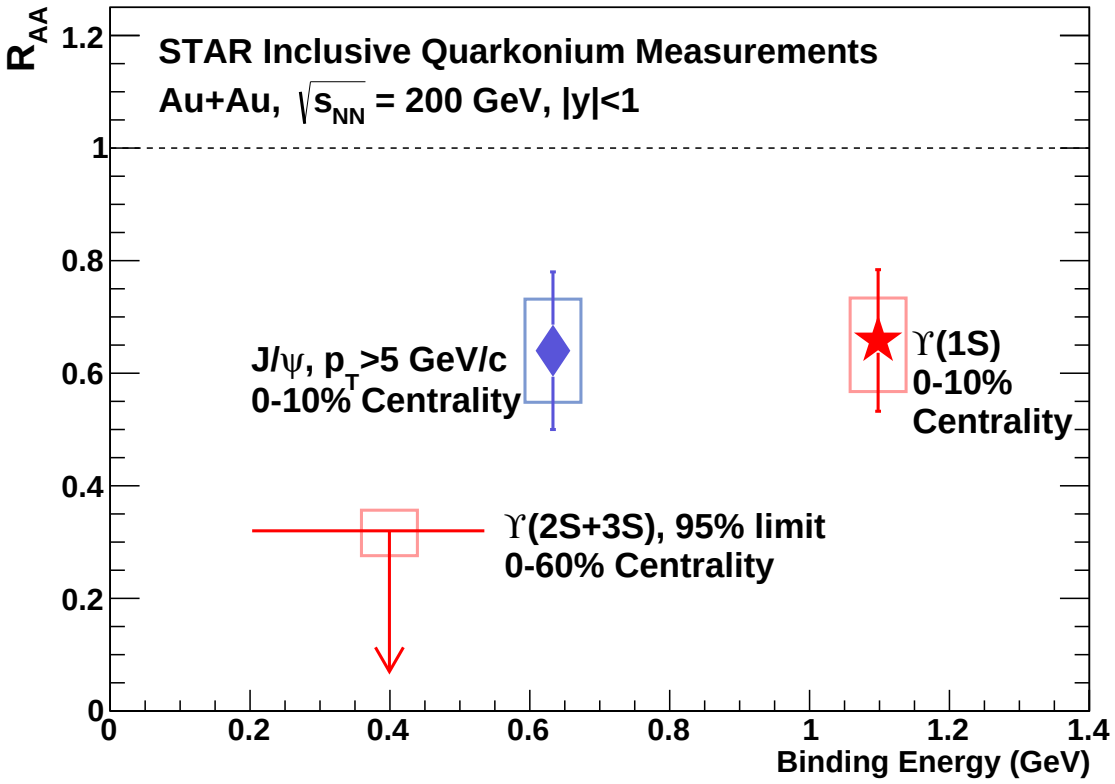

FIGURE 7.8. Nuclear Modification Factor of heavy quarkonia as measured by STAR as a function of binding energy. The high-p_T J/ψ results are from [**44**]. The width of the Υ(2S+3S) upper limit spans the range between their two biding energies. The arrow is placed at the weighted average of their binding energies.

7.3. Comparison to Model-Based Psuedoexperiments

In order to help interpret our results and explore the many possible sources of suppression, we implemented Monte Carlo pseudoexperiments modeling Υ production rates. For each run, we simulated the number of Υ(1S+2S+3S) measured in $p+p$, $d+$Au, and all Au + Au centralities. Υ were generated in each system by a Poisson process whose expected value is chosen based on the scenarios described below. The simulated $p+p$ baseline was used in combination with the simulated results from each of the other collision systems to calculate an R_{AA} or $R_{d\mathrm{Au}}$. The overall level of simulated statistics was chosen to reflect the statistics of our datasets. This allows us to estimate the statistical significance of our measurements from simulations. The simulation was performed for both measured rapidity ranges ($|y| < 0.5$ and $|y| < 1.0$).

Four different scenarios were explored: (1) no CNM or QGP suppression of Υ mesons; (2) only suppression from CNM effects; (3) only suppression from QGP effects; and (4) both CNM and QGP suppression. In the first scenario, all systems are simulated assuming unmodified binary scaling. In the second scenario, the CNM suppression parameterization measured by E772 (A^{α}) was used with their measured exponent of $\alpha = 0.962 \pm 0.006$ [**40**]. Production was simply scaled by A^{α} in the $d + \mathrm{Au}$ simulation and scaled by $A^{2\alpha}$ in $\mathrm{Au} + \mathrm{Au}$ simulations to account for the combined effects of the modification of the nuclear PDFs in both projectiles as well as other sources of suppression. To account for uncertainty in the exponent, a new α was drawn for each simulation from a Gaussian distribution centered at 0.962 and with a width of 0.006. In the third scenario, we model QGP suppression using the calculations by Strickland and Bazow discussed previously [**41**]. Suppression for each centrality in the $\mathrm{Au} + \mathrm{Au}$ simulations is chosen based on N_{part}; there is no suppression in the $d + \mathrm{Au}$ simulations. Since the viscosity of the QGP created at RHIC is still an unknown quantity, a different viscosity is selected for each simulation based on a flat prior in the range $\eta/S \in [1/4\pi, 3/4\pi]$ (see the height of the theory bands in Fig. 7.6). In the final scenario, we combine the effects described in the second and third scenarios. This approach assumes that suppression from QGP and CNM effects factorize. Both α and η/S are varied independently for each run.

We ran 10 million pseudoexperiments for each scenario and rapidity range. The results are shown in Figs. 7.9-7.12. The upper four plots of each figure show the results for $|y| < 0.5$ and the lower plots show the wider range $|y| < 1.0$. The histograms show the number of experiments which resulted in each nuclear modification factor. Our results are shown as a red line and the systematic uncertainties are shown as a pink box. The p-value of our result for the given system and scenario is displayed at the top. The p-values of the upper and lower limits of our systematic uncertainties are displayed afterwards. The statistical uncertainties of our measurements are not shown since that is what we are trying to assess through this pseudoexperiment study.

We first look at the results of the 'no suppression' scenario (shown in Fig. 7.9). All eight results disfavor this scenario, though with different statistical strengths. Our peripheral $\mathrm{Au} + \mathrm{Au}$, $|y| < 1.0$ results only disfavor this result with a p-value of 0.098 (about 1.3σ).

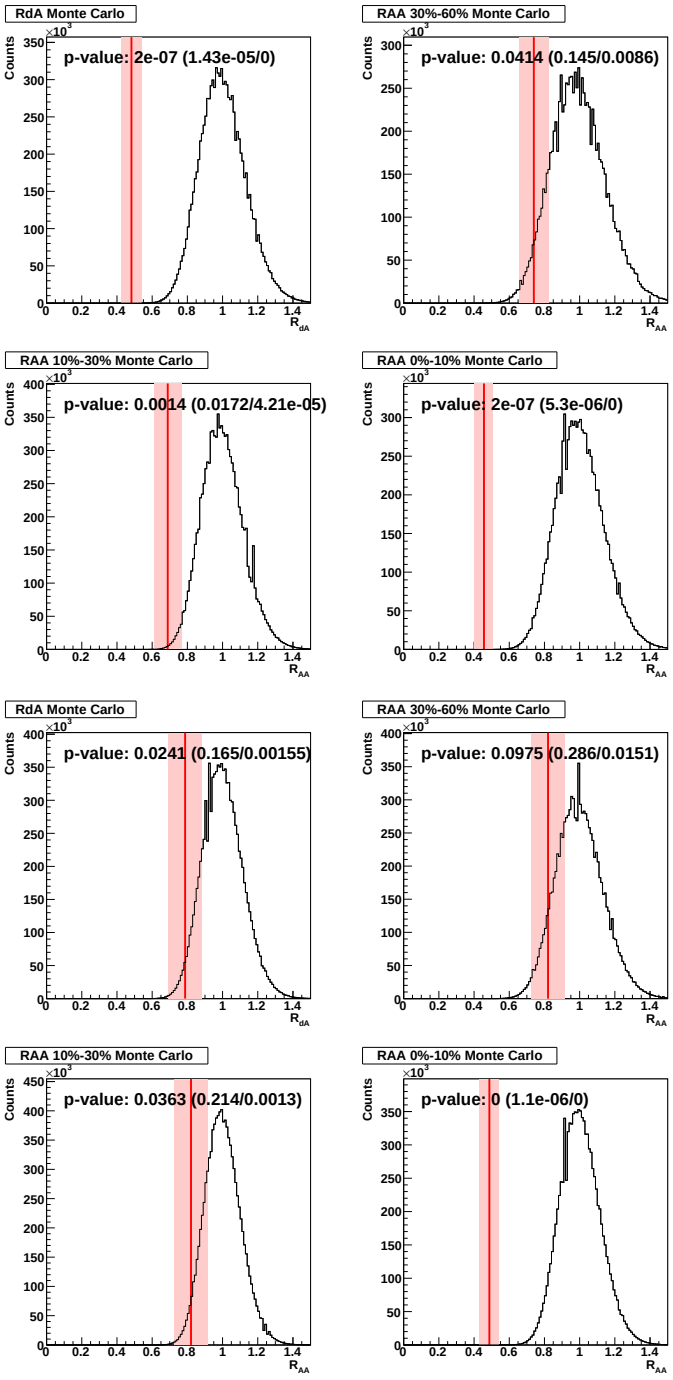

FIGURE 7.9. Summary of simulation results assuming no suppression (scenario 1). The upper plots show the results for $|y| < 0.5$ and the lower plots show $|y| < 1.0$. The red lines denote our results and the pinks bands show systematics uncertainties.

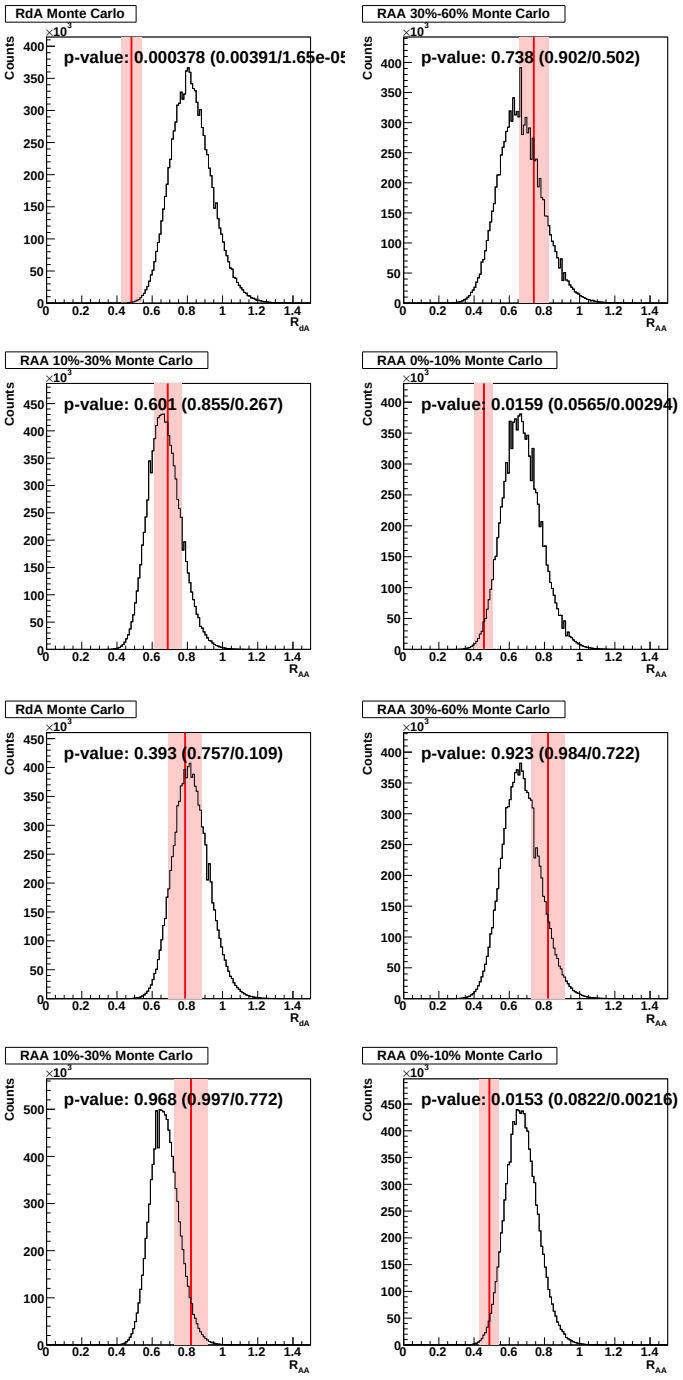

FIGURE 7.10. Summary of simulation results assuming suppression from CNM effects only (scenario 2). The upper plots show the results for $|y| < 0.5$ and the lower plots show $|y| < 1.0$. The red lines denote our results and the pinks bands show systematics uncertainties.

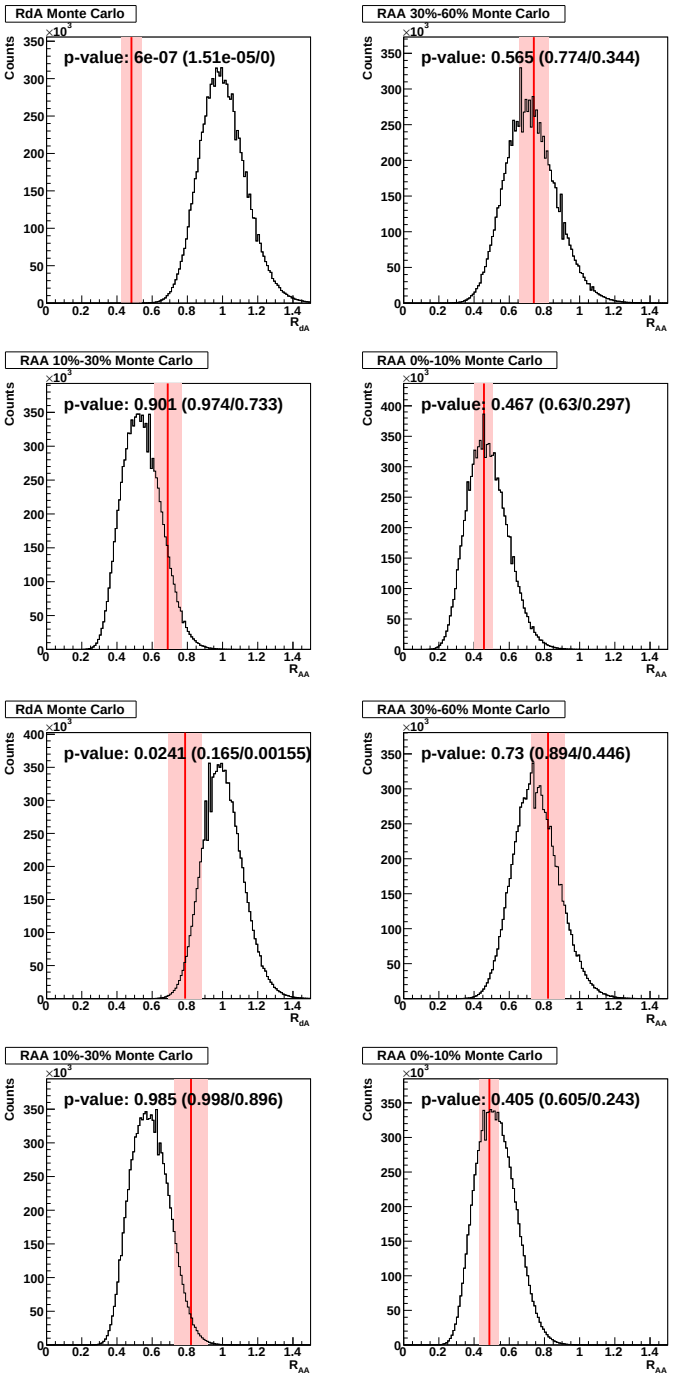

FIGURE 7.11. Summary of simulation results assuming suppression from QGP effects only (scenario 3). The upper plots show the results for $|y| < 0.5$ and the lower plots show $|y| < 1.0$. The red lines denote our results and the pinks bands show systematics uncertainties.

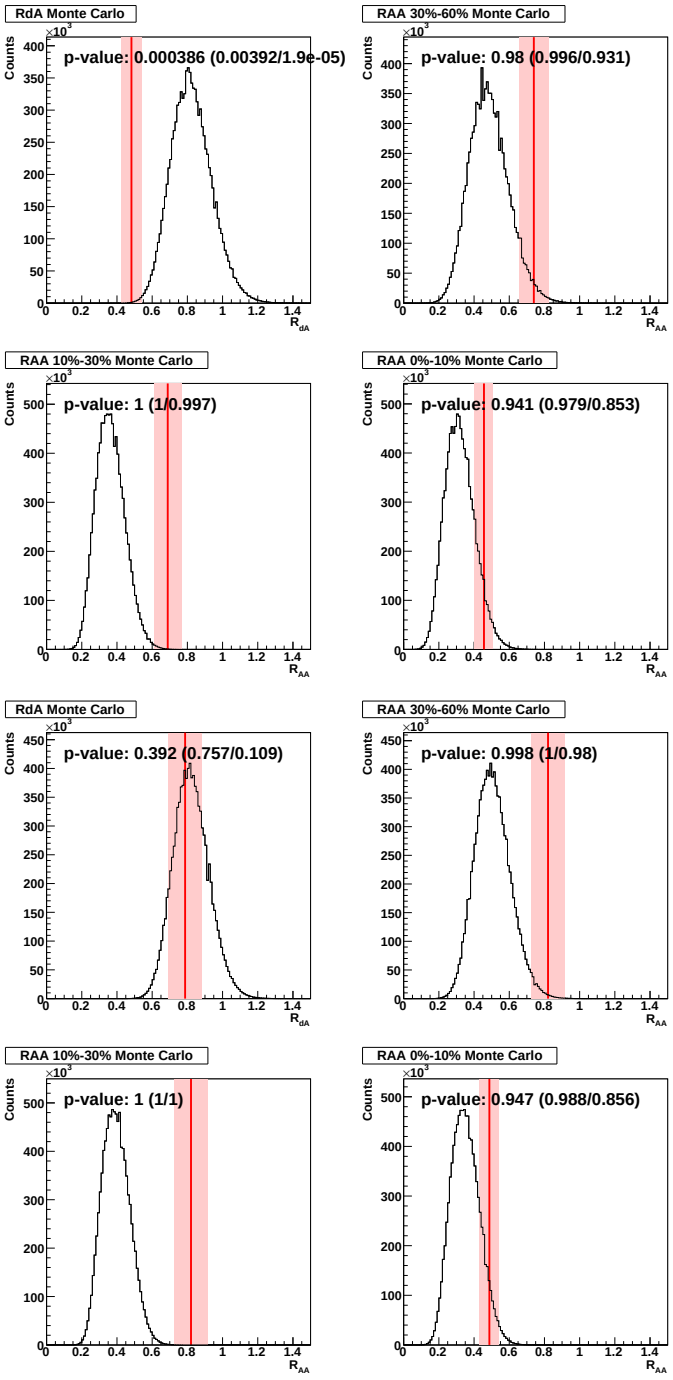

FIGURE 7.12. Summary of simulation results assuming suppression from both the QGP and CNM effects (scenario 4). The upper plots show the results for $|y| < 0.5$ and the lower plots show $|y| < 1.0$. The red lines denote our results and the pinks bands show systematics uncertainties.

However, the $|y| < 0.5$ d + Au and both central Au + Au results disfavor the 'no suppression' scenario at the 5σ level. Given these results, it is safe to say our combined results were not statistical fluctuations and there must be a source of suppression, be it hot or cold.

Next we examine the results of scenario 2, where all suppression comes from CNM effects (see Fig. 7.10). The simulations are in decent agreement with our results for most systems and centralities with a few notable exceptions. First, our central Au + Au results disfavor a scenario where all suppression comes form CNM effects at slightly above a 2σ level. While not definitive with our level of statistics, this points to additional suppression beyond what could be explained by a simple CNM suppression model. Higher statistics $p + p$ and Au + Au data is needed to increase our confidence in this result. Fortunately, we have $p + p$ data from 2012 available and the 2014 Au + Au run delivered statistics beyond expectations (around 20x the Au + Au events analysed in this thesis).

Also interesting is the result for midrapidity ($|y| < 0.5$) d + Au. This results exceeds the suppression predicted by this simple parameterization at almost 3.5σ. This level of suppression is also not seen in the Strickland-Bazow or Emerick-Zhao-Rapp models. Furthermore, results for the full rapidity range ($|y| < 1.0$) are consistent with the parameterization, which was originally calculated using results extending to slightly beyond $y = 1$. Speculating, this could be a sign that Υ created at midrapidity in d + Au collisions are given a slight kick by passing spectator nucleons, pushing them to slightly higher rapidities. Results from the recent ^{3}He + Au run might shine more light on this puzzle.

We now move on to scenario 3, where all suppression comes from the QGP (Fig. 7.11). As there is no suppression in d + Au collisions in this scenario, all of the analysis regarding d + Au results from scenario 1 still hold, greatly disfavoring this scenario from the start. However, we can still draw some conclusions by examining the Au + Au results. For all six Au + Au simulations, the results are in fairly good agreement with our measurements. This complicates our interpretation given that they were mostly in agreement with simulation in scenario 2. However, in this case even the central Au + Au simulations are in agreement with the measurements.

Finally, we examine scenario 4, combining the suppression from CNM and QGP effects (see Fig. 7.12). Again, since the model of the QGP effects used here does not modify

the $d+\mathrm{Au}$ results, the analysis of the $d+\mathrm{Au}$ results is the same as it was in scenario 2. Looking at the $\mathrm{Au}+\mathrm{Au}$ results, the simulations all show a larger suppression than the measurements. This indicates that one cannot naïvely combine suppression from the hot and cold sources modeled here. Upon reflection, this is not too surprising given that in $\mathrm{Au}+\mathrm{Au}$ collisions, any nucleon involved in the initial collision is incorporated into the bulk matter so it is not around as a spectator to kick or absorb Υ mesons.

Ultimately, our simulations show there must be suppression of Υ(1S+2S+3S) production in heavy ion collisions. The suppression seen in $d+\mathrm{Au}$ collisions shows there must be some cold-nuclear-matter effect which modifies Υ production, but whether it is from a modification of the nuclear PDF, from interactions with spectator nucleons, or some combination thereof, we cannot yet say. Suppression seen in peripheral and mid-central $\mathrm{Au}+\mathrm{Au}$ collisions are consistent with both the CNM and QGP models; the suppression seen in central events favor effects from the QGP. However, when we try to combine these two effects directly, all of the $\mathrm{Au}+\mathrm{Au}$ simulations fall out of line with the results.

CHAPTER 8

Conclusions

We successfully measured Υ(1S+2S+3S) and Υ(1S) production cross sections in $p+p$, $d+\mathrm{Au}$, and $\mathrm{Au}+\mathrm{Au}$ collisions at $\sqrt{s_{NN}} = 200$ GeV using the STAR detector at RHIC. The cross section in $p+p$ collisions for Υ(1S+2S+3S) was found to be $B_{ee} \times d\sigma/dy|_{|y|<1} = 61 \pm 8(\mathrm{stat.+fit})^{+13}_{-12}(\mathrm{syst.})$ pb. This result is consistent within errors with both NLO Color Singlet Model and NLO Color Evaporation Model calculations. The cross section in $d+\mathrm{Au}$ collisions is found to be $B_{ee} \times d\sigma/dy|_{|y|<1} = 19 \pm 3(\mathrm{stat.+fit}) \pm 3(\mathrm{syst.})$ nb. This result falls below the aforementioned NLO CEM calculations. However, if one adjusts the $d+\mathrm{Au}$ predictions based on the differences between the $p+p$ data and $p+p$ predictions, the discrepancy all but vanishes.

We measured the cold nuclear modification factor for $|y| < 1.0$ to be $R_{d\mathrm{Au}}(1S+2S+3S) = 0.79 \pm 0.22$ ($d+\mathrm{Au}$ stat.) ± 0.10 ($p+p$ stat.) ± 0.03 ($d+\mathrm{Au}$ syst.) ± 0.09 ($p+p$ syst.). Models of cold-nuclear-matter effects incorporating both initial state modifications such as shadowing and parton energy loss and final state effects such as nuclear absorption are consistent with our measured suppression. However, there is an indication of additional suppression of Υ mesons at midrapidity ($|y| < 0.5$) which is unforeseen by any calculations. It must be noted that this is only a 3σ deviation; not enough to claim proof but enough to warrant further study in future CNM runs at RHIC.

We measured Υ suppression in $\mathrm{Au}+\mathrm{Au}$ collisions in three different centrality bins. In the rapidity range $|y| < 1.0$, the centrality-integrated (0-60%) nuclear modification factor was found to be $R_{AA}(1S+2S+3S) = 0.66 \pm 0.09$ ($\mathrm{Au}+\mathrm{Au}$ stat.) ± 0.10 ($p+p$ stat.) $\pm$ 0.02 ($\mathrm{Au}+\mathrm{Au}$ syst.) ± 0.08 ($p+p$ syst.), giving a clear indication of suppression in $\mathrm{Au}+\mathrm{Au}$ collisions. Looking at the most central bin (0-10%), we find $R_{AA}(1S+2S+3S) = 0.49 \pm$ 0.13 ($\mathrm{Au}+\mathrm{Au}$ stat.) ± 0.07 ($p+p$ stat.) ± 0.02 ($\mathrm{Au}+\mathrm{Au}$ syst.) ± 0.06 ($p+p$ syst.), indicating greater suppression in central collisions than in peripheral. In the centrality-integrated

signal, we find an upper limit on the nuclear modification factor of the excited states of $R_{AA} < 0.32$. Our suppression results are consistent with calculations assuming an initial central plasma temperature in the range 428-442 MeV and others assuming 330 MeV. Hence, our results are indicative of deconfinement of the excited states and possibly of the ground state. However, given the small but noticeable discrepancy in $d + \mathrm{Au}$, more work must be done to understand and quantify cold-nuclear-matter effects before suppression in $\mathrm{Au} + \mathrm{Au}$ collisions can be fully interpreted.

Bibliography

[1] MissMJ and the Particle Data Group, "Standard model of elementary particles." https://commons.wikimedia.org/wiki/File:Standard_Model_of_Elementary_Particles.svg.

[2] Niamh O'C, "Weak decay (flipped)." https://en.wikipedia.org/wiki/File:Weak_Decay_(flipped).svg.

[3] Cjean42, "Electroweak." https://commons.wikimedia.org/wiki/File:Electroweak.svg.

[4] M. Cheng *et al.*, "The QCD equation of state with almost physical quark masses," *Phys.Rev.* **D77** (2008) 014511, arXiv:0710.0354 [hep-lat].

[5] O. Kaczmarek and F. Zantow, "Static quark-antiquark interactions in zero and finite temperature qcd: I. heavy quark free energies, running coupling, and quarkonium binding," *Phys. Rev. D* **71** (Jun, 2005) 114510. http://link.aps.org/doi/10.1103/PhysRevD.71.114510.

[6] **STAR Collaboration** Collaboration, J. Adams *et al.*, "Evidence from d+au measurements for final-state suppression of high-pt hadrons in au+au collisions at rhic," *Phys. Rev. Lett.* **91** (Aug, 2003) 072304. http://link.aps.org/doi/10.1103/PhysRevLett.91.072304.

[7] R. Snellings, "Elliptic Flow: A Brief Review," *New J.Phys.* **13** (2011) 055008, arXiv:1102.3010 [nucl-ex].

[8] **STAR Collaboration** Collaboration, B. Abelev *et al.*, "Υ cross section in $p+p$ collisions at $\sqrt(s) = 200$ GeV," *Phys.Rev.* **D82** (2010) 012004, arXiv:1001.2745 [nucl-ex].

[9] K. Eskola, H. Paukkunen, and C. Salgado, "EPS09: A New Generation of NLO and LO Nuclear Parton Distribution Functions," *JHEP* **0904** (2009) 065, arXiv:0902.4154 [hep-ph].

[10] P. Petreczky, C. Miao, and A. Mocsy, "Quarkonium spectral functions with complex potential," *Nucl.Phys.* **A855** (2011) 125–132, arXiv:1012.4433 [hep-ph].

[11] **Particle Data Group** Collaboration, J. Beringer *et al.*, "Review of Particle Physics (RPP)," *Phys.Rev.* **D86** (2012) 010001.

[12] "Apex workshop 2013." http://www.c-ad.bnl.gov/APEX/APEXWorkshop2013/.

[13] M. Harrison, S. Peggs, and T. Roser, "The rhic accelerator," *Annual Review of Nuclear and Particle Science* **52** (2002) 425–469.

[14] M. Vargyas, "Experimental and Theoretical Studies: Analysis of Low-mass Dilepton Enhancement in 200 GeV Au+Au Collisions at RHIC (thesis)," *ArXiv e-prints* (Mar., 2013) , arXiv:1303.2200 [nucl-ex].

[15] "Rhic — phobos and brahms detectors." http://www.bnl.gov/rhic/PHOBOS_BRAHMS.asp.

[16] "Phobos experiment at rhic." http://www.bnl.gov/phobos/.

[17] C. A. Whitten and T. S. Collaboration, "The beambeam counter: A local polarimeter at star," *AIP Conference Proceedings* **980** no. 1, (2008) 390–396.

[18] C. Adler *et al.*, "The rhic zero degree calorimeter," *Nucl.Instrum.Meth.A* **A470** (2001) 488–499, nucl-ex/0008005. http://arxiv.org/abs/nucl-ex/0008005.

[19] M. Anderson *et al.*, "The Star time projection chamber: A Unique tool for studying high multiplicity events at RHIC," *Nucl.Instrum.Meth.* **A499** (2003) 659–678, arXiv:nucl-ex/0301015 [nucl-ex].

[20] M. Anderson *et al.*, "A Readout system for the STAR time projection chamber," *Nucl.Instrum.Meth.* **A499** (2003) 679–691, arXiv:nucl-ex/0205014 [nucl-ex].

[21] H. Bichsel, "Comparison of bethe-bloch and bichsel functions." https://drupal.star.bnl.gov/STAR/starnotes/public/sn0439.

[22] A. Rose, "Star integrated tracker," nucl-ex/0307015. http://arxiv.org/abs/nucl-ex/0307015.

[23] **STAR Collaboration** Collaboration, M. Beddo *et al.*, "The STAR barrel electromagnetic calorimeter," *Nucl.Instrum.Meth.* **A499** (2003) 725–739.

[24] **CDF Collaboration** Collaboration, D. Acosta *et al.*, "Υ production and polarization in $p\bar{p}$ collisions at $\sqrt{s} = 1.8$-TeV," *Phys.Rev.Lett.* **88** (2002) 161802.

[25] G. Moreno *et al.*, "Dimuon production in proton - copper collisions at $\sqrt{s} = 38.8$-GeV," *Phys.Rev.* **D43** (1991) 2815–2836.

[26] J. Yoh *et al.*, "Study of Scaling in Hadronic Production of Dimuons," *Phys.Rev.Lett.* **41** (1978) 684.

[27] K. Ueno *et al.*, "Evidence for the υ'' and a search for new narrow resonances," *Phys. Rev. Lett.* **42** (Feb, 1979) 486–489. http://link.aps.org/doi/10.1103/PhysRevLett.42.486.

[28] S. Childress *et al.*, "Production dynamics of the υ in proton-nucleon interactions," *Phys. Rev. Lett.* **55** (Nov, 1985) 1962–1964. http://link.aps.org/doi/10.1103/PhysRevLett.55.1962.

[29] T. Yoshida *et al.*, "High-resolution measurement of massive-dielectron production in 800-gev proton-beryllium collisions," *Phys. Rev. D* **39** (Jun, 1989) 3516–3519. http://link.aps.org/doi/10.1103/PhysRevD.39.3516.

[30] *In the Proceedings of the 9th International Symposium on Lepton on Photon Interactions at High Energy.* Aug, 1979.

[31] C. Kourkoumelis, L. Resvanis, T. Filippas, E. Fokitis, A. Cnops, *et al.*, "Characteristics of J/psi and Upsilon production at the CERN intersecting storage rings," *Phys.Lett.* **B91** (1980) 481–486.

[32] **CERN-Columbia-Oxford-Rockefeller Collaboration, CCOR Collaboration** Collaboration, A. Angelis *et al.*, "A Measurement of the Production of Massive e^+e^- Pairs in Proton Proton Collisions at $\sqrt{s} = 62.4$-GeV," *Phys.Lett.* **B87** (1979) 398.

[33] C. Albajar *et al.*, "Beauty production at the {CERN} proton-antiproton collider," *Physics Letters B* **186** no. 2, (1987) 237 – 246. http://www.sciencedirect.com/science/article/pii/0370269387902875.

[34] **CMS Collaboration** Collaboration, V. Khachatryan *et al.*, "Upsilon production cross section in pp collisions at $\sqrt{s} = 7$ TeV," *Phys. Rev. D* **83** (Jun, 2011) 112004. http://link.aps.org/doi/10.1103/PhysRevD.83.112004.

[35] A. Frawley, T. Ullrich, and R. Vogt, "Heavy flavor in heavy-ion collisions at rhic and rhic ii," *Physics Reports* **462** no. 4–6, (2008) 125 – 175.

[36] **PHENIX Collaboration** Collaboration, A. Adare *et al.*, "$\upsilon(1S + 2S + 3S)$ production in d+Au and $p + p$ collisions at $\sqrt{s_{NN}} = 200$ GeV and cold-nuclear matter effects," *Phys.Rev.* **C87** (2013) 044909, arXiv:1211.4017 [nucl-ex].

[37] A. D. F. R. Vogt, R. E. Nelson, "Calculations for bottomium with shadowing." Private Communication, 2012.

[38] S. Brodsky and J.-P. Lansberg, "Heavy-quarkonium production in high energy proton-proton collisions at rhic," *Physical Review D* **81** no. 5, (Mar, 2010) 051502.

[39] F. Arleo and S. Peigne, "Heavy-quarkonium suppression in p-A collisions from parton energy loss in cold QCD matter," *JHEP* **1303** (2013) 122, arXiv:1212.0434 [hep-ph].

[40] D. M. Alde *et al.*, "Nuclear dependence of the production of υ resonances at 800 gev," *Phys. Rev. Lett.* **66** (May, 1991) 2285–2288. http://link.aps.org/doi/10.1103/PhysRevLett.66.2285.

[41] M. Strickland and D. Bazow 1112.2761v4. http://arxiv.org/abs/1112.2761v4.

[42] A. Emerick, X. Zhao, and R. Rapp, "Bottomonia in the quark-gluon plasma and their production at rhic and lhc," *Eur. Phys. J. A* **48** (2012) 72, 1111.6537. http://arxiv.org/abs/1111.6537.

[43] Y. Liu, B. Chen, N. Xu, and P. Zhuang *Phys. Lett. B* **697** (2011) 32. http://arxiv.org/abs/1009.2585.

[44] L. Adamczyk and T. S. Collaboration *Phys. Lett. B* **722** (2013) 55.

[45] J. J. Thompson, "Cathode rays," *The Electrician* **39** (1897) 104.

[46] A. Einstein, "Zur elektrodynamik bewegter körper," *Annalen der Physik* **322** no. 10, (1905) 891–921. http://dx.doi.org/10.1002/andp.19053221004.

[47] P. A. M. Dirac, "The quantum theory of the emission and absorption of radiation," *Proceedings of the Royal Society of London. Series A* **114** no. 767, (1927) 243–265, http://rspa.royalsocietypublishing.org/content/114/767/243.full.pdf+html. http://rspa.royalsocietypublishing.org/content/114/767/243.short.

[48] C. D. Anderson, "The positive electron," *Phys. Rev.* **43** (Mar, 1933) 491–494. http://link.aps.org/doi/10.1103/PhysRev.43.491.

[49] E. Rutherford, "The scattering of α and β particles by matter and the structure of the atom," *Philosophical Magazine* **21** (May, 1911) 669–688.

[50] J. Chadwick, "Possible Existence of a Neutron," *Nature* **129** (Feb., 1932) 312.

[51] H. Yukawa, "On the interaction of elementary particles," *Proc. Phys. Math. Soc. Japan* **17** no. 48, (1935) 139–148.

[52] J. C. Street and E. C. Stevenson, "New evidence for the existence of a particle of mass intermediate between the proton and electron," *Phys. Rev.* **52** (Nov, 1937) 1003–1004. http://link.aps.org/doi/10.1103/PhysRev.52.1003.

[53] C. M. G. Lattes, H. Muirhead, G. P. S. Occhialini, and C. F. Powell, "Processes Involving Charged Mesons," *Nature* **159** (May, 1947) 694–697.

[54] M. Riordan, *The Hunting of the Quark*. Simon & Schuster, 1987.

[55] M. Kaku, *Hyperspace: A Scientific Odyssey Through Parallel Universes, Time Warps and the Tenth Dimension*. Oxford Paperbacks, 1995.

[56] V. E. Barnes *et al.*, "Observation of a hyperon with strangeness minus three," *Phys. Rev. Lett.* **12** (Feb, 1964) 204–206. http://link.aps.org/doi/10.1103/PhysRevLett.12.204.

[57] E. D. Bloom *et al.*, "High-energy inelastic $e-p$ scattering at 6° and 10°," *Phys. Rev. Lett.* **23** (Oct, 1969) 930–934. http://link.aps.org/doi/10.1103/PhysRevLett.23.930.

[58] M. Breidenbach *et al.*, "Observed behavior of highly inelastic electron-proton scattering," *Phys. Rev. Lett.* **23** (Oct, 1969) 935–939. http://link.aps.org/doi/10.1103/PhysRevLett.23.935.

[59] H. D. Politzer, "Reliable Perturbative Results for Strong Interactions?," *Physical Review Letters* **30** (June, 1973) 1346–1349.

[60] H. David Politzer, "Asymptotic freedom: An approach to strong interactions," *Physics Reports* **14** (Nov., 1974) 129–180.

[61] D. J. Gross and F. Wilczek, "Ultraviolet behavior of non-abelian gauge theories," *Physical Review Letters* **30** no. 26, (1973) 1343–1346.

[62] J. J. Aubert, U. Becker, *et al.*, "Experimental observation of a heavy particle j," *Phys. Rev. Lett.* **33** (Dec, 1974) 1404–1406. http://link.aps.org/doi/10.1103/PhysRevLett.33.1404.

[63] J. E. Augustin *et al.*, "Discovery of a narrow resonance in e^+e^- annihilation," *Phys. Rev. Lett.* **33** (Dec, 1974) 1406–1408. http://link.aps.org/doi/10.1103/PhysRevLett.33.1406.

[64] H. Harari, "A new quark model for hadrons," *Physics Letters B* **57** no. 3, (1975) 265 – 269. http://www.sciencedirect.com/science/article/pii/0370269375900726.

[65] M. Kobayashi and T. Maskawa, "Cp-violation in the renormalizable theory of weak interaction," *Progress of Theoretical Physics* **49** no. 2, (1973) 652–657, http://ptp.oxfordjournals.org/content/49/2/652.full.pdf+html. http://ptp.oxfordjournals.org/content/49/2/652.abstract.

[66] D. C. Hom *et al.*, "Observation of high-mass dilepton pairs in hadron collisions at 400 gev," *Phys. Rev. Lett.* **36** (May, 1976) 1236–1239. http://link.aps.org/doi/10.1103/PhysRevLett.36.1236.

[67] S. W. Herb *et al.*, "Observation of a dimuon resonance at 9.5 gev in 400-gev proton-nucleus collisions," *Phys. Rev. Lett.* **39** (Aug, 1977) 252–255. http://link.aps.org/doi/10.1103/PhysRevLett.39.252.

[68] **D0 Collaboration** Collaboration, S. Abachi *et al.*, "Search for high mass top quark production in $p\overline{p}$ collisions at $\sqrt{s} =$ 1.8 tev," *Phys. Rev. Lett.* **74** (Mar, 1995) 2422–2426. http://link.aps.org/doi/10.1103/PhysRevLett.74.2422.

[69] **CDF Collaboration** Collaboration, F. Abe *et al.*, "Observation of top quark production in $\overline{p}p$ collisions with the collider detector at fermilab," *Phys. Rev. Lett.* **74** (Apr, 1995) 2626–2631. http://link.aps.org/doi/10.1103/PhysRevLett.74.2626.

[70] **UA1 Collaboration** Collaboration, G. Arnison *et al.*, "Experimental Observation of Isolated Large Transverse Energy Electrons with Associated Missing Energy at s**(1/2) = 540-GeV," *Phys.Lett.* **B122** (1983) 103–116.

[71] **UA2 Collaboration** Collaboration, M. Banner *et al.*, "Observation of Single Isolated Electrons of High Transverse Momentum in Events with Missing Transverse Energy at the CERN anti-p p Collider," *Phys.Lett.* **B122** (1983) 476–485.

[72] K. Kodama *et al.*, "Observation of tau neutrino interactions," *Physics Letters B* **504** no. 3, (2001) 218 – 224. http://www.sciencedirect.com/science/article/pii/S0370269301003070.

[73] **ATLAS Collaboration** Collaboration, G. Aad *et al.*, "Observation of a new particle in the search for the Standard Model Higgs boson with the ATLAS detector at the LHC," *Phys.Lett.* **B716** (2012) 1–29, arXiv:1207.7214 [hep-ex].

[74] **CMS Collaboration** Collaboration, S. Chatrchyan *et al.*, "Observation of a new boson at a mass of 125 GeV with the CMS experiment at the LHC," *Phys.Lett.* **B716** (2012) 30–61, arXiv:1207.7235 [hep-ex].

[75] **Super-Kamiokande Collaboration** Collaboration, Y. Fukuda *et al.*, "Evidence for oscillation of atmospheric neutrinos," *Phys.Rev.Lett.* **81** (1998) 1562–1567, arXiv:hep-ex/9807003 [hep-ex].

[76] **SNO Collaboration** Collaboration, Q. Ahmad *et al.*, "Measurement of the rate of $\nu_e + d \to p + p + e^-$ interactions produced by ^8B solar neutrinos at the Sudbury Neutrino Observatory," *Phys.Rev.Lett.* **87** (2001) 071301, arXiv:nucl-ex/0106015 [nucl-ex].

[77] Z. Fodor and S. Katz, "The Phase diagram of quantum chromodynamics," arXiv:0908.3341 [hep-ph].

[78] C. Berger *et al.*, "Topology of the -decay," *Zeitschrift für Physik C Particles and Fields* **8** no. 2, (1981) 101–114. http://dx.doi.org/10.1007/BF01547873.

[79] C. Berger *et al.*, "Jet analysis of the (9.46) decay into charged hadrons," *Physics Letters B* **82** no. 3–4, (1979) 449 – 455. http://www.sciencedirect.com/science/article/pii/037026937990265X.

[80] B. R. Stella and H.-J. Meyer, "Y(9.46 GeV) and the gluon discovery (a critical recollection of PLUTO results)," *Eur.Phys.J.* **H36** (2011) 203–243, arXiv:1008.1869 [hep-ex].

[81] R. Brandelik *et al.*, "Evidence for planar events in e+e annihilation at high energies," *Physics Letters B* **86** no. 2, (1979) 243 – 249. http://www.sciencedirect.com/science/article/pii/037026937990830X.

[82] D. P. Barber *et al.*, "Discovery of three-jet events and a test of quantum chromodynamics at petra," *Phys. Rev. Lett.* **43** (Sep, 1979) 830–833. http://link.aps.org/doi/10.1103/PhysRevLett.43.830.

[83] C. Berger *et al.*, "Evidence for gluon bremsstrahlung in e+e annihilations at high energies," *Physics Letters B* **86** no. 3–4, (1979) 418 – 425. http://www.sciencedirect.com/science/article/pii/0370269379908694.

[84] W. Bartel *et al.*, "Observation of planar three-jet events in e $^{+}$e $^{-}$ annihilation and evidence for gluon bremsstrahlung," *Physics Letters B* **91** (Mar., 1980) 142–147.

[85] **STAR Collaboration** Collaboration, K. Ackermann *et al.*, "Elliptic flow in Au + Au collisions at (S(NN))**(1/2) = 130 GeV," *Phys.Rev.Lett.* **86** (2001) 402–407, arXiv:nucl-ex/0009011 [nucl-ex].

[86] **STAR Collaboration** Collaboration, J. Adams *et al.*, "Azimuthal anisotropy at RHIC: The First and fourth harmonics," *Phys.Rev.Lett.* **92** (2004) 062301, arXiv:nucl-ex/0310029 [nucl-ex].

[87] **STAR Collaboration** Collaboration, J. Adams *et al.*, "Multi-strange baryon elliptic flow in Au + Au collisions at s(NN)**(1/2) = 200-GeV," *Phys.Rev.Lett.* **95** (2005) 122301, arXiv:nucl-ex/0504022 [nucl-ex].

[88] **STAR Collaboration** Collaboration, B. Abelev *et al.*, "Mass, quark-number, and $\sqrt{s_{NN}}$ dependence of the second and fourth flow harmonics in ultra-relativistic nucleus-nucleus collisions," *Phys.Rev.* **C75** (2007) 054906, arXiv:nucl-ex/0701010 [nucl-ex].

[89] **STAR Collaboration** Collaboration, B. Abelev *et al.*, "Identified particle production, azimuthal anisotropy, and interferometry measurements in Au+Au collisions at s(NN)**(1/2) = 9.2- GeV," *Phys.Rev.* **C81** (2010) 024911, arXiv:0909.4131 [nucl-ex].

[90] **STAR Collaboration** Collaboration, B. Abelev *et al.*, "Charged and strange hadron elliptic flow in Cu+Cu collisions at $\sqrt{s_{NN}}$ = 62.4 and 200 GeV," *Phys.Rev.* **C81** (2010) 044902, arXiv:1001.5052 [nucl-ex].

[91] **STAR Collaboration** Collaboration, L. Adamczyk *et al.*, "Measurement of J/ψ Azimuthal Anisotropy in Au+Au Collisions at $\sqrt{s_{NN}}$ = 200 GeV," *Phys.Rev.Lett.* **111** no. 5, (2013) 052301, arXiv:1212.3304 [nucl-ex].

[92] **STAR Collaboration** Collaboration, L. Adamczyk *et al.*, "Elliptic flow of identified hadrons in Au+Au collisions at $\sqrt{s_{NN}}$ = 7.7-62.4 GeV," *Phys.Rev.* **C88** (2013) 014902, arXiv:1301.2348 [Unknown].

[93] **STAR Collaboration** Collaboration, L. Adamczyk *et al.*, "Beam-Energy Dependence of Directed Flow of Protons, Antiprotons and Pions in Au+Au Collisions," *Phys.Rev.Lett.* **112** (2014) 162301, arXiv:1401.3043 [nucl-ex].

[94] **STAR Collaboration** Collaboration, L. Adamczyk *et al.*, "Third Harmonic Flow of Charged Particles in Au+Au Collisions at sqrtsNN = 200 GeV," *Phys.Rev.* **C88** no. 1, (2013) 014904, arXiv:1301.2187 [nucl-ex].

[95] T. Matsui and H. Satz, "J/ψ suppression by quark-gluon plasma formation," *Physics Letters B* **178** no. 4, (1986) 416 – 422.

[96] N. Brambilla, "NRQCD and Quarkonia," *eConf* **C0610161** (2006) 004, arXiv:hep-ph/0702105 [hep-ph].

[97] S. Gavin, M. Gyulassy, and A. Jackson, "Hadronic j/ψ suppression in ultrarelativistic nuclear collisions," *Physics Letters B* **207** no. 3, (1988) 257 – 262. http://www.sciencedirect.com/science/article/pii/0370269388905710.

[98] C. Gerschel and J. Hufner, "Charmonium suppression in heavy ion collisions," *Ann.Rev.Nucl.Part.Sci.* **49** (1999) 255–301, arXiv:hep-ph/9802245 [hep-ph].

[99] Z.-w. Lin and C. Ko, "Upsilon absorption in hadronic matter," *Phys.Lett.* **B503** (2001) 104–112, arXiv:nucl-th/0007027 [nucl-th].

[100] F. Karsch and E. Laermann, "Thermodynamics and in medium hadron properties from lattice QCD," arXiv:hep-lat/0305025 [hep-lat].

[101] M. Cheng *et al.*, "Equation of State for physical quark masses," *Phys.Rev.* **D81** (2010) 054504, arXiv:0911.2215 [hep-lat].

[102] **Wuppertal-Budapest Collaboration** Collaboration, S. Borsanyi *et al.*, "Is there still any T_c mystery in lattice QCD? Results with physical masses in the continuum limit III," *JHEP* **1009** (2010) 073, arXiv:1005.3508 [hep-lat].

[103] S. Digal, P. Petreczky, and H. Satz, "Quarkonium feed down and sequential suppression," *Phys.Rev.* **D64** (2001) 094015, arXiv:hep-ph/0106017 [hep-ph].

[104] **STAR Collaboration** Collaboration, H. Agakishiev *et al.*, "High p_T non-photonic electron production in $p+p$ collisions at $\sqrt{s}$ = 200 GeV," *Phys.Rev.* **D83** (2011) 052006, arXiv:1102.2611 [nucl-ex].

[105] **STAR Collaboration** Collaboration, J. Adams *et al.*, "Open charm yields in d + Au collisions at s(NN)**(1/2) = 200-GeV," *Phys.Rev.Lett.* **94** (2005) 062301, arXiv:nucl-ex/0407006 [nucl-ex].

[106] **PHENIX Collaboration** Collaboration, A. Adare *et al.*, "Heavy Quark Production in $p+p$ and Energy Loss and Flow of Heavy Quarks in Au+Au Collisions at $\sqrt{s_N N} = 200$ GeV," *Phys.Rev.* **C84** (2011) 044905, arXiv:1005.1627 [nucl-ex].

[107] G. Danby *et al.*, "Observation of High-Energy Neutrino Reactions and the Existence of Two Kinds of Neutrinos," *Phys.Rev.Lett.* **9** (1962) 36–44.

[108] M. Banner, J. W. Cronin, J. K. Liu, and J. E. Pilcher, "Measurement of the branching ratio $k_l \to \gamma\gamma$ $k_l \to 3\pi^0$," tech. rep., Palmer Physical Laboratory, Princeton University, United States Department of Energy, 1968.

[109] M. Banner, J. W. Cronin, J. K. Liu, and J. E. Pilcher, "Measurement of the branching ratio $k_l \to 2\pi^0$ $k_l \to 3\pi^0$," tech. rep., Palmer Physical Laboratory, Princeton University, United States Department of Energy, 1968.

[110] J. Benjamin *et al.*, "Injecting RHIC from the Brookhaven tandem Van de Graaff,".

[111] L. Ahrens *et al.*, "Status and Recent Performance of the Accelerators that Serve as Gold Injector for RHIC," *Conf.Proc.* **C0106181** (2001) 3326–3328.

[112] J. Alessi *et al.*, "Construction of the bnl ebis preinjector," *Proceedings of the 2009 PAC Conference, Vancouver, BC, Canada* **MO6RFP025** (2009) .

[113] 2014. http://www.bnl.gov/rhic/linac.asp.

[114] A. Drees *et al.*, "Abort gap studies and cleaning during rhic heavy ion operation," in *Particle Accelerator Conference, 2003. PAC 2003. Proceedings of the*, vol. 3, pp. 1685–1687 vol.3. May, 2003.

[115] **STAR Collaboration** Collaboration, K. Ackermann *et al.*, "STAR detector overview," *Nucl.Instrum.Meth.* **A499** (2003) 624–632.

[116] J. Kiryluk and S. Collaboration, "Local polarimetry for proton beams with the star beam beam counters," *Proceedings of the 16th International Spin Physics Symposium* (October, 2004) , hep-ex/0501072. http://arxiv.org/abs/hep-ex/0501072.

[117] J. Kiryluk and S. Collaboration, "Relative luminosity measurement in star and implications for spin asymmetry determinations," *AIP Conference Proceedings* **675** no. 1, (September, 2003) 424–428.

[118] **STAR Collaboration** Collaboration, J. Adams *et al.*, "Transverse-momentum and collision-energy dependence of high-pt hadron suppression in au+au collisions at ultrarelativistic energies," *Phys. Rev. Lett.* **91** (Oct, 2003) 172302. http://link.aps.org/doi/10.1103/PhysRevLett.91.172302.

[119] W. J. Llope, "The star time-of-flight system," *Proceedings of the 24th Winder Workshop on Nuclear Dynamics* (2008) .

[120] R. Reed *et al.*, "Vertex finding in pile-up rich events for p+p and d+au collisions at star,".

[121] J. Dunlop, "2008 d+au and p+p run (run 8) trigger faq," February, 2009. http://www.star.bnl.gov/protected/common/common2008/trigger2008/triggers2008.html.

[122] J. Dunlop, "p+p run 9 trigger faq," August, 2009. http://www.star.bnl.gov/protected/common/common2009/trigger2009/triggers2009.html.

[123] J. Dunlop, "2010 trigger page," 2010. http://www.star.bnl.gov/protected/common/common2010/trigger2010/triggers2010.html.inprogress.

[124] **GEANT4** Collaboration, S. Agostinelli *et al.*, "GEANT4: A Simulation toolkit," *Nucl.Instrum.Meth.* **A506** (2003) 250–303.

[125] http://online.star.bnl.gov/L2Quarkonia2007/.

[126] C. Yang *et al.*, "Calibration and performance of the STAR Muon Telescope Detector using cosmic rays," arXiv:1402.1078 [physics.ins-det].

[127] J. E. Gaiser, *Charmonium Spectroscopy from Radiative Decays of the J/ψ and ψ'*. PhD thesis, Stanford University, August, 1982.

[128] W. Verkerke and D. Kirkby, "The RooFit toolkit for data modeling," *ArXiv Physics e-prints* (June, 2003) , physics/0306116.

[129] G. Moreno *et al.*, "Dimuon production in proton-copper collisions at 38.8 gev," *Phys. Rev. D* **43** (May, 1991) 2815–2835. http://link.aps.org/doi/10.1103/PhysRevD.43.2815.

[130] "Centrality and glauber mc simulation in run10 au + au collisions," May, 2012. http://www.star.bnl.gov/protected/common/common2010/centrality/.

[131] W. A. Rolke, A. M. López, and J. Conrad *Nucl.Instrum.Meth.A* **551** (2005) 493.

[132] J. Dunlop, "Normalization of $p + p$ data." http://www.star.bnl.gov/protected/highpt/dunlop/pp/normalization/.

[133] **STAR Collaboration** Collaboration, B. I. Abelev *et al.*, "Longitudinal double-spin asymmetry and cross section for inclusive jet production in polarized proton collisions at s=200 gev," *Phys. Rev. Lett.* **97** (Dec, 2006) 252001. http://link.aps.org/doi/10.1103/PhysRevLett.97.252001.

[134] **STAR Collaboration** Collaboration, B. I. Abelev *et al.*, "Longitudinal double-spin asymmetry and cross section for inclusive neutral pion production at midrapidity in polarized proton collisions at s=200 gev," *Phys. Rev. D* **80** (Dec, 2009) 111108. http://link.aps.org/doi/10.1103/PhysRevD.80.111108.

[135] J. Balweski, "Vertex efficiency study for 2006." http://www.star.bnl.gov/protected/spin/balewski/2006-PPV-eval/effiReal2006/.

[136] T. Ullrich, "Study on upsilon polarization," September, 2009. http://www.star.bnl.gov/protected/heavy/ullrich/ups-pol.pdf.

[137] E. Ferreiro, F. Fleuret, J. Lansberg, N. Matagne, and A. Rakotozafindrabe, "Υ production in p(d)A collisions at RHIC and the LHC," *Eur.Phys.J.* **C73** (2011) 2427, arXiv:1110.5047 [hep-ph].

[138] R. Vertesi, "U+u upsilon raa results." Jun, 2014.

[139] **(CDF Collaboration)** Collaboration, T. Affolder *et al.*, "Production of $\upsilon(1s)$ mesons from χ_b decays in $p\bar{p}$ collisions at s=1.8 tev," *Phys. Rev. Lett.* **84** no. 10, (Mar, 2000) 2094–2099.

[140] **LHCb Collaboration** Collaboration, R. Aaij *et al.*, "Measurement of the fraction of $\Upsilon(1S)$ originating from $\chi_b(1P)$ decays in pp collisions at $\sqrt{s} = 7$ TeV," *JHEP* **1211** (2012) 031, `arXiv:1209.0282 [hep-ex]`.